

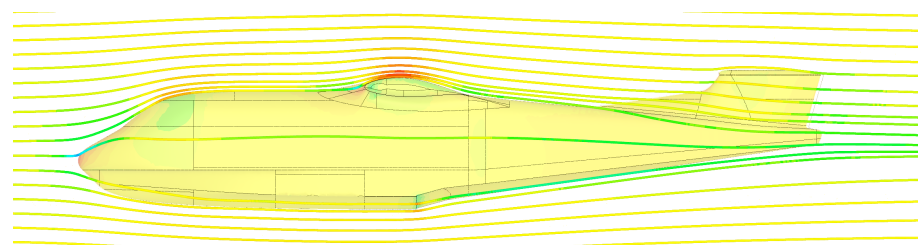
Joakim Saugen

Aerodynamic Optimization of a Flying Boat Hull

Bachelor's thesis in Mechanical Engineering

Supervisor: Anna Olsen

December 2024



Norwegian University of
Science and Technology

Joakim Saugen

Aerodynamic Optimization of a Flying Boat Hull

Bachelor's thesis in Mechanical Engineering
Supervisor: Anna Olsen
December 2024

Norwegian University of Science and Technology
Faculty of Engineering
Department of Mechanical and Industrial Engineering



Norwegian University of
Science and Technology

MAST2900 - BACHELOR THESIS MECHANICAL ENGINEERING

Aerodynamic Optimization of a Flying Boat Hull

Joakim Saugen

Mechanical Engineering

Autumn 2024



Norges teknisk-naturvitenskapelige universitet
Institutt for maskinteknikk og produksjon

Preface

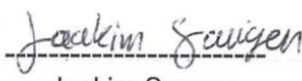
This thesis investigates the aerodynamic drag of a flying boat hull, and methods to reduce this drag. This work is the final thesis of a bachelors degree in mechanical engineering.

The work in this thesis is part of the ongoing development of a clean sheet, electric flying boat. Most of the research done on the subject of flying boat hulls was done over 60 years ago. With the increased importance of optimizing aerodynamic drag due to the range challenges of electric flight, as well as new possibilities brought on by the design freedom of composites and new development methods like CFD, this thesis aims to aid in the development of new means of transportation, electric flight.

I would like to thank my supervisor, Anna Olsen, for all her help and a lot of good guidance and support. I would also like to thank the team at the NTNU wind tunnel and, in particular, Srikar Yadala V, for allowing me to use their facility for this thesis and for all the help prior to, during, and after the testing.

I also wish to thank the team at Elfly for the support during the work on this thesis. I especially want to thank Kenzo Sasaki for his guidance.

Torp, 20.12.2024



Joakim Saugen

Abstract

With global warming becoming an increasingly critical challenge, the development of sustainable aviation technologies is essential. This thesis investigates methods to reduce the aerodynamic drag of a nine-passenger, electric flying boat hull to improve its efficiency and viability for zero-emission transport.

Using a combination of literature review, wind tunnel testing, and computational fluid dynamics (CFD) analysis, this study examines the aerodynamic effects of design features such as step geometry and fairings, afterbody angle, and overall hull dimensions. The thesis also briefly considers how changes to these features might impact hydrodynamic performance, ensuring a balanced design approach.

Due to challenges with the accuracy of the wind tunnel testing, the results from this part of the thesis were not directly transferable, but the results were used in order to calibrate the CFD results.

Results demonstrate that aerodynamic drag can be reduced significantly, potentially by 15% to 20%, with the most substantial improvements achieved through step fairings and optimizing the hull's angle of incidence. Fairing the step alone offers a reduction of up to 15%, with drag reductions showing a non-linear relationship to the extent of fairing applied. These findings highlight key opportunities for advancing the design of electric flying boats.

Sammendrag

Global oppvarming utgjør en stadig mer kritisk utfordring. Det er derfor essensielt å utvikle mer bærekraftige løsninger innen alle områder, inkludert luftfart. Denne oppgaven undersøker metoder for å redusere den aerodynamiske motstanden til skroget på en elektrisk flybåt med plass til ni passasjerer, for å forbedre effektiviteten og akselerere overgangen til nullutslipps luftfart.

Gjennom en kombinasjon av litteraturstudier, vindtunneltesting og CFD-analyse undersøker studien geometriske endringer for å bedre aerodynamikken, spesielt rundt "step" regionen og vinkelen på bakre del av skroget. Oppgaven vurderer også kort hvordan disse endringene vil påvirke de hydrodynamiske egenskapene til flyet.

Grunnet utfordringer med nøyaktigheten på vindtunnel testingen var ikke resultatene fra denne delen av studien direkte overførbar, men kunne isteden brukes for å validere CFD modellen.

Resultatene viser at den aerodynamiske motstanden kan reduseres betydelig, potensielt med 15% til 20%, der de største forbedringene oppnås gjennom å delvis rette ut "steppet" og endre vinkelen på skroget i forhold til luftstrømmen. Ved å delvis dekke til "steppet" kunne den aerodynamiske motstanden reduseres med opptil 15%.

Contents

1	Introduction	1
1.1	Background	1
1.2	Thesis Objective	1
1.3	Scope	1
1.4	Requirements and Standards	2
1.5	Seaplanes	2
2	Hydrodynamics of Flying Boat Hulls	3
2.1	Hydrodynamic Performance	3
2.2	Basic Seaplane Hull	4
2.3	Take-off Performance	5
2.4	Hydrodynamic Resistance	6
2.5	Dynamic Stability	8
2.6	Hydrodynamic Loads	10
3	Aerodynamic Theory	12
3.1	Fundamentals of Fluid Dynamics	12
3.2	Fundamentals of Aerodynamics and Flight Physics	13
4	Literature study: Aerodynamic optimization	17
4.1	Method	17
4.2	Aerodynamic Impact of the Step	18
4.3	Sternpost Angle	26
4.4	Conventional VS. Planning Tail Hulls	28
4.5	Length/Width Ratio	29
4.6	Height/Width Ratio	30
4.7	Chines Radius and Flare	30
4.8	Impact of Deadrise Angle	31
4.9	Results Literature Study	32
5	Wind Tunnel	34
5.1	Test Objective	34
5.2	Test Facility	35
5.3	Model Design	37
5.4	Experimental Aerodynamics	41
5.5	Other Aerodynamic Dissimilarities	43
5.6	Integration Into Wind Tunnel	46
5.7	Missing Data Points	46
5.8	Results	47
5.9	Post Test Error Analysis	47
6	CFD Study of Step Geometry	52
6.1	Choice of CFD Model	52
6.2	CAD Model Preparation and Import	54
6.3	Meshing	54
6.4	Runs	58
6.5	Results	59
6.6	Discussion on the Accuracy and Confidence in the Results	59
7	Conclusion	63

8 Future Work	64
A Step Geometries for Wind Tunnel Testing	II
B Deceleration of AI aids and tools	VII
C CFD Appendix	VIII

List of Figures

2.1	Side-view of an example flying boat. Figure borrowed from Thurston (1978)	3
2.2	Gradual change from streamlined shape to a flying boat hull. The numbers to the right are the relative drag as a percentage of the full flying boat hull. Figure borrowed from (Coombes and Clark 1937)	4
2.3	Illustration of deadrise angle, with and without flare. Image edited based on two original images from (Thurston 1978)	5
2.4	Phases during takeoff. Source of figure: Recolored by prof. E. Wilczek, based on data from Sottorf (1937)	6
2.5	Hydrodynamic forces during displacement phase. Figure borrowed from Sottorf (1937)	7
2.6	Spray aft of the step, onto the after body. Source of figure: Recolored by prof. E. Wilczek, based on drawing by (Sottorf 1937)	7
2.7	Illustration of severe porpoising leading to takeoff at too low speed, and subsequent stall and crash. Figure borrowed from FFA (2014)	8
2.8	Example of plot of upper and lower trim limits along the takeoff profile for a seaplane. Figure borrowed from lecture held by prof. E. Wilczek (Wilczek 2021) .	10
2.9	Distribution of afterbody pressure, as a function of sternpost angle. The left image shows the view of the frontal section. The right image shows a side view from the step extending rearwards. Figure borrowed from Tomaszewski, Smith and Chalmers (1946)	10
3.1	Development of turbulent flow over a flat plate. Image edited based on an original image by Leishman (2024c)	12
3.2	Flow around a smooth ball vs golf ball, illustrating the delaying effect of flow separation caused by turbulence. Figure borrowed from Leishman (2024c)	13
3.3	Coordinate and rotation axis for an aircraft	14
3.4	Aerodynamic forces acting on an airfoil. Image borrowed from: Leishman (2024a)	14
3.5	Drag of different shapes, broken down into pressure and friction drag. Different shapes can be seen to have very large variations in drag. Image has been edited based on two original images from (Talay 1975)	16

4.1	Collection of 4 different flying boat hulls, with wind tunnel test data investigating the drag related to the depth of the step	19
4.2	Trim limit as a function of step height and speed. Figure borrowed from Olson and Land (1942)	19
4.3	Hydrodynamic drag during takeoff run, as a function of step height. Source: Recolored in an unpublished report by Prof E. Wilczek, based on original data from Sottorf (1937)	20
4.4	Illustration of Step Geometry. Top Left: V-shaped step from side view. Bottom Left: a straight step in side view. Right Figure, V-shaped step from bottom view. A straight step would go where the dashed line is located. Figure borrowed from Parkinson and Land (1944)	21
4.5	Air drag as a function of step shape and angle of attack. Figure borrowed from Coombes and Clark (1937)	21
4.6	Drag as a percentage of drag without step fairing over a range of fairing lengths. Figure borrowed from Coombes and Clark (1937)	22
4.7	Drag coefficient of a flying boat hull with different step fairings, as a function of Reynolds number (10^6). Figure borrowed from Hamilton (1956)	23
4.8	Hulls tested by Riebe and Yates (1947)	24
4.9	Design assurance levels in aerospace, according to the DO-254 standard, with targeted system failure rates. (Mistral 2024)	25
4.10	Landing deceleration and resistance plots, when landing with and without step. Figures borrowed from Benson and Freihofner (1944)	26
4.11	Ar drag vs angle of incidence	27
4.12	Effect of tail afterbody upsweep on land planes. Figure borrowed from Torenbeek (1982).	27
4.13	Stability against skipping, as a factor of beam loading, sternpost angle and step height. Figure borrowed from Locke (1946)	28
4.14	The difference between two step VS. one step flying boat hull. Figure is of Model 203 from the Langley tank facility. Figure borrowed from Riebe and Naeseth (1947a)	29
4.15	Comparison of hydrodynamic resistance for a two-step (labeled conventional hull) and the one-step hull (labeled Planning tail). Source: Recolored by Prof. E. Wilczek, based on original figure from Dawson, Walter and Hay (1946)	29

4.16 Effect of flare on air drag, as a function of angle of incidence. Figure edited based on two figures from Coombes and Clark (1937)	30
4.17 Hydrodynamic resistance and landing loads as a function of deadrise angle. The graph is given in deadrise dihedral angle α , not the typical definition of deadrise angle as described in Figure 2.3. Figure borrowed from Sottorf (1937).	31
4.18 Increase of stability limit due to addition of smaller steps behind the rear step. Figure edited based on original from Sottorf (1942)	32
4.19 Afterbody step on Beriev A-40. Source:Wilczek (2021), unknown original source .	33
5.1 Overview picture of a closed loop wind tunnel, image from www.onera.fr	35
5.2 Setup for mounting the model to the measuring equipment	36
5.3 Scale Comparison between 9% model and full scale aircraft	38
5.4 CAD Render of the model used in wind tunnel testing. The figure shows the sections the model was printed in, the interchangeable parts of the model, and the stiffing aluminum beams running the length of the model	40
5.5 Model in the process of being assembled. The rear section assembled, while the front sections are in the background	40
5.6 Flow over a body in external and internal flow. Figure Borrowed from: Katz (1995)	42
5.7 Flow through a wind tunnel, wind development of boundary layer, and pressure gradient along the length of the test section. Figure borrowed from Leishman (2024c)	43
5.8 Compressibility ratio VS. Mach number. Figure borrowed from Leishman (2024c)	44
5.9 Scale model in the wind tunnel	46
5.11 Smoke visualization of flow separation. Wind speed: 5m/s	49
5.12 Measurement made in the wind tunnel showing the size of fluctuations over a 30-second period.	50
5.13 Vortex shedding of a cube. Image borrowed from: Stern and yang (2012)	50
6.1 Difference between solvers methods. Image Borrowed from: LEAP (2018)	53
6.2 Flow volume set up as a function of the model size	54
6.3 Example of buildup of a turbulent boundary layer, and linear interpolation error. Image edited based on original images from Ansys (2020b) and Wimshurst (2022)	55

6.4	Inflation layers should be contained within the inflation layers, as seen in the right image, in order to resolve the boundary layer properly. Image borrowed from Wimshurst (2021a)	55
6.5	Example image of good and poor volume transition between inflation layer. Image borrowed from Wimshurst (2021a)	56
6.6	Input and output values used for determining the inflation layer in the mesh	56
6.7	Mesh independence study performed on the TAC1 hull	57
6.8	Refinement regions used for this CFD study. A third volume was used around the step region but is not that visible in the image.	58
6.9	Mesh used in the CFD study comparing steps	58
6.10	Results from CFD step study. The drag of the fairings is given as a percentage decrease compared to the non-faired step with a depth of 5.8%. The x-axis is the length of the fairing for that run	59
6.11	Flow field around aircraft showing flow separation behind the step without fairing	60
6.12	Convergence of a CFD run, over 3000 iterations	61
6.13	Flow field of flow in the wind tunnel, simulated by CFD. The interference from the mounting strut can be clearly seen. The surface of the model is plotted with a pressure field in [Pa], while the surrounding field is plotted with velocity [m/S]. Model seen from top view	62
A.1	Frontal and side view of model used in the wind tunnel testing, including wing and tail fairings, and tail attachment to change afterbody angle	II
C.1	Zoomed in of mesh used in the CFD study comparing steps	VIII
C.3	Y^+ plotted on the surface of the model, in the range of 0 to 2	VIII
C.5	Residuals plotted for the run with no fairings	IX

Terminology

Afterbody	Part of aircraft body aft of the step
Angle of Incidence	Angle between fuselage and wing cord
Beam	Width of the hull
CFD	Computational Fluid Dynamics
Chines	Sharp break between hull and fuselage
CS23	EASA regulations covering small aircraft
Deadrise	Angle from keel to chines
Drag Coefficient (Cd)	Dimensionless number for drag
EASA	European Union Aviation Safety Agency
Fairing	Structure added for aerodynamic (streamlining drag reduction)
Flare	Gradually changing of the deadrise angle
Forebody	Part of aircraft body in front of the step
Hull	Part of a flying boat body that is submerged during water operations
Hump	Period of highest hydrodynamical resistance prior to planning
Keel	Bottom edge of the hull, running the length of the body
Parasitic Drag	Drag not related to lift
Porpoising	Instability in planning, causing oscillating trim
Skipping	Type of porpoising involving heave
Step	Sharp break in the continuity of the hull
TAC1	Test Aircraft 1
Trim	Angle of the body relative to the horizontal axis (aka. pitch)

1 Introduction

1.1 Background

Globally, aviation accounts for about 4% of the total global greenhouse emissions to date. With passenger numbers rising by 3% yearly, this share in total emissions is predicted to double by 2050. (Klöwer 2021) With global warming set to exceed the 2015 Paris 1.5 degree goal in 2024, reducing all sources of greenhouse gasses is more crucial than ever. (C3S 2024) The TAC1 program aims to accelerate this transition by electrifying seaplanes, one of the available market segments with the shortest range requirements. The TAC1 program aims to develop a clean-sheet, nine-passenger electric flying boat certified under EASA CS23 regulations.

1.2 Thesis Objective

Due to batteries' relatively poor energy density (1.4 MJ/kg) compared to jet fuel (42 MJ/kg), reducing the required energy for flight is an important step toward the viability of electric flight.

The objective of this thesis is therefore:

Investigate potentials for reducing the aerodynamic drag of the TAC1 flying boat hull.

Reducing the aerodynamic will also decrease operating cost for an electric aircraft. Although electricity is relatively cheap, compared to jet fuel, high performance batteries do not last that long, and will have to be replaced at a regular basis. This makes battery cost a variable cost, in the same way as fuel, and will be a major driving cost of operations. By reducing the energy consumption, the battery wear, and thereby, cost, will be reduced.

1.3 Scope

The thesis will focus on the aerodynamic drag of the fuselage and hull of the aircraft. The wings, tail section, and external equipment are considered outside the scope of this thesis.

The thesis consists of the following sections:

- An introduction to the hydrodynamics of flying boat
- A literature study on aerodynamic refinements of flying boats
- An experiment section in the large wind tunnel at NTNU

- A CFD study investigating the step drag

The initial literature study focused broadly on the fuselage. At the same time, for the experiment section, it was decided to reduce the scope further only to consider the step section and afterbody angle. These features were chosen due to their relatively large contribution to aerodynamic drag.

This thesis is only one part of the development of the TAC1 hull. The work on aerodynamics in this thesis will be combined with hydrodynamic research and tests from other work, as well as commercial and operational limitations to derive the final shape.

1.4 Requirements and Standards

As the TAC1 program aims to certify the aircraft for commercial operations under CS23 Level 3, applicable standards and requirements must be met. Many aircraft performance requirements are affected by aircraft drag, but the most critical requirements regarding the fuselage and hull are those concerning safety during water operation.

From CS23 Amendment 4: (EASA 2015)

- Section 75c: "The landing must be made without excessive vertical acceleration or tendency to bounce, nose-over, ground loop, porpoise or water loop."
- Section 231a: "A seaplane or amphibian may not have dangerous or uncontrollable porpoising characteristics at any normal operating speed on the water."
- Section 233d: "Seaplanes must demonstrate satisfactory directional stability and control for water operations up to the maximum wind velocity specified in subparagraph (a)."

1.5 Seaplanes

Seaplanes are currently being operated by about 40 commercial operators in many regions around the world, for both short-haul costal transport and sightseeing missions, most notably the Maldives and the Vancouver area. These missions are typically very short, with an average range of 75 km, making them well-suited for electric aviation.

Seaplanes can in general be split in two classes: Float planes which utilize external floats below the fuselage to provide buoyancy, and flying boats which utilize the fuselage as the body of contact with the water. The TAC1 aircraft is a flying boat.

2 Hydrodynamics of Flying Boat Hulls

In addition to functioning as aircraft, seaplanes must function as boats. In order to achieve sufficient handling on water during taxiing, takeoff and landing, their shape must deviate from that of a relatively streamlined land plane. If one tries to optimize the aerodynamics of a seaplane without understanding the hydrodynamics, the design would easily trend towards that of a circular fuselage land plane shape, resulting in poor water characteristics. In order to optimize the aerodynamics, it is therefore important to understand what features are added to a seaplane hull and how they affect the hydrodynamic performance. This section aims to outline the basics of flying boat hydrodynamical design. (deCallies 1967).

A typical flying boat hull can be seen in Figure 2.1. A design goal can then be set for a specific hydrodynamic performance, and different characteristics can be tweaked in order to achieve that performance at the least aerodynamic penalty possible.

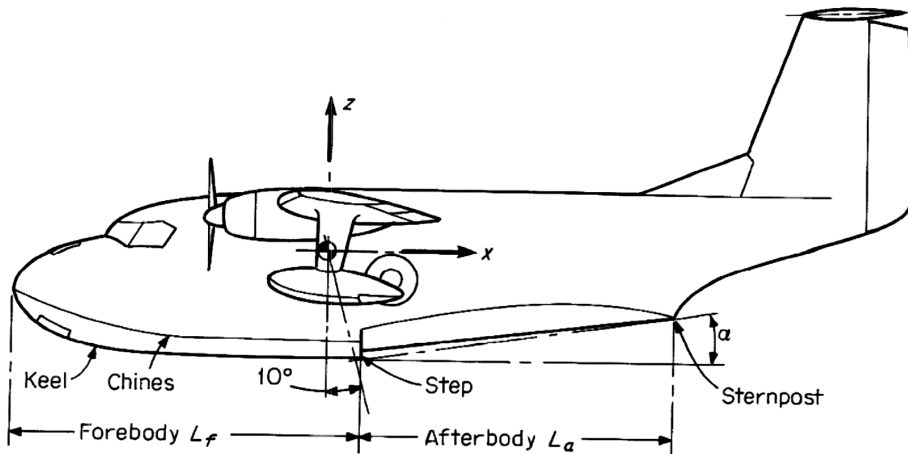


Figure 2.1: Side-view of an example flying boat. Figure borrowed from Thurston (1978)

2.1 Hydrodynamic Performance

There are four primary factors that can be considered as hydrodynamic performance.

Hydrodynamic resistance is the water drag that acts on the hull when it moves through the water. Generally, we want to reduce this in order to decrease the takeoff distance and power requirement of the motor. Shorter takeoffs mean less time for something to go wrong, like hitting an object in the sea or starting porpoising. Several flying boats are actually unstable, but avoid porpoising by accelerating through the unstable region before it becomes a problem. (Smith and White 1954)

During landing, hydrodynamic resistance is less important and can even be a good thing, slowing the aircraft down faster.

Dynamic stability refers to the stability in roll, yaw, and pitch, as well as heave, as the aircraft moves through the water. Especially instability in pitch and heave can be dangerous for seaplanes during takeoff and landing.

Spray is the water that gets pushed up and out from the hull as the hull moves through the water. This spray can seriously damage the propeller and control surfaces of the aircraft and needs to be minimized. Spray characteristic is an entire topic in itself and is considered outside the scope of this thesis.

Landing loads is the force on the hull during landing and is a big driver of hull strength and, thereby, hull weight.

In addition to these considerations, other factors like low-speed maneuverability also fall into the category of hydrodynamic performance.

2.2 Basic Seaplane Hull

Figure 2.2 shows the gradual change from a streamlined body (shape 1). In the second shape, the tail is swept up. This is also done on most land planes in order to give tail clearance to allow for rotation during takeoff and landing. For seaplanes, the tail is also swept up to reduce the spray that hits the tail, which increases the resistance. (Coombes and Clark 1937)

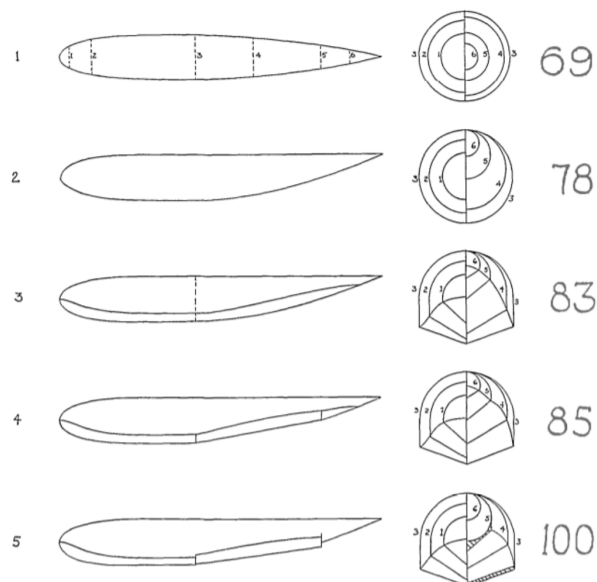


Figure 2.2: Gradual change from streamlined shape to a flying boat hull. The numbers to the right are the relative drag as a percentage of the full flying boat hull. Figure borrowed from (Coombes and Clark 1937)

Figure 2.2, shape 3 shows a hull with a sharp keel. The angle β , seen in Figure 2.3 is known as the deadrise angle. The sharp keel decreases water landing loads, adds lateral stability, and helps control spray at the cost of increased hydrodynamical resistance.

At the intersection between the hull and the fuselage there is also typically a sharp break, known as the chine. The chines helps reduce the spray. The hull may also have a concave shape, with a larger deadrise angle at the keel, which further decreases landing loads and reduces spray. This is known as flare. (Coombes and Clark 1937) (Thurston 1978)

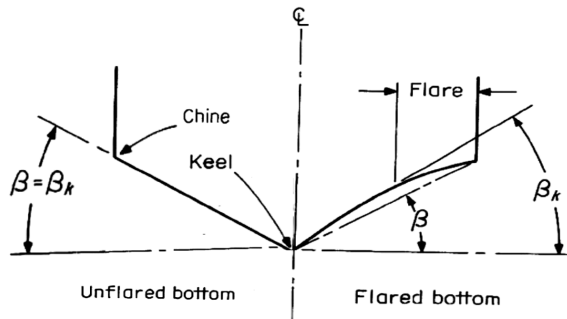


Figure 2.3: Illustration of deadrise angle, with and without flare. Image edited based on two original images from (Thurston 1978)

Figure 2.2, shape 4 shows the addition of sharp breaks in the shape around the mid and aft sections. This is done to create a flow separation for the water and spray to break clear of the aft body. Shape 5 adds a flat indent or plane, referred to as a step, to the discontinuity line in order to increase the breakage. This step is one of the major drivers of drag for seaplane hulls, and this is the main focus point of this thesis. Without the features in shapes 4 and 5, the shape would, in effect, create an upside-down airfoil in the water, causing water spray to fly upwards behind the body and, subsequently, creating a suction force that would pull the hull down into the water and prevent it from taking off. (Coombes and Clark 1937)

2.3 Take-off Performance

During stationary and low speed, the hull of a flying boat acts as a displacement hull. The weight of the water displaced equals the weight of the aircraft. During a takeoff, as speed increases, the hull starts to generate hydrodynamic lift, lifting the hull out of the water into a planning stage. As the speed increases further, the hydrodynamic lift is slowly replaced by aerodynamic lift until the aircraft reaches takeoff speed. These phases can be seen in figure 2.4. (deCallies 1967)

The point of maximum resistance occurs during the transition from displacement to planning,

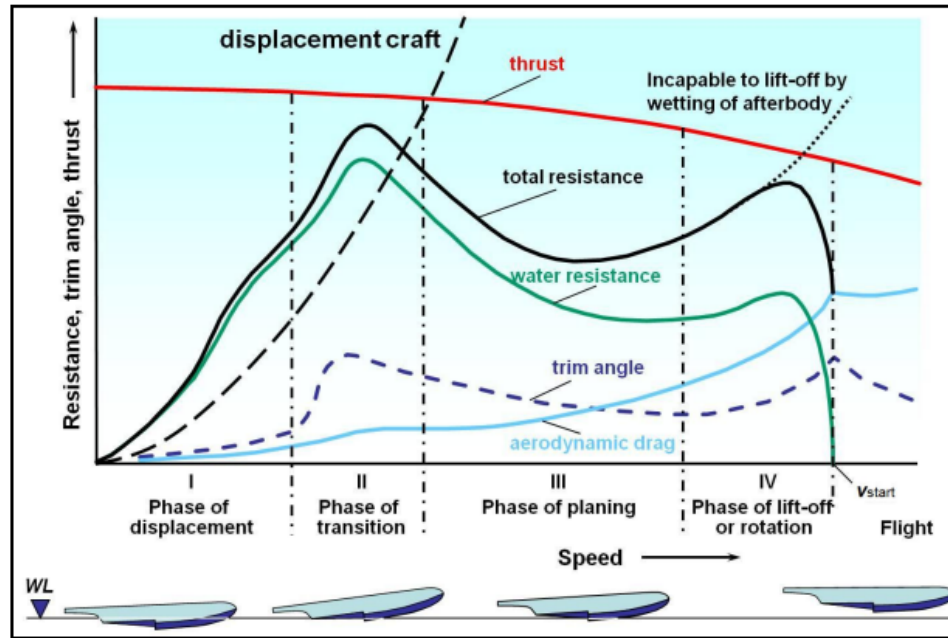


Figure 2.4: Phases during takeoff. Source of figure: Recolored by prof. E. Wilczek, based on data from Sottorf (1937)

as the aircraft is lifting itself out of the water. This point is referred to as the hump. A sharp increase in pitch (also known as trim) can be seen in figure 2.4 in this phase. Once the hull is out of the water, the pitch decreases, and the water resistance decreases again. (deCallies 1967)

Importantly, the available thrust must be larger than the sum of the resistance. The rate of acceleration will be the difference between the thrust and the drag over the mass of the aircraft.

2.4 Hydrodynamic Resistance

Each of the four phases introduced in section 2.3 comes with different mechanisms for hydrodynamic drag. Depending on which phase we want to optimize for, the design will differ. Some general trends do also exist, like deadrise angle, where hydrodynamic drag increases with increasing angle, especially for the planning phases (Sottorf 1937)

The following section is a general explanation of the hydrodynamic drag, in the four phases as shown in figure 2.4

In phase 1 the displacement phase, the flying boat hull creates relatively high drag compared to a more streamlined hull. This is not of great concern in terms of takeoff performance, however, as the excess thrust is large in this phase, leading to a fast acceleration into stage two. The drag in this phase does matter, however, if the aircraft is expected to see long taxiing runs. Combined

with the poor efficiency of the propeller in this phase, some energy could be saved by reducing the drag. During this stage, an air bubble will be drawn in by the negative pressure behind the step and start to reduce the wetted area of the after body, as seen in figure 2.5. (Sottorf 1937)

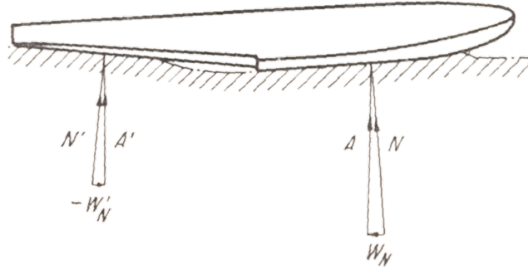


Figure 2.5: Hydrodynamic forces during displacement phase. Figure borrowed from Sottorf (1937)

In phase 2 the air trapped behind the step increases in length, while the impact pressure on the forebody increases, both working to move the center of pressure forward. This causes a pitch-up movement that increases the hydrodynamic lift, and the hull lifts out of the water. This lifting movement moves the center of pressure aft again, causing a pitch down once the hull is in planning mode. The maximum hydrodynamic drag will be somewhere in the region around the maximum pitch, and it is important to have sufficient excess thrust to overcome this resistance. (ibid.).

In phase 3 the hull is fully planning and only a small part of the hull in front of the step is in contact with the water. As speed increases, this patch of contact with the water decreases in size, caused by load shifting from hydrodynamic to aerodynamic lift from the wing. The decrease in contact with the water also moves the center of pressure further aft, slowly decreasing pitch.

In phase 4 the pitch has to increase in order to increase wing lift and lift the aircraft out of the water. This pitch-up increases the spray and drag on the aft body, as can be seen in figure 2.6. As the thrust curve also comes down at this point, a second critical phase occurs where drag could exceed thrust.

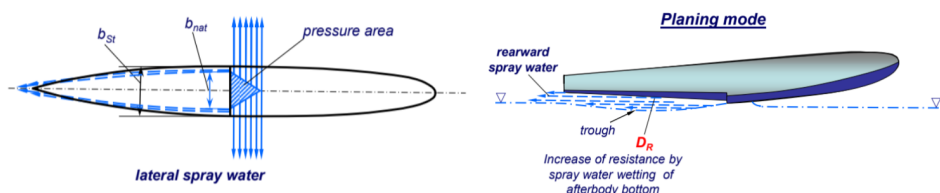


Figure 2.6: Spray aft of the step, onto the after body. Source of figure: Recolored by prof. E. Wilczek, based on drawing by (Sottorf 1937)

It should be noted that different hulls will differ in these characteristics. deCallies (1967) does

not report an increase in hydrodynamic drag during step four, most likely due to having looked at different hull geometries.

2.5 Dynamic Stability

When under very low speed or stationary, the center of buoyant forces vs the center of gravity and wind loads are the primary drivers of stability. At higher speeds, the hydrodynamic forces, and increasingly with speed, aerodynamic forces take over. This thesis will focus on the stability when moving, known as dynamic stability, as static stability is primarily a function of the overall hull width, the height of the center of gravity, and tip float size, neither of which is a focus of this thesis. The most critical factor for dynamic stability is the longitudinal stability. Here, there are two characteristics that can be critical for a seaplane during takeoff or landing: The following section is primarily based on the findings of Smith and White (1954), and Olson and Land (1942).



Figure 2.7: Illustration of severe porpoising leading to takeoff at too low speed, and subsequent stall and crash. Figure borrowed from FFA (2014)

Porpoising is an oscillating change in pitch, typically defined at a minimum amplitude of 2 degrees. Higher amplitudes may be acceptable, but this is dependent on duration, pilot skill, and the speed at which it occurs. The main danger of porpoising is increased stress on the airframe, increased spray, and premature takeoff with a subsequent stall. Generally, porpoising becomes more critical with higher speed. The instability may be self-sustaining or self-dampened. Some highly unstable seaplanes might start porpoising without the aid of external disturbance, while other planes require an external disturbance like a wave or sudden change in pitching moment from high-mounted engines to start porpoising. Smith and White (1944) report that porpoising seems to be more likely to occur during pitch-down rather than pitch-up disturbance. This effect has a bigger impact on landings, as the thrust line VS. dragline makes the aircraft more likely to have pitch-down moments during landing. (Smith and White 1954)

It is also important to consider the time component of instability. While one method to determine the stability limit is to run tests at a constant speed and measure instability, this represents the

real-world conditions poorly, as an aircraft may pass through an unstable range as long as the acceleration is sufficient to prevent instability from occurring. (Smith and White 1954) This makes the reduction of hydrodynamic drag one of the key ways to combat instability during takeoff.

Benson and Freihofner (1944) Benson and Freihofner (1944) tested the landing stability of a model of a flying boat where the depth of the step was reduced to zero by using a retractable step. This model was unstable in landings, but as long as the deceleration was sufficient, the instability oscillations would be acceptable.

Skipping is a form of porpoising that also includes a heave motion and is commonly encountered during landing. Skipping can have very severe consequences, as the aircraft may lift out of the water during these oscillations. If the speed is then below stall speed, the aircraft will stall and fall down to the water surface with a large force that may damage or destroy the airframe. (Smith and White 1954)

Trim limits determine within which range of pitch the seaplane will be stable. This is typically not a hard line, but instability is more and more likely to occur the closer to the line one gets. In addition, due to the time dependency, instability may also not occur if the lines are crossed briefly. (ibid.)

Because of the increased sensitivity during pitch-down disturbance, compared to pitch-up movement, as described above, trim limit graphs often come with one upper limit for decreasing pitch and one higher one for increasing pitch disturbance. (Olson and Land 1942)

Forebody Porpoising is caused by varying pressure on the forebody, just ahead of the step, within the area marked pressure area in figure 2.6. This occurs during planning at low trim, with little flow over the afterbody. During the hump region, the afterbody will normally prevent this type of porpoising, as the afterbody will be partially submerged and dampen any change in the center of pressure on the forebody. (Smith and White 1954) The primary design that affects the forebody porpoising is the area immediately in front of the step.

Forebody - afterbody Porpoising is a type of porpoising that only occurs if two steps are present, with the pressure area of the aft step oscillating. (ibid.)

Step Porpoising is a type of porpoising that is caused by insufficient flow separation behind the step. The water spray behind the step creates a suction force on the afterbody, which may

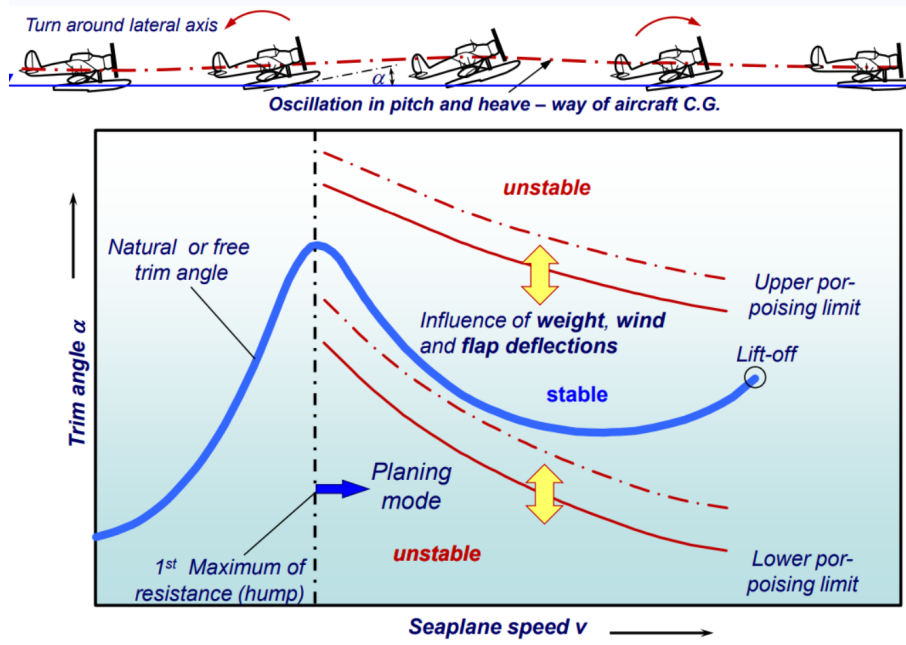


Figure 2.8: Example of plot of upper and lower trim limits along the takeoff profile for a seaplane. Figure borrowed from lecture held by prof. E. Wilczek (Wilczek 2021)

oscillate, causing oscillation in pitch. Skipping is a type of step porpoising. Afterbody shape and rise angle, known as sternpost angle, as well as the height and ventilation of the step, are the most important methods to reduce this porpoising. (Smith and White 1954) An example of the distribution of negative pressure aft of the step can be seen in Figure 2.9.

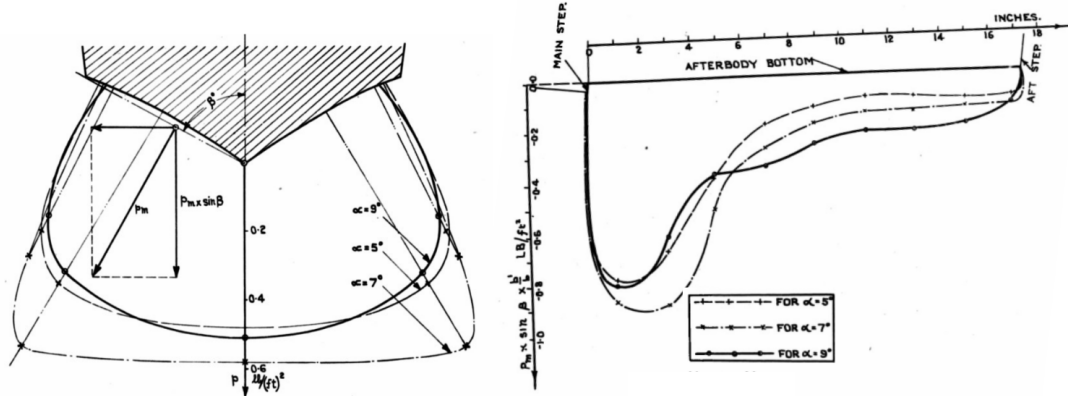


Figure 2.9: Distribution of afterbody pressure, as a function of sternpost angle. The left image shows the view of the frontal section. The right image shows a side view from the step extending rearwards. Figure borrowed from Tomaszewski, Smith and Chalmers (1946)

2.6 Hydrodynamic Loads

Load coefficient is a unitless coefficient for the concentration of hydrodynamic loads, often used for float and flying boat design.

$$C_{\Delta_0} = \frac{\Delta_0}{w \cdot b^3} \quad (2.1)$$

Where:

- * Δ_0 is the aircraft weight in [kg],
- * w is the specific weight of water [$\frac{kg}{m^3}$],
- * b is the width of the beam in [m]

3 Aerodynamic Theory

3.1 Fundamentals of Fluid Dynamics

3.1.1 Types of Flow

Fluid flow over a surface will be either one of two types: laminar or turbulent. With laminar flow, the fluid flows in the direction of flow, with very little motion or mixing in secondary directions. For turbulent flow, the flow will have internal eddies and vortices, creating a much more uneven and mixed flow. (Leishman 2024c)

3.1.2 Boundary Layer

When air flows over a surface, the air closest to the surface will stagnate and not move due to the friction forces between the fluid molecules and the surface. This is called non-slip. Further from the surface, the air will increase speed up to a point where the air is at free-flow speed. This layer of slower-moving air, affected by shear forces in the fluid, is called the boundary layer. The thickness of the boundary layer depends on many factors, like fluid viscosity, fluid velocity, surface roughness, surface geometry, and whether the fluid is in turbulent or laminar flow. (ibid.)

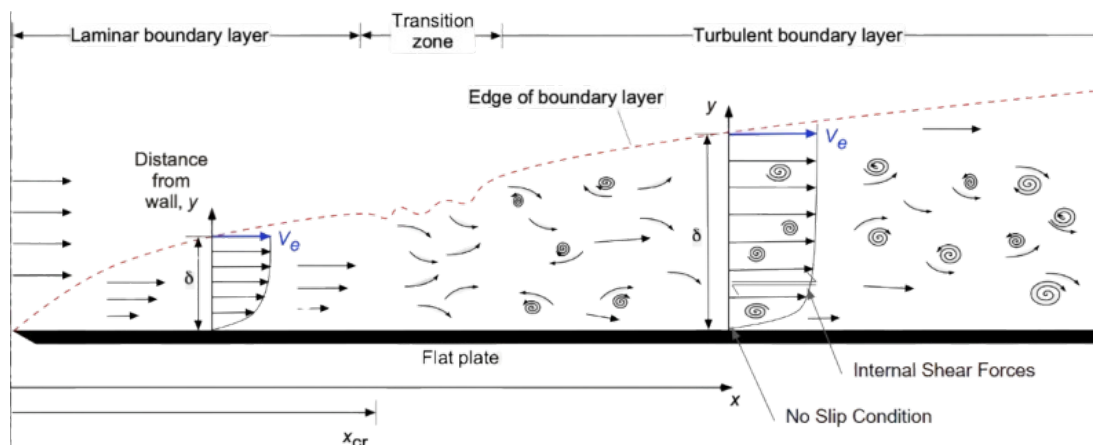


Figure 3.1: Development of turbulent flow over a flat plate. Image edited based on an original image by Leishman (2024c)

The thickness of the boundary layer is typically defined at where the flow speed is 99% of free flow speed, and denoted with δ , and can be seen in figure 3.1. For turbulent flow, the boundary layer will be thicker but also have a more uniform velocity profile due to mixing between the layers. (ibid.)

Due to the mentioned shear forces in the fluid, the boundary layer is where the friction drag

originates and is, therefore, a very important area to study. Turbulent boundary layers will generally have a higher aerodynamic drag than laminar ones. When designing aerodynamic surfaces where low drag is a benefit, it is, therefore, generally a good idea to try to keep the flow laminar as long as possible. (Leishman 2024c)

3.1.3 Flow Separation

Flow separation is when the flow is not able to follow the contours of the shape it flows over. Turbulent flow is more resistant to separation than laminar flow. Flow separation causes a large pressure drag behind the body, so turbulent flow may reduce drag. This feature can be exploited by aerodynamic design, which is why golf balls have dimples. As seen in figure 3.2, the dimpled surface causes a turbulent boundary layer, delaying flow separation. (ibid.)

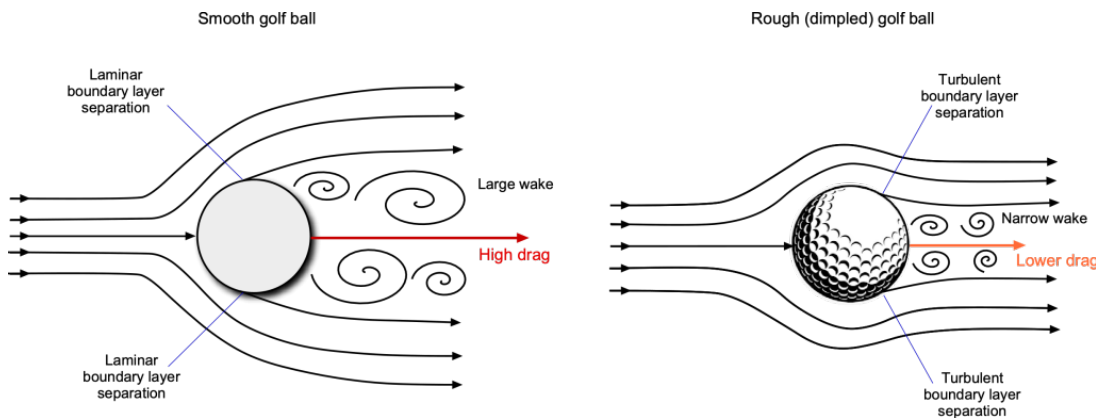
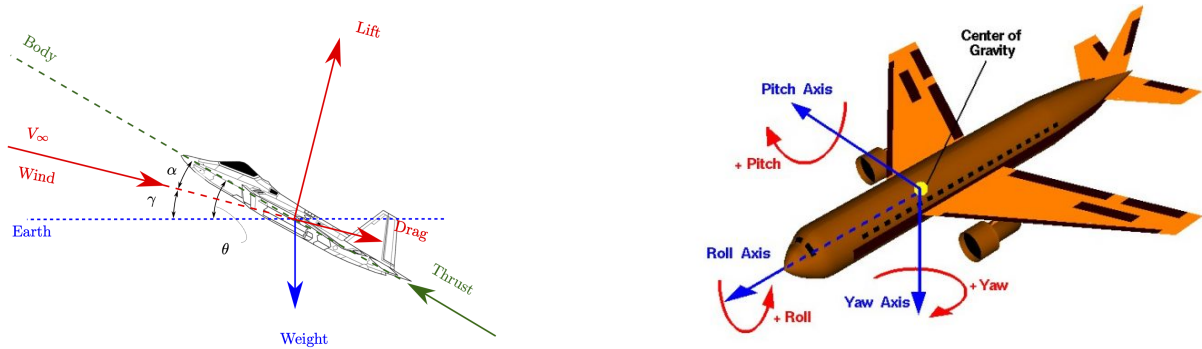


Figure 3.2: Flow around a smooth ball vs golf ball, illustrating the delaying effect of flow separation caused by turbulence. Figure borrowed from Leishman (2024c)

3.2 Fundamentals of Aerodynamics and Flight Physics

As an aircraft is not restrained to 2D motion and may move and rotate along all three axes, some definitions should be established about what coordinate system to use and which forces act in which axis system. There are four fundamental forces acting on an aircraft: Weight, Lift, Thrust, and Drag. (Leishman 2024b)

The three main coordinate systems when describing aircraft motion are the body, earth, and wind axis, as shown in figure 3.3a. Weight acts in the earth reference, lift and drag acts in the wind reference, and thrust acts in the body coordinate system. The angle of attack is defined as the difference between the body and wind axis. (ibid.)



(a) Coordinate systems for aircraft motion. Figure borrowed from Smith (2022)

(b) Definition of the rotational axis of an aircraft. Figure borrowed from NASA (2022a)

Figure 3.3: Coordinate and rotation axis for an aircraft

There are also three axes' of rotation, roll, yaw, and pitch, as seen in figure 3.3b. In this thesis, the pitch is sometimes referred to as trim.

3.2.1 Aircraft Drag

Aerodynamic drag is defined as the force opposing motion. The force does not act along the neutral axis of the body, as the thrust line does, but instead acts in the direction of the wind reference axis, as seen in Figure 3.3a. It is caused by the interaction between the air and the aircraft. (NASA 2022b)

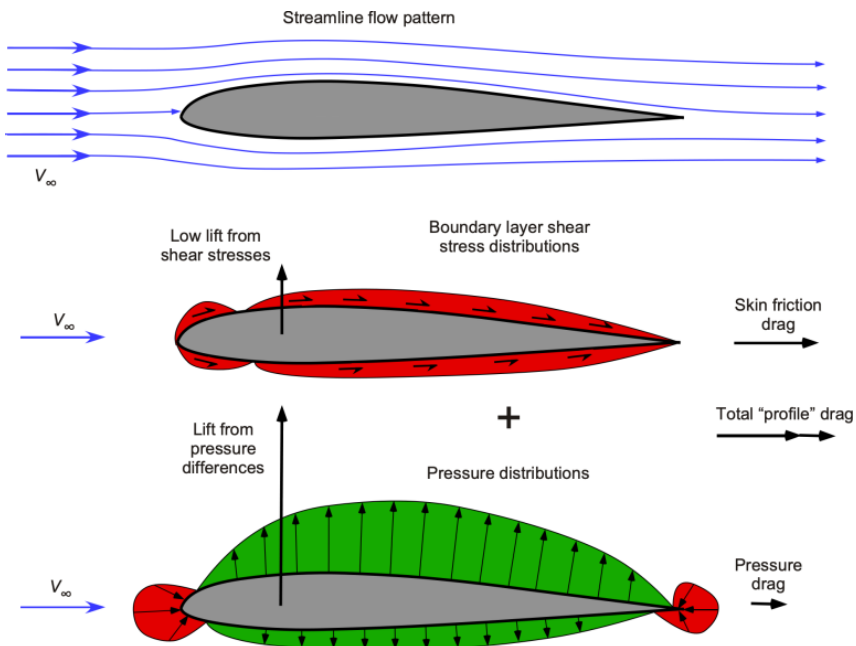


Figure 3.4: Aerodynamic forces acting on an airfoil. Image borrowed from: Leishman (2024a)

There are multiple ways to break down drag into categories, depending on what one wants to show. The physics-based breakdown breaks the drag down into pressure and friction drag, as

seen in Figure 3.4. As the name implies, the pressure drag is caused by higher pressures acting on the forward-facing surfaces than the rearwards-facing faces. This type of drag is related to the form and frontal area of the body. The skin friction is caused by shear forces in the boundary layer and primarily correlates with the surface area of the body. (Leishman 2024c)

Another common classification in aerospace is the difference between drag correlated with generating lift (induced drag) and drag not correlated with lift (parasitic drag). (ibid.)

3.2.2 Drag Coefficient

The drag coefficient is a dimensionless number used to compare the aerodynamic efficiency of shapes. Equation 3.1 is used to calculate this coefficient. The reference area used depends on the application and must always be checked. For simple shapes, it is common to use the frontal projected area or the surface area, while for aircraft, the wing area is typically used. (Ansys 2020a)

$$C_D = \frac{F_D}{\frac{1}{2} \cdot \rho \cdot V_\infty^2 \cdot A} \quad (3.1)$$

Where:

* D is the drag in Newtons

* ρ is the air density,

* V_∞ is the free flow speed of the air in [m/s],

* A is the reference area,

Drag coefficients are useful due to the fact that a similar shape with a different size will give the same drag coefficient. If one wants to compare the aerodynamic efficiency of two aircraft of different sizes, the drag coefficient is a good way to go about it, assuming the wing loading is similar. This can be seen in figure 3.5 where the two balls of 1:10 size difference have the same drag count.(ibid.)

If the reference area is sufficiently large, the drag coefficient becomes so small that it becomes hard to read, like 0.00323. In those cases, a more readable number may be used, called drag count. Drag count is $C_D * 10^4$ and means the aforementioned example would be a more readable value of 32.3 drag counts. (ibid.)

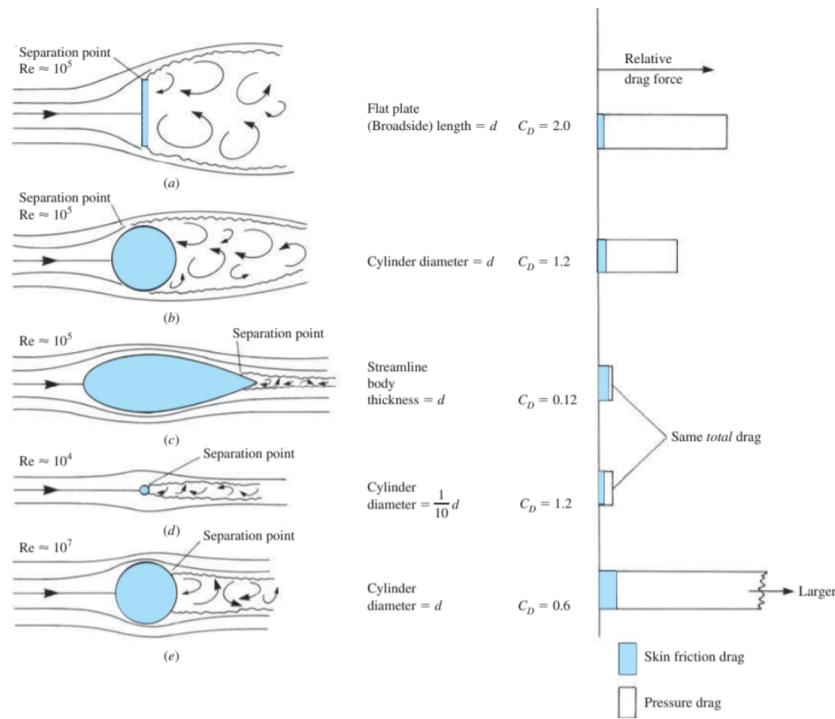


Figure 3.5: Drag of different shapes, broken down into pressure and friction drag. Different shapes can be seen to have very large variations in drag. Image has been edited based on two original images from (Talay 1975)

3.2.3 Drag Bookkeeping

It can sometimes be hard to know which category to place drag, as it may be a combination of features and factors that created the drag. One example is cooling drag that sometimes is counted as its own drag source, while in other cases, it is accounted for as a reduction of thrust of the motor. (Stauffer and Takahashi 2023) This becomes even more challenging if the outlet for the cooling duct is oriented in a way as to reduce the low-pressure zone of another system, thereby having a reducing component on another system's drag. (Wolf 2004)

For the step, the pressure drag directly behind the step easily contributes to the step. The increase or decrease of drag on the after body due to the turbulence and flow separation can, however, be harder to define but should most likely also be attributed to the step.

4 Literature study: Aerodynamic optimization

This chapter outlines the current literature on the aerodynamic impact and potential for improvements that can be made by refining a flying boat hull. Since the hulls used in the referenced tests vary significantly, this section serves as a baseline to identify trends, prioritize promising solutions for further testing, and provide reference values to detect and address any unrealistic test results. The results found in this section may not be thought of as directly applicable to the TAC1 hull without also being supported by a more targeted analysis. The chapter is divided into two main categories, step, and overall hull shape:

Step	Overall hull shape
• Step height	• Sternpost angle
• Step shape	• Tailcone upsweep
• Step fairing	• Deadrise angle and warp
• Step ventilation	• Length/beam ratio
	• Height/width ratio
	• Chines radius

4.1 Method

When researching flying boat performance, some challenges were quickly identified. Firstly, the number of sources on flying boat performance far exceeded what could reasonably be analyzed. Secondly, most of these sources were very old, primarily from 1930 - 1950. Newer sources existed, but these were primarily literature studies, using the older sources as primary sources. These literature studies did not always reflect the data from the primary sources well. Several errors and misrepresentations were found when looking at other literature studies. It was, therefore, decided to focus on primary sources where possible. A challenge in avoiding referring to the same test twice, as a lot of sources cited each other, was also identified.

The primary database of sources was found through the NASA Technical Reports Server (NTRS). The papers include research done in Germany, the UK, and the USA, which has been declassified and published.

4.1.1 Parametric Study of Drag

One good way to investigate the drag of certain features of a flying boat hull is to systematically vary one feature, keep the rest of the hull similar, and measure the change in drag from that one feature. This can give valuable data, but as drag from one feature can influence the flow over other features, it is not certain that when multiple features are changed, the change in drag will add up to the sum of the changes in drag expected based on individual tests. Wind tunnel testing by Riebe and Naeseth (1947b) found that fairing the step reduced drag by 12% while rounding the bow chines reduced drag by 5%. When both features were tested, the sum added up to 14% drag reduction, not the expected 17%.

4.2 Aerodynamic Impact of the Step

One important factor in determining the amount of design effort to allocate to each design feature is to estimate the impact and potential for improvement.

Prior to this thesis work, the drag contribution of the main step has been calculated to 16 drag counts internally by Elfly, which is estimated to be 6.8% of total parasitic drag or 133N at cruise speed. The method presented by Hoerner (1965) was used in this calculation. This corresponds relatively well with results from full-scale aircraft, where the step drag is typically found to be in the range of 2-3% of the full aircraft drag (parasitic and induced drag), considering this was calculated for a straight, non-faired step. (Benson and Havens 1945)

4.2.1 Step Height

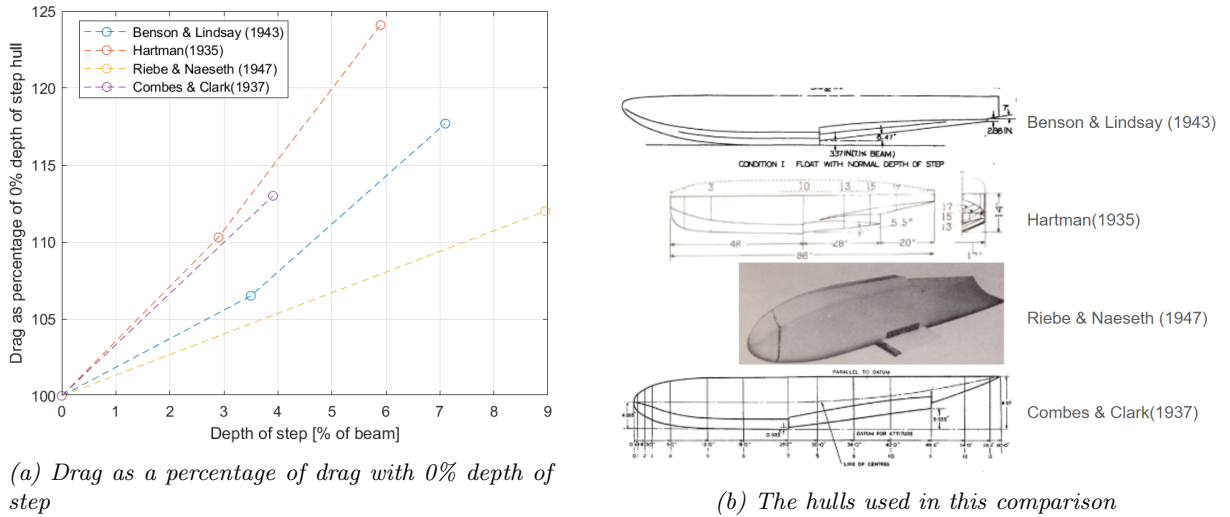
The typical depth of step for seaplanes is in the range of 5- 10% of the beam width. (Chicken 1999)

Effect on air drag

A summary of the aerodynamic drag vs step height as a percentage of the beam of four sources can be seen in Figure 4.1a. The hulls in the comparison differ significantly, as can be seen in Figure 4.1b. All the hulls are two-stepped hulls. However, the size and shape of the second step differ. The size of the model and the number of features, like wing stubs in the test by Riebe and Naeseth, will also affect the percentage a certain change in drag will make up.

The TAC1 hull is most similar to the hull tested by Benson and Lindsay. The 0% depth of step

used as a benchmark in that test still had a sharp break in angle.



(a) Drag as a percentage of drag with 0% depth of step

(b) The hulls used in this comparison

Figure 4.1: Collection of 4 different flying boat hulls, with wind tunnel test data investigating the drag related to the depth of the step

Effect on hydrodynamics

Impact on Stability: Olson and Land (1942) found that increasing the depth of step had no effect on lower limit porpoising but had a large impact on the higher limit porpoising, as seen in Figure 4.2. The figure also clearly shows the difference between decreasing trim and increasing trim limits, as discussed in chapter 2.5

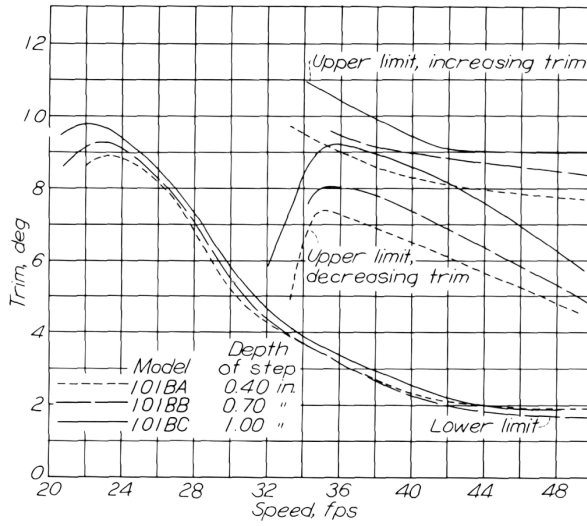


Figure 4.2: Trim limit as a function of step height and speed. Figure borrowed from Olson and Land (1942)

Impact on hydrodynamic Drag: Sottorf (1937) tested the hydrodynamic resistance with varying depth of step. The results can be seen in figure 4.3. Each depth of step had a different region, and it performed better or worse. In general, the higher the depth of step, the higher the resistance

at low speeds, and the lower the resistance at lower speeds. The lowest hump resistance came from the medium step heights.

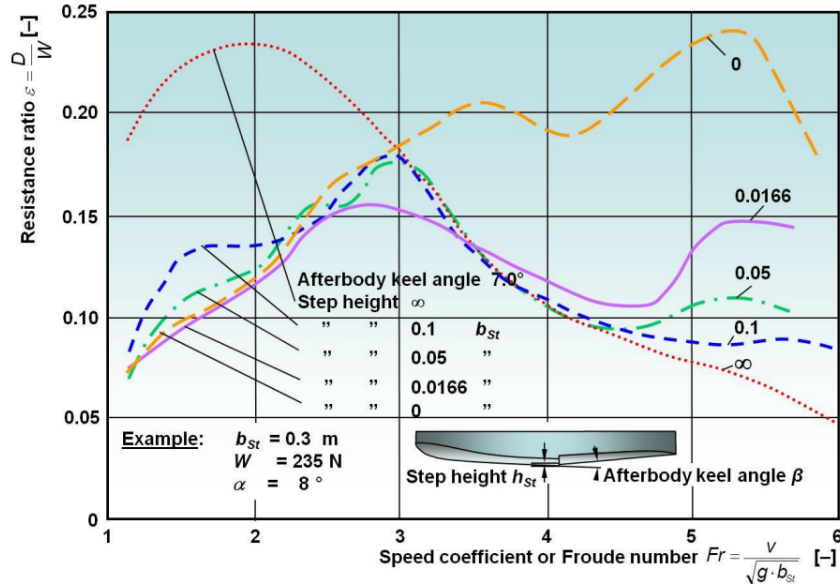


Figure 4.3: Hydrodynamic drag during takeoff run, as a function of step height. Source: Recolored in an unpublished report by Prof E. Wilczek, based on original data from Sottorf (1937)

A similar result was found by Benson and Freihofner (1944) when comparing the hydrodynamic resistance of a 5% of the beam and zero depth of step hull. The zero-step hull had lower resistance up until right after the hump. The resistance of the zero-step hull then continued almost linearly upwards, while the stepped hull had decreasing resistance after the hump.

4.2.2 Step Shape

The step of flying boat hulls may be straight, angled backward in a V-shape, or oval. An illustration of straight and V-shaped steps can be seen in figure 4.4. Angling the step backward will increase the effective depth of the step at the keel by a factor proportional to the sternpost angle.

Effect on air drag

Coombes and Clark (1937) investigated the change of air drag from angling the step and found that a 30° step had 4% higher drag than a straight step. If the angle was increased to 60%, the drag came back down to that of a straight step. The same trend was observed for oval-shaped steps, with the medium-angle shapes showing the highest drag. V-shaped steps will have a varying depth of step, which could influence the overall drag if not corrected properly.

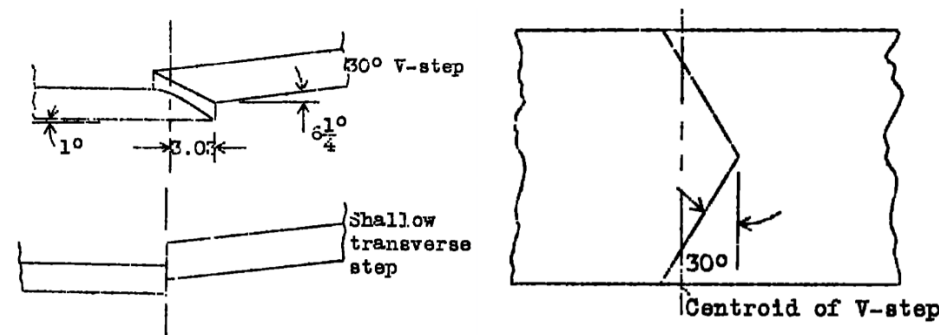


Figure 4.4: Illustration of Step Geometry. Top Left: V-shaped step from side view. Bottom Left: a straight step in side view. Right Figure, V-shaped step from bottom view. A straight step would go where the dashed line is located. Figure borrowed from Parkinson and Land (1944)

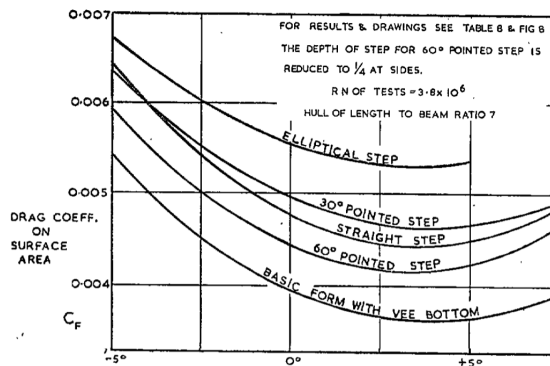


Figure 4.5: Air drag as a function of step shape and angle of attack. Figure borrowed from Coombes and Clark (1937)

The same conclusion was reached, that V-shaped steps have higher drag, by wind tunnel test conducted by Hartman (1935).

Effect on hydrodynamics

Parkinson and Land (1944) investigated the landing stability of V-shaped steps and found that a V-shaped step with 25% less frontal area than a straight step gave similar landing stability. Coombes and Clark (1937) mention that the hydrodynamic resistance is lower, although just marginally so.

4.2.3 Step Fairings

Several sources have investigated the addition of fairings on the step in order to reduce the aerodynamic drag while still having sufficient hydrodynamical performance. Coombes and Clark (ibid.) found the relation seen in Figure 4.6, by wind tunnel testing 18 different fared steps. The raw data from these tests, including sweeps on the angle of incidence, was published by Smith (1957). The wind tunnel tests found a 70% reduction of step drag with a 6 times the depth of the

step with a straight step fairing. This fairing, however, also increased the hydrodynamic drag during planning by 40%. A fairing from half the depth of the step could half the step drag, but it needed to have a length at least 15 times the depth of the step. Concave steps were not found to significantly reduce drag. The best trade-off was suggested to be with a fairing that started at 1/4 depth of step and extended rearwards 9 times the depth of step. This fairing halved the aerodynamic drag while only increasing the hydrodynamic drag at planning with 15%. No information on the stability of this fairing was given.

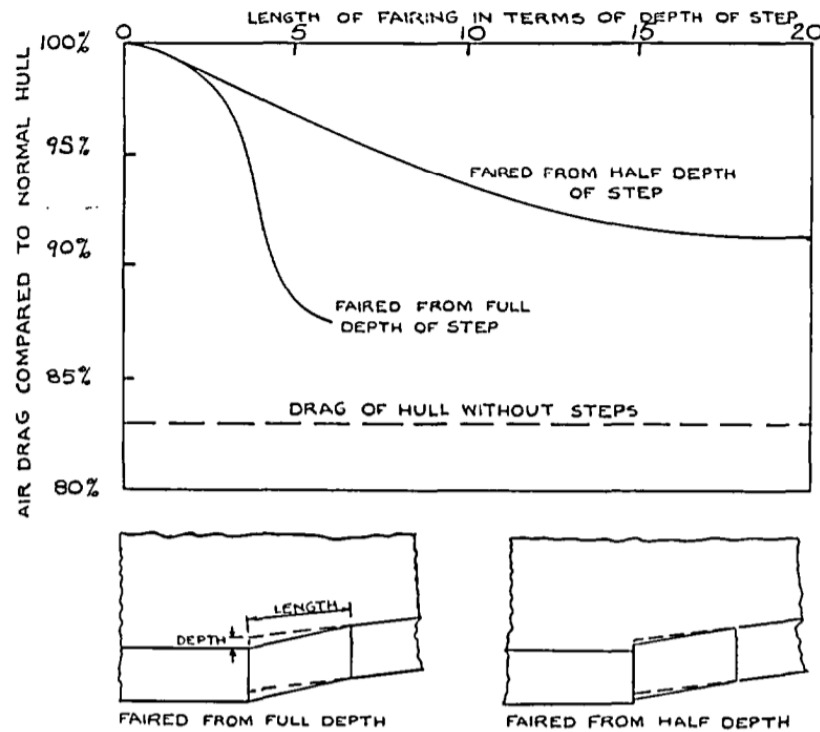


Figure 4.6: *Drag as a percentage of drag without step fairing over a range of fairing lengths.* Figure borrowed from Coombes and Clark (1937)

Benson and Havens (1945) investigated 15 different fared steps in a tank test with a scaled model of a 30-ton flying boat. Six of the fairings incorporated ventilation, discussed further in Chapter 4.2.4. This paper highlighted a step with 1% depth of step unfaired, with a relatively large ventilation (ventilation area 7% of the beam width squared) as favorable to a conventional step.

Hamilton (1956) tested several shapes of step fairings, as seen in Figure 4.7. The straight fairing 9 times the depth of step reduced the drag almost up to the hull without step. The concave fairing reduced drag by more than what was found by Coombes and Clark (1937) but still less than the other fairings.

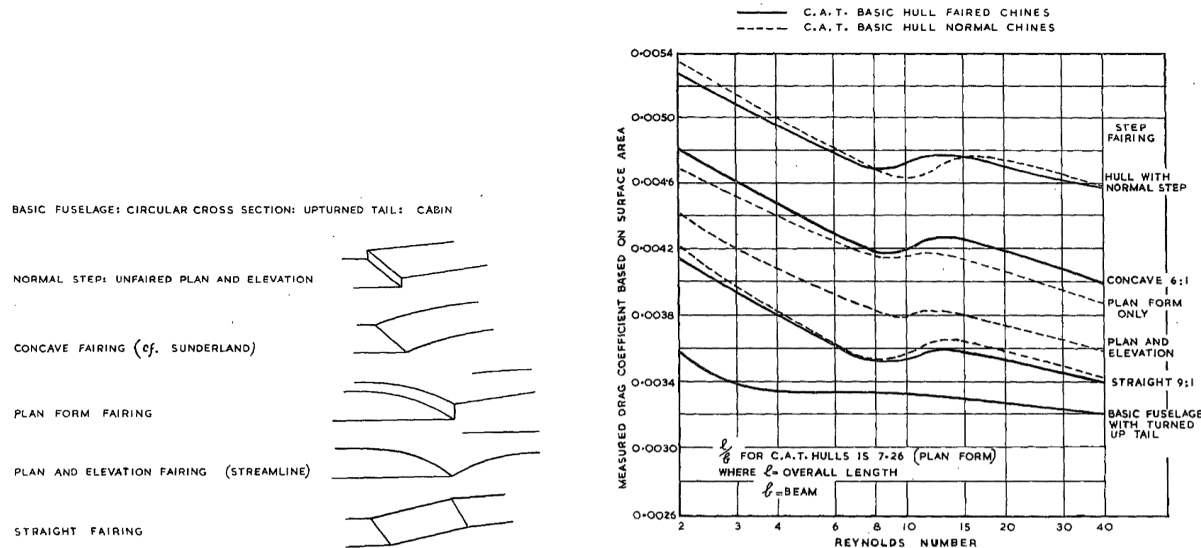


Figure 4.7: Drag coefficient of a flying boat hull with different step fairings, as a function of Reynolds number (10^6). Figure borrowed from Hamilton (1956)

Conway and Maynard (1943) tested a total of 6 fairings, both straight, convex, and concave. One of the concave fairings in this study had almost the same drag as a fully faired convex fairing. This concave fairing was chosen as a baseline for one of the concave fairings tested in the wind tunnel.

Plan and elevation fairings are fairings that curve in more than one plane, as seen in Figure 4.7.

Riebe and Yates (1947) investigated the three steps seen in Figure 4.8. The one-step hull seen in Figure 4.14, which is similar to the current proposed TAC1 hull, was also tested for comparison. The hull 221A had an 18% reduction in drag compared to the comparison hull, which had a drag coefficient of 0.0066. Hull 221C had a slightly less aggressive fairing, based on the same principle, and had a drag reduction of 12%. The single plan form step fairing had less than 2% drag reduction compared to the comparison hull. It should be noted that the comparison hull did not have a step fairing. Another paper by the same authors found a 15% decrease in aerodynamic drag by fairing the comparison hull with a straight fairing 9 times the depth of the step. (Yates and Riebe 1947)

These step fairings are very similar to the fairing on the Princess flying boat, a very streamlined flying boat that reached an impressive L/D ratio of 19. (Smith 1959)

These step geometries, although promising, were not chosen for the wind tunnel testing. This was due to the fact that they would require a larger modification to the hull than the straight and concave steps.



Figure 4.8: Hulls tested by Riebe and Yates (1947)

4.2.4 Step Ventilation

As discussed in Chapter 2.5, one of the main reasons for porpoising is negative pressure aft of the step. If the step is not sufficient to create an opening to let air into this region, air ducts can be added going through the fuselage to add ventilation and equalize the pressure in this region. This will increase the upper trim limits and reduce hydrodynamical drag. This negative pressure can be quite high and cause the aircraft to stick to the water, making take-off impossible. Dornier Do 18 flying boat measured 11.8 kPa negative pressure behind the step (Wilczek 2021) Tests with the Sunderland, a flying boat of the same size, measured a negative pressure of 27.5 kPa. (Hamilton 1956)

Hamilton (*ibid.*) investigated the effect of ventilation the step on the Sunderland flying boat. One key finding was that ventilation alone, when the step height was reduced to zero and rounded off, was not sufficient to reduce hydrodynamical resistance and instability. A full-scale investigation into the hydrodynamical behavior of a highly faired flying boat hull

As mentioned in Chapter 4.2.3, Benson and Havens (1945) found that stable landings could be made with only a 1% depth of step if the ventilation area was large enough. The source included the recorded heave and pitch data for all 15 steps tested, giving a good indication of the different degrees of porpoising and skipping observed. These tests were for a two-step hull and would have to be redone for the specific one-step TAC1 hull.

Forced ventilation

Some aircraft have experimented with the use of fans in order to push air into the region behind the step. This does work, although the amount of air needed makes it highly impractical. The Empire flying boat, a boat with a total weight of 20 metric tons, needed an airflow of about $11 \frac{m^3}{s}$. (Tomaszewski, Smith and Chalmers 1946) An investigation by Hamilton (1947) found no effect in forced ventilation, even for a much smaller, 2.7-ton aircraft.

4.2.5 Retractable Steps

When studying step design and the trade-off between hydrodynamics and aerodynamics, it can be tempting to solve both problems at the same time by making a movable mechanism to retract or extend the step, allowing for optimizing both air and water operation. Coombes and Clark (1937) was one of the first to discuss the possibility of extendable/retraceable step geometries.

Benson and Lindsay (1943) investigated the use of a retractable step. A reduction of 8% in hydrodynamic resistance, and 2-3% of aerodynamic resistance in flight was found

The drawback of a movable system is the increased complexity, weight, cost, and risk associated with a movable mechanism. The step also has to sustain very high loads during take-off and landings.

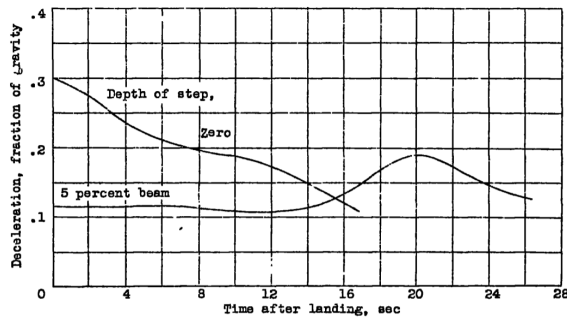
One of the most important factors in the feasibility of a movable mechanism is the criticality of failure. DO-254 specifies maximum failure rates based on the criticality of events, as seen in Figure 4.9. If safe landings can be made with the mechanism in the flight configurations, the criticality level would probably be classified as Minor. If the event could cause an unstable landing, the criticality level may increase to Hazardous. This may require the mechanism to have redundancy or, in other ways, increase the cost and complexity of the mechanism. (Mistral 2024)

Design Assurance Level	Description	Target System Failure Rate	Example System
Level A (Catastrophic)	Failure causes crash, death	$<1 \times 10^{-9}$ chance of failure / flight-hr	Flight controls
Level B (Hazardous)	Failure may cause crash, deaths	$<1 \times 10^{-7}$ chance of failure / flight-hr	Braking systems
Level C (Major)	Failure may cause stress, injuries	$<1 \times 10^{-5}$ chance of failure / flight-hr	Backup Systems
Level D (Minor)	Failure may cause inconvenience	No safety metric	Ground navigation systems
Level E (No Effect)	No safety effect on passengers/crew	No safety metric	Passenger entertainment

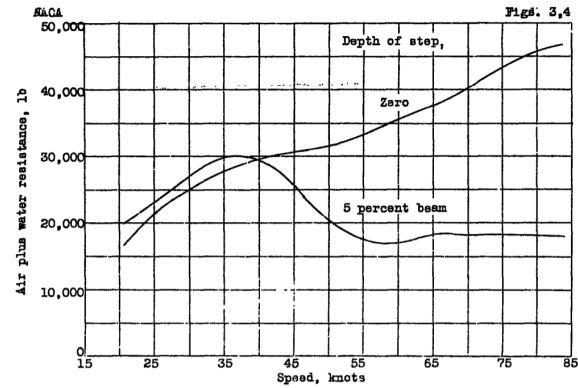
Figure 4.9: Design assurance levels in aerospace, according to the DO-254 standard, with targeted system failure rates. (Mistral 2024)

Benson and Freihofner (1944) investigated the landing stability and hydrodynamical resistance when landing with a step retracted to a 0% depth of step. This test showed a very stable landing between a landing pitch of 5.5° to 12°. High-speed landings at lower trim than 5.5° were stable only if the deceleration was large enough. If the deceleration was insufficient, the aircraft would trim up and take off again (skip). The deceleration curve of the model with and without the

step retracted can be seen in Figure 4.10a. Due to the higher hydrodynamical resistance without a step, the landing length was reduced by 50%, which was a potentially valuable feature in space-restricted areas.



(a) Deceleration of a hull with zero depth of step and 5% depth of step, after landing.



(b) Sum of air and water resistance, in lb, as a function of speed with and without a step, after landing.

Figure 4.10: Landing deceleration and resistance plots, when landing with and without step. Figures borrowed from Benson and Freihofner (1944)

4.3 Sternpost Angle

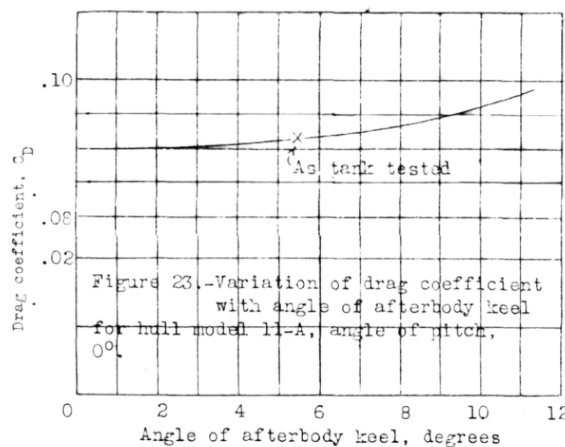
Sternpost angle is the angle of the fuselage after the step, as seen in Figure 2.1. For flying boats, this angle is typically in the range of 5° to 9°. (Locke 1946) This is done primarily to reduce the hydrodynamic resistance due to spray on the afterbody, but this angle also has a big impact on the hydrodynamic stability and air drag.

Impact on aerodynamics

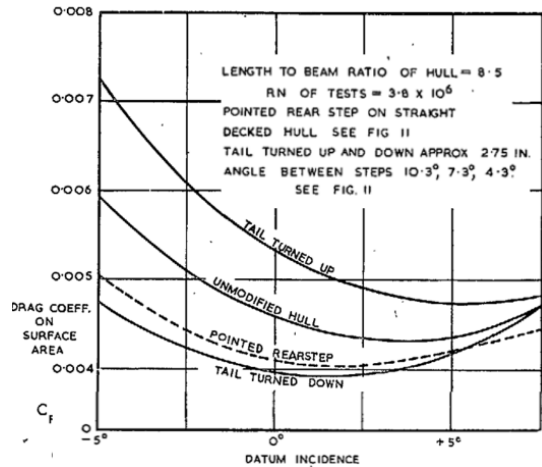
Coombes and Clark (1937) reported afterbody upsweep angle as one of the most significant factors in reducing flying boat drag. The data from these tests were published publicly by Smith Smith (1957) and can be seen in Figure 4.11b. A similar trend was found by Hartman (1935) and can be seen in Figure 4.11a.

From Figure 4.11b it can also be seen that the minimum drag does not occur at 0° of incidence. Notably, the optimal angle of incidence increases with increased afterbody upsweep.

This is a well-documented phenomenon, and it is not only a percentage in flying boats. Conventional land aircraft also have an upswept afterbody in order to give ground clearance to avoid a tail strike during take-off. (Torenbeek 1982)



(a) Air drag increases due to increasing angle of the afterbody of a flying boat hull. Edited image based on an original image from Hartman (1935)



(b) Air drag increase VS tail upsweep over a range of fuselage angles of incidents. Image edited based on original data from Coombes and Clark (1937), published by Smith (1957)

Figure 4.11: Ar drag vs angle of incidence

A similar effect as in Figure 4.11 can be seen in Figure 4.12. We can, therefore, be quite confident in the effect of this parameter on aircraft drag, although the magnitude may vary from aircraft to aircraft and is highly dependent on whether the flow separates or not. Flying boats are not helped in this regard, given that they already have a sharp discontinuity (step) where the change in direction occurs.

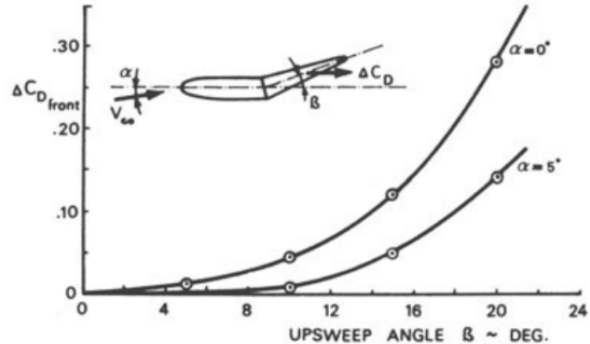
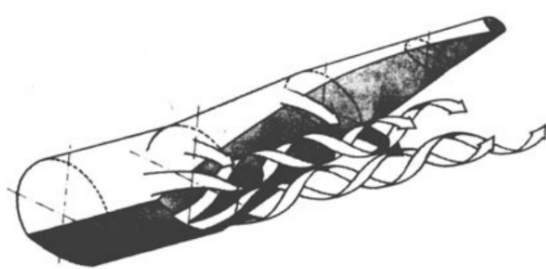


Figure 4.12: Effect of tail afterbody upsweep on land planes. Figure borrowed from Torenbeek (1982).

Effect on Hydrodynamics

Sottorf (1937) describes an increase in hydrodynamic resistance at the hump when increasing the afterbody angle from 7° to 9.5° . This could be due to the higher afterbody angle causing the aircraft to have a higher pitch due to the removal of buoyancy volume aft of the center of gravity, increasing the resistance prior to planning.

The hydrodynamic drag during planning was reported to decrease slightly with increased

sternpost angle. (Sottorf 1937)

Afterbody angle also greatly influences the upper limit stability, which is the proposing type known to cause skipping. Figure 4.13 shows the stability against skipping of a collection of full-scale flying boats as a factor of beam loading (described in 2.6, sternpost angle, and step height. Higher step height can be seen to decrease skipping while increasing the sternpost angle or beam loading will increase the tendency to skip. In order to avoid skipping, Locke (1946) recommends to stay above the dashed line. The data is derived from pilot interviews, where the pilot experience was used to adjust the rating of stability.

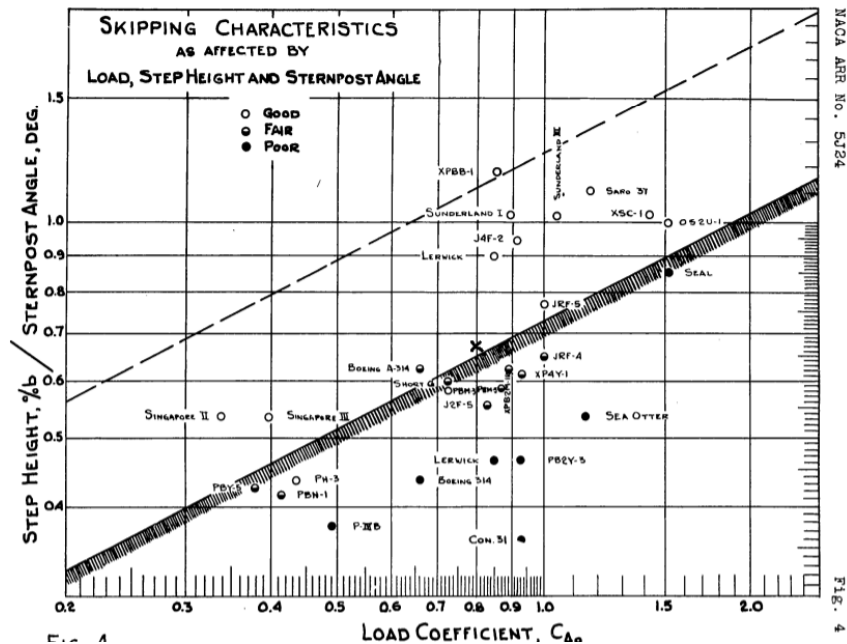


Figure 4.13: Stability against skipping, as a factor of beam loading, sternpost angle and step height.
Figure borrowed from Locke (1946)

4.4 Conventional VS. Planning Tail Hulls

Most of the sources in this chapter have done their testing on two-stepped hulls, often with the rear step being pointed (highly faired in the plan form) as per the definition of Figure 4.7. These hulls often also have a lower sternpost angle than one-step hulls.

Riebe and Naeseth (1947a) tested a one-step hull, modified from a model originally made as a two-step hull, seen in Figure 4.14. The drag was reported as "about the same". The tests were done at the same lab, at the same Reynolds numbers, but in different studies.

The TAC1 hull, on the other hand, is designed to have a one-step hull. This is mainly due to the advantage this step type gives in hydrodynamic resistance, especially around the hump speed.

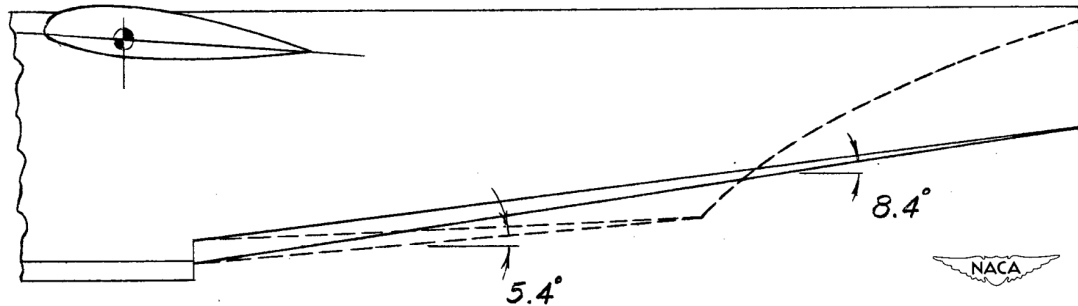


Figure 4.14: The difference between two step VS. one step flying boat hull. Figure is of Model 203 from the Langley tank facility. Figure borrowed from Riebe and Naeseth (1947a)

A plot of this decrease, as tested by Sottorf (1937) can be seen in Figure 4.15. A very similar reduction in hydrodynamic drag was found by Dawson, Walter and Hay (1946)

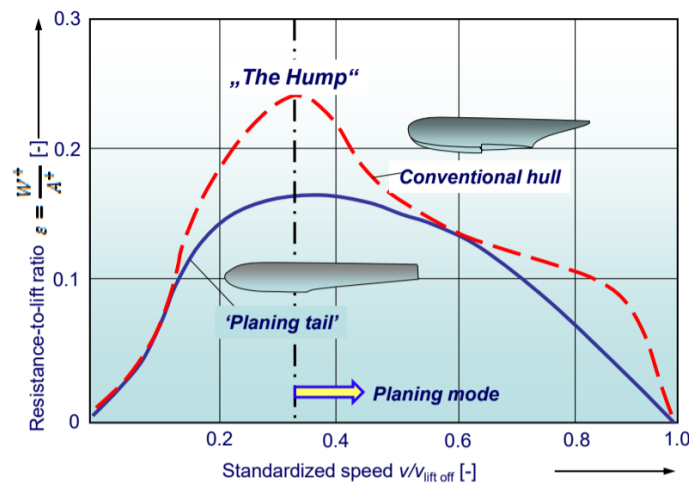


Figure 4.15: Comparison of hydrodynamic resistance for a two-step (labeled conventional hull) and the one-step hull (labeled Planing tail). Source: Recolored by Prof. E. Wilczek, based on original figure from Dawson, Walter and Hay (1946)

4.5 Length/Width Ratio

Coombes and Clark (1937) investigated the effect of length-to-width ratio on flying boats. And found a clear drop in drag coefficient with higher length-to-width hulls when using the surface area as the reference volume. The same trend was found by Riebe and Lowry (1948). It should be noted that the difference is biggest when going from a ratio of 6 to a ratio of 9, while the effect beyond 9 is lower, as surface friction drag then starts to increase significantly. The volume inside these thinner fuselages is also lower.

4.6 Height/Width Ratio

Coombes and Clark (1937) republished results from a test done at an unspecified NACA wind tunnel on varying the height of a flying boat hull. As expected, the drag increases with increased height as both frontal area and surface area increase. The increase was, however, quite linear, with a gradient of 1% increase in drag for every 2% increase in height. This trend, in combination with the trend on length/width ratio, explains why many seaplanes have been relatively long, tall, and slim.

4.7 Chines Radius and Flare

The chines and flare of the hull are methods to control spray but add a certain amount of aerodynamic drag. Combes and Clark(1937) report a 5% increase in drag from adding flare, but it is not specified how much flare other than visually by the image in Figure 4.16.

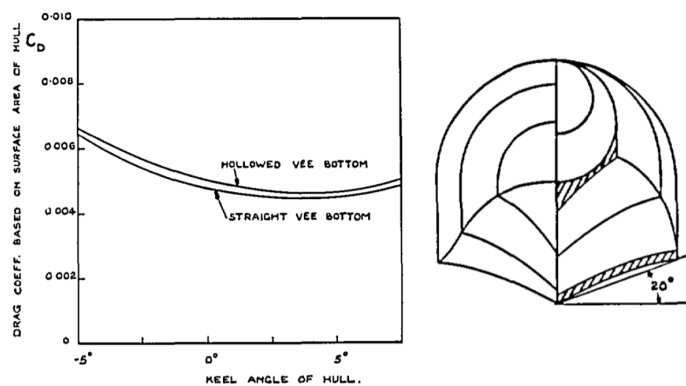


Figure 4.16: Effect of flare on air drag, as a function of angle of incidence. Figure edited based on two figures from Coombes and Clark (1937)

Coombes and Clark (ibid.) also found a 1% decrease in aerodynamic drag possible by rounding the chines with a radius, with the benefit flattening above a radius of about 10mm. This test's results were very dependent on the Reynolds number, as the flow boundary layer would be tripped by the chine if not already turbulent. Initial testing at Reynolds numbers between $3.8 \cdot 10^6$ to $6.3 \cdot 10^6$ initially found a 2% decrease in drag when rounding the chines, but increasing the Reynolds number to 10^8 in later tests saw the impact half for the same radius's.

A later test by Riebe and Naeseth (1947b) found a 5% reduction of drag by rounding the chine radius. This test was done at a Reynolds number of $2.4 \cdot 10^6$, but the boundary layer was tripped at 5% of the length of the hull, so the effects seen by varying the Reynolds number should be a lot less than what was seen by the untripped airflow tested by Coombes and Clark (1937).

4.8 Impact of Deadrise Angle

Deadrise angle, angle β as seen in Figure 2.3, has the biggest impact on the hydrodynamic performance, especially the hydrodynamic resistance to get up to and during planning, but it also affects the aerodynamic drag. The direct impact was tested for a set of floats by Parkinson, Roland and House (1939), which found that a higher deadrise angle led to a higher drag coefficient when using the volume as a reference. Coombes and Clark (1937) found an 11% decrease in overall drag when changing the deadrise angle from 20° to 30° .

Figure 4.17 shows the impact the deadrise angle has on hydrodynamics and loads. This trade-off is typically the driving factor behind the choice of deadrise angle due to its relatively larger impact.

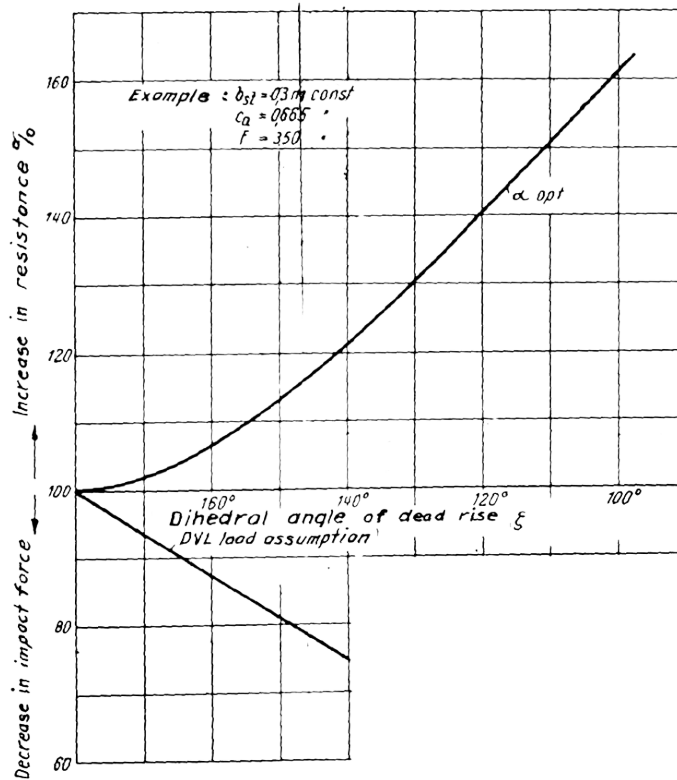


Figure 4.17: Hydrodynamic resistance and landing loads as a function of deadrise angle. The graph is given in deadrise dihedral angle α , not the typical definition of deadrise angle as described in Figure 2.3. Figure borrowed from Sottorf (1937).

4.8.1 Deadrise Angle Warp

Hugli and Axt (1951) found that warping the afterbody deadrise by increasing the deadrise from 20° at the step up to 35° at the middle of the afterbody, before bringing it back to 20° at the stern, significantly improved hydrodynamic performance. This allowed for the step to

be decreased from 8.3% down to 4.2% of the beam, with similar hydrodynamical performance. As discussed in Chapter 4.2.1, the step drag is roughly proportional to the step height. This improvement would, therefore, most likely be half the step drag.

4.8.2 Afterbody Steps

One of the main drivers of hydrodynamic drag during planning is the spray on the afterbody. One very effective way of reducing this drag is by separating the spray by the addition of auxiliary steps behind the main step. Sottorf (1942) found a 3° increase in upper limit stability by the addition of these steps, as seen in Figure 4.18.

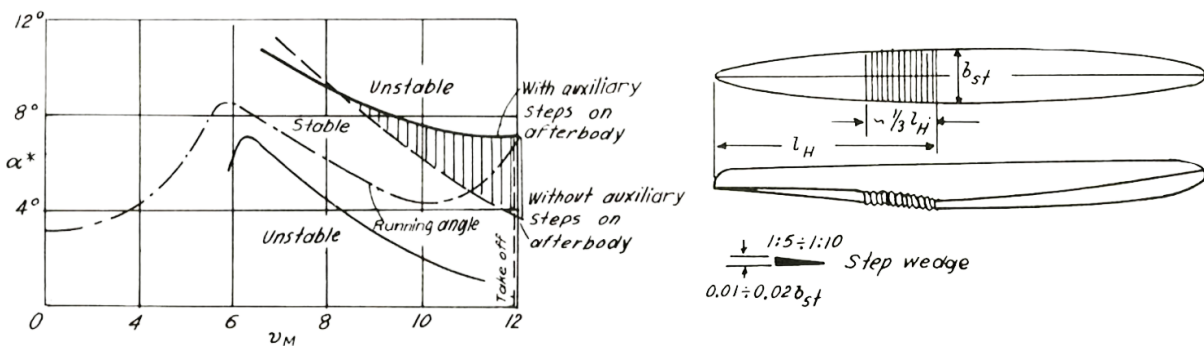


Figure 4.18: Increase of stability limit due to addition of smaller steps behind the rear step. Figure edited based on original from Sottorf (1942)

Wilczek (2021) also reports a potential to reduce the hydrodynamic drag right before take-off by up to 45% by the addition of auxiliary wedges, but the primary source was not directly cited, so no further details are known. In more modern aircraft, the Beriev A-40 from 1986 implemented auxiliary steps, as seen in Figure 4.19. This feature is especially interesting as it is outside the main region of hydrodynamic forces and, therefore, might be easier to make retractable with actuators.

4.9 Results Literature Study

Based on the literature reviewed, step-faring geometries were considered the most promising option to reduce the drag of the TAC1 flying boat, potentially in combination with step ventilation to increase hydrodynamical performance.

Auxiliary afterbody steps could be an attractive way to improve the hydrodynamical performance of a highly faired step further; however, it is not considered a viable option if it is not made retractable. Therefore, testing the aerodynamic drag would not be of a big significance.



Figure 4.19: Afterbody step on Beriev A-40. Source: Wilczek (2021), unknown original source

Sternpost angle was chosen as the second most important factor in getting good aerodynamic data due to its combination of large impact on aerodynamic drag and relatively lower impact on hydrodynamic performance.

The angle of incidence of the hull was seen as a third big improvement.

Chine radius showed varying degrees of drag reduction in the sources, but the negative effect this feature would have on the spray characteristics was considered outside of the topic of this thesis, and this feature was, therefore, not included in further testing.

5 Wind Tunnel

Based on the results from Chapter 4, it was decided to investigate the most promising features in order to determine the aerodynamic drag reduction possible by changing these features. Wind tunnel testing is a resource-intensive test method, but the large deviations between many of the hull shapes in the literature study VS. the TAC1 hull meant that many of the results from the literature were not directly transferable. Wind tunnel testing was initially chosen over CFD due to the author's lack of experience with CFD.

5.1 Test Objective

The primary test objective was to acquire data on the relative drag difference between different faired steps. This data will then be used, together with data from hydrodynamic testing, to make an informed decision on the step fairing design.

This test being about relative differences is important for the test setup, as it means that if the results are slightly off due to, for example, a low Reynolds number, the comparative results will still be similar. The usefulness of displaying the comparative results as a percentage of the full fuselage drag means that the test should also aim to get the right fuselage drag, but the accuracy could be lower than for factors affecting the relative difference between the geometries.

As discussed in Chapter 4.2.3, Coombes and Clark (1937) describes a non-linear relationship between fairing and drag reduction. Due to this, 11 step geometries were chosen, divided into three series of step geometries, each varying one variable at a time. Based on recommendations from Barlow, William and Pope (1966), a minimum of four geometries per test series was chosen so that the loss of any one test sample would still yield a correlation graph. In addition, two concave and one convex fully faired geometry and one without fairing were chosen, bringing the total geometries to 14.

The series' were as follows:

- Straight Faring, 0% depth of step. Lengths varying from 2 to 8 x the depth of step.
- Straight Faring, 1% depth of step. Lengths varying from 4 to 10 x the depth of step.
- Straight Faring, Length 6 x depth of step, varying starting depth from 0% to 3%.

Each fairing was tested at an angle of attack from 0° to 5°

The tested geometries can be seen in appendix A.

It was chosen to only test two angles of afterbody. This was due to the difficulty and time required to make this extension part. The current designed upsweep angle was chosen as the base case, and a neutral upsweep angle was chosen as a second geometry in order to measure the drag penalty of the upsweep.

5.2 Test Facility

The wind tunnel used in the test is the large-scale wind tunnel at NTNU, which has a cross-section of 2.7m x 1.8m and a maximum speed of 16 m/s. For reference, the full-scale aircraft is designed to cruise at 51 m/s at 1219 m altitude.

The wind tunnel used in this thesis is a closed-loop wind tunnel, similar to the example seen in Figure 5.1. This type of wind tunnel requires a smaller motor and less power than a straight, open wind tunnel, as the kinetic energy of the air is maintained. The NTNU wind tunnel required about 54 kW just to maintain the airspeed at 16 m/s. This power is mainly dissipated in air friction, heating up the air. Some larger wind tunnels have active water-cooled radiators to deal with this. The NTNU wind tunnel does not have active cooling. On the day of testing, the air started out at 17°C, and heated up to about 28°C before stabilizing. This temperature change will change the air properties and must be accounted for.

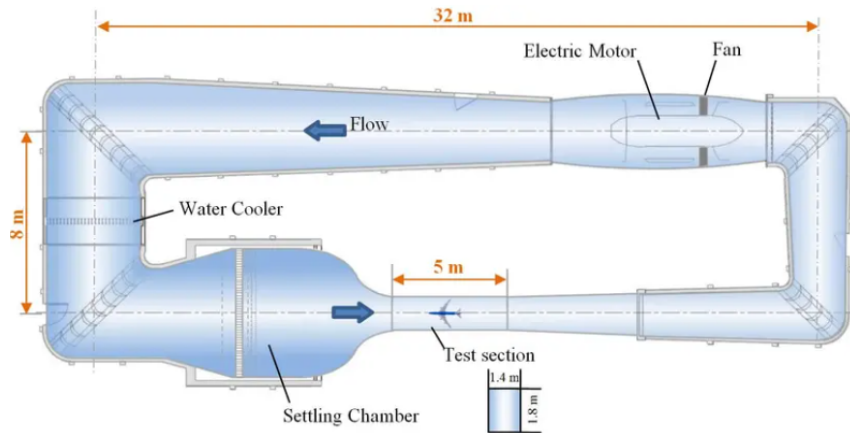


Figure 5.1: Overview picture of a closed loop wind tunnel, image from www.onera.fr

5.2.1 Data Acquisition

For the test proposed, the primary metric of interest is the drag force. More specifically, the relative change in aerodynamic drag was the most important factor. The small change in drag

between the different tested geometries required a precise measuring method.

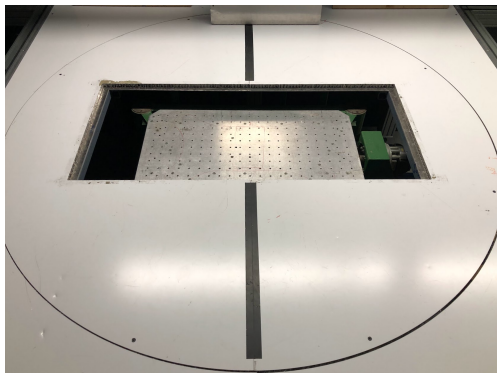
Prior to the test, the full-scale aircraft drag of the features tested was calculated to 80.9 drag counts, with wing area as the reference area. The drag force expected can be found by reversing the drag coefficient equation 3.1 to solve for the drag force, and using $V_\infty = 16m/s$, $\rho = 1.228kg/m^3$, and $A = 0.357m^2$.

This gives an estimated drag force for the model of 0.454 N, or 46.3 grams. The drag due to the step was estimated to be in the range of $\pm 10\%$, or ± 4.63 grams.

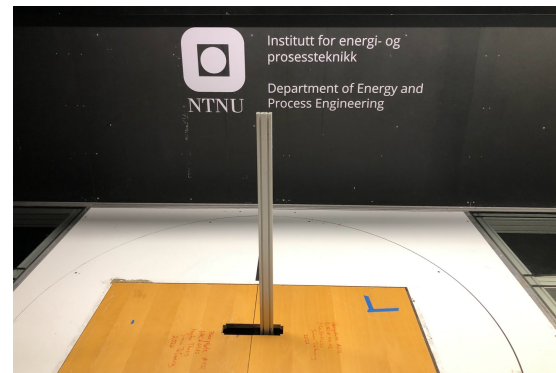
Force Measuring

The wind tunnel is equipped with a six-component force balance sensor that has a stated accuracy of $\pm 10mg$. (Larsen 2021). This would make the error due to the force balance around 0.22% of the difference due to the step geometries. The force balance is completely isolated from the main body of the wind tunnel, in order to reduce vibrations.

Measurements of forces were made with 5Hz frequency over a period of 30 seconds in order to cancel out any fluctuations.



(a) Mounting plate for the force balance sensor, with the rotatable section around it



(b) Strut used to mount the model to the force balance sensor

Figure 5.2: Setup for mounting the model to the measuring equipment

Airspeed

The airspeed inside the tunnel was measured using a pitot tube exposed to the free-flow air and converted to airspeed using Bernoulli's equation. The pressures were measured using a Setra Model 239 differential pressure transducer with a stated accuracy of $\pm 0.073\%$ of full-scale reading.

5.3 Model Design

5.3.1 Model Scaling Theory

When doing wind tunnel tests, it is often not feasible to test the model at full size due to economical reasons. Scaled-down models are then used, but the difference must be accounted for.

Reynolds Number

The Reynolds number is a dimensionless number used for aerodynamical compassion. Two flows with the same Reynolds number will give similar results. As seen in the equation for the Reynolds number 5.1, if the size is reduced, the fluid velocity must increase by a similar fraction, keeping the other fluid variables constant. This is often not possible due to cost or physical limitations like the speed of sound.

$$Re = \frac{\rho \cdot u \cdot L}{\mu} \quad (5.1)$$

We are then left with two options: changing the fluid parameters or accepting lower Reynolds numbers. Some of the wind tunnel tests referred to in this thesis were tested in compressed air tunnels. Another method is to use other mediums, like cooled nitrogen or water.

5.3.2 Model Size

The model was initially sized to fit in a smaller, $0.5m^2$ wind tunnel at NTNU, with a wind speed of 35 m/s. The model size was chosen to balance blockage percentage (see chapter 5.4.1), model build effort, and Reynolds number. This analysis gave a size of 9% of the full scale, which would have given a blockage factor of 7.5% and a Reynolds number of 6.7% of the full scale. A comparison between the model size and scale model can be seen in Figure 5.3 Material requirements generally scale with the size cubed, while the Reynolds number only scales with size squared, so an increase in Reynolds number by increasing the size above this would quickly have become very resource intensive.

Two weeks prior to the testing, it was decided to switch to a larger wind tunnel with lower top air speed due to the increased availability of measuring equipment, mainly a digital six-component force sensor and a rotatable floor, allowing for automatic and precise change in angle of incidence,

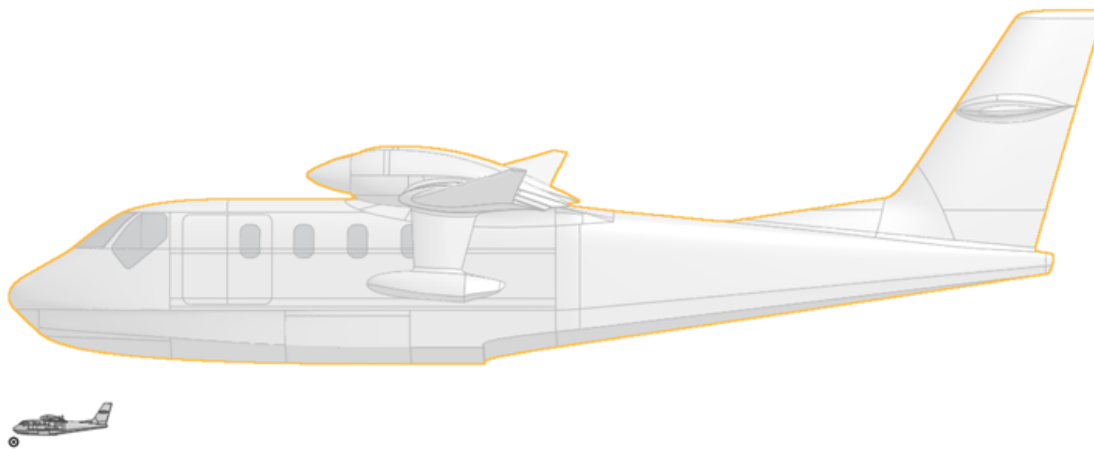


Figure 5.3: Scale Comparison between 9% model and full scale aircraft

as seen in Figure 5.2. The smaller wind tunnel only had an analog force sensor.

It was chosen not to rescale the model, even though a much larger model, up to 29% of full scale, could now fit with a blockage ratio below 10%. With the new wind tunnel, the Reynolds number was reduced from 6.7% to 3.0% of full-scale cruise Reynolds number due to a decrease in tunnel airspeed. The new Reynolds number was $1.43 \cdot 10^6$, when using the length from the bow to the step as the characteristic length. This Reynolds number is high enough for the flow to be turbulent.

It was recognized that this could affect the accuracy of the measurements, but it was believed that actively tripping the boundary layer and having access to more accurate measuring equipment would make up for this increase in Reynolds number difference. This difference in Reynolds number would make the flow more prone to detaching, but this can then be seen as a safety margin to the real-world case. If the flow stays attached in the wind tunnel, it is more likely to do so in real life. The Reynolds number will also affect the losses due to skin friction, and this will act in the opposite direction, increasing drag with a higher Reynolds number. (Ansys 2020a)

Because of this, the C_D plotted against the Reynolds number will often follow a pattern similar to that seen in Figure 4.7. Notably, the relative difference between the fairings in this figure does not change significantly. (*ibid.*)

A Reynolds sweep from 5 m/s up to 16 m/s was also planned in order to check the variability in C_D due to the Reynolds number.

5.3.3 Model Design and Production Method

Some design goals were set for the model used in the wind tunnel testing:

- Barlow, William and Pope (1966) suggests that the form similarity of the fuselage should be within 0.25 mm of the intended position for a model with a wingspan between 1.8m to 2.4m in low-speed wind tunnels. The scale model in this thesis would have had a wing span of 1.89 m if it had wings and, therefore, falls into this size category.
- Model stiffness should be sufficient to avoid bending of the model, larger than the form similarity goal above. This was achieved with internal extruded aluminum members. These members also allowed for accurate alignment of the sections.
- Quickly interchangeable step geometries were required to be able to quickly test many different step geometries. A sliding mechanism without any bolt holes was chosen.
- Interchangeable afterbody angle was required according to the test plan. As only two geometries were to be tested, it was considered sufficient to bolt them to the model.
- Due to the chosen size, transport without disassembly would be challenging. A design that allowed for splitting the model in half was set.
- Wing and tail mountings were added to make it possible to mount wings and full tail to the model at a later stage. This allows the model to be reused for other tests or marketing, reducing waste.

Historically, wind tunnel models have mostly been made from wood or milled aluminum. (ibid.) For this thesis, 3D printing was chosen due to the accessibility to a 3D printer at Elfly. This printer is a Bambu x1 printer with a build volume of 250x250x250 mm. This meant the model had to be cut into sections in order to be printed. This production method will give a model with a lower stiffness, geometric accuracy, and higher surface roughness than what could have been achieved with aluminum as a trade-off against less resource-intensive production. The aforementioned form similarity, stiffness, and surface roughness goals were considered achievable with 3D printing.

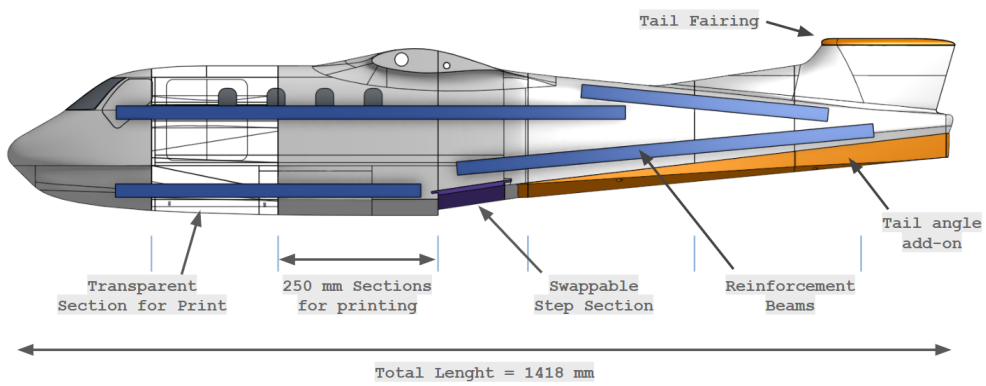


Figure 5.4: CAD Render of the model used in wind tunnel testing. The figure shows the sections the model was printed in, the interchangeable parts of the model, and the stiffening aluminum beams running the length of the model



Figure 5.5: Model in the process of being assembled. The rear section assembled, while the front sections are in the background

The model was made hollow before printing, reducing both required material and print time by about 70%. The walls were made 10mm thick, with three printed layers on each side and 15% infill between. The material used was PLA due to its low cost and sufficient strength for the application.

Surface Roughness

Barlow, William and Pope (1966) suggests wet sanding the surface with No. 600 paper for aluminum surfaces; however, this is for wind tunnel testing where the absolute drag is the drag number of interest.

In the case of this test, as we care more about the relative drag, the surface finish is of lesser importance. Activity tripping the boundary layer also reduces the impact of surface roughness as it does not determine the transition point.

With these considerations in mind, as well as time restraints, it was chosen to use a combination of machine and hand sanding with P120 and P240 was used, before hand sanding with P300. Variable print height was used to reduce the needed surface sanding while balancing print times, ranging from 0.08 mm to 0.28 mm layer height, depending on the gradient and features. The largest imperfections were seen around holes used for fastening.

It was still important to get similar surface roughness for the interchangeable step sections as deviations here would affect the comparative results, so extra care was taken to sand these a similar amount.

5.4 Experimental Aerodynamics

5.4.1 Internal Flow Errors

A well-designed wind tunnel is able to replicate the airflow experienced in free flight quite well, but there will always be some differences that need to be understood and compensated for.

In free flight, an aircraft experiences what is referred to as external flow, with little to no interference from surrounding objects. The air is free to divert around the object, and the static pressure is the same everywhere. In a wind tunnel, however, the flow is confined by walls, known as internal flow. This causes some differences in the flow, which must be accounted for:

Blockage

When placing a model inside a tunnel section, the model will occupy some of the cross-section, and the area available to the flow will shrink. In a closed tunnel, the air mass flow into the test section will be the same as the flow out. If we assume the flow to be incompressible, the only two variables that may change are speed and area, as seen in equation 5.2. (Barlow, William and Pope 1966)

$$\dot{m} = \rho \cdot V \cdot A = \text{constant} \quad (5.2)$$

In order to keep the errors from this phenomenon small, it is generally recommended to keep the blockage ratio, defined by equation 5.3 to below 5 - 10%. (ibid.) (Airshaper 2020)

$$\text{BlockageRatio} = \frac{\text{ModelFrontalArea}}{\text{TunnelFrontalArea}} \quad (5.3)$$

As mentioned in chapter 5.3.2, the model was originally sized to have a blockage ratio of 7.5%. With the swap to the larger wind tunnel, the blockage ratio was reduced to 0.8%. This increased the local airflow speed from 16 m/s to 16.13 m/s.

Wall interference

Wall interference is the effect the wall has on the flow lines and vortexes generated by the model. In general, we want the model to be far enough from the wall to avoid the wall interfering. In aircraft testing, this is especially applicable to wing tip vortexes. (Airshaper 2020) The phenomena can be seen in Figure 5.6.

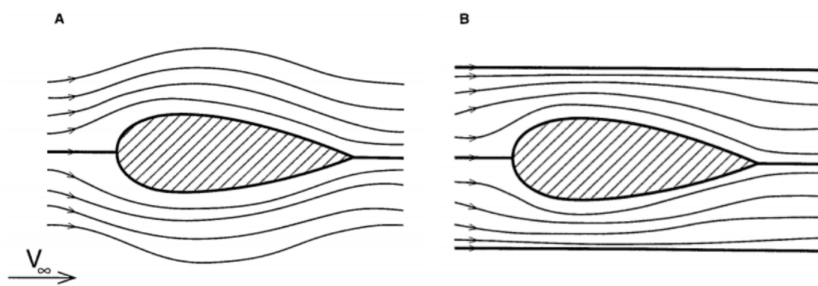


Figure 5.6: Flow over a body in external and internal flow. Figure Borrowed from: Katz (1995)

This was the original reason for orienting the model sideways when the smaller wind tunnel was planned to be used. This wind tunnel only had a height of 500 mm. Since the model was taller than wide, orienting it on the side would increase the wall clearance from 125 mm to 162.5 mm. With the larger wind tunnel, this factor was considered insignificant.

Static Buoyancy

As the flow in a wind tunnel is internal flow, there will be a pressure drop along the length of the flow, as seen at the top of Figure 5.7. This pressure drop will create a static buoyancy force in the horizontal direction if not accounted for, especially for longer bodies like the model in this test. Therefore, some wind tunnels, including the large wind tunnel at NTNU, have an expanding cross-section along the length of the flow. Due to Bernoulli's law, this causes a pressure increase along the flow length, counteracting the pressure drop due to wall interference. (Leishman 2024c)

Boundary layer Growth

As explained in Chapter 5.2, the nozzle right in front of the test section also removes most of the built-up boundary layer. Throughout the test section, the boundary layer will build back up.

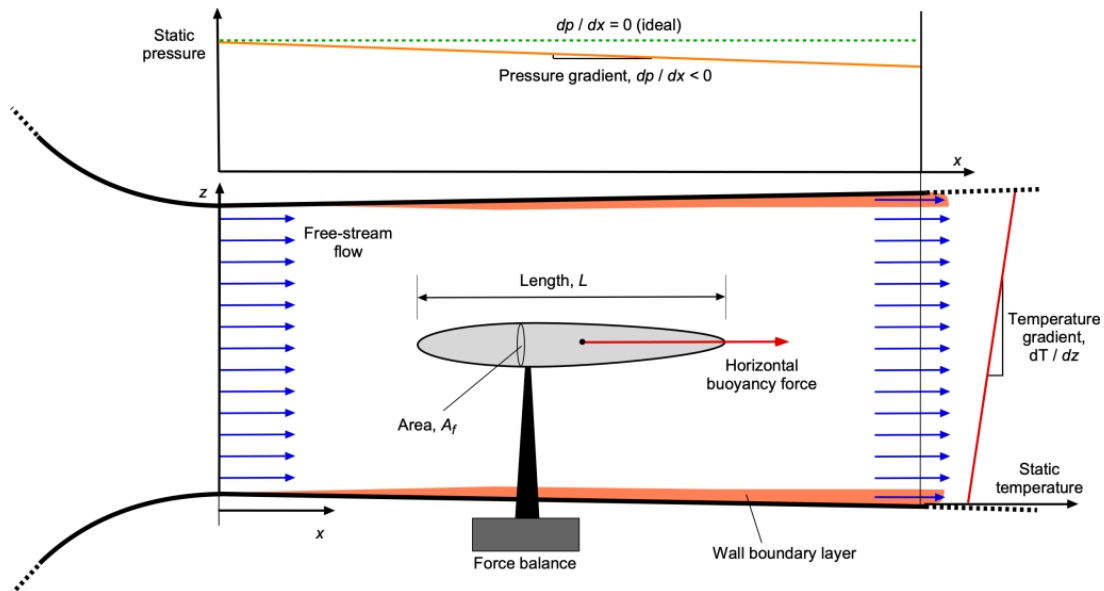


Figure 5.7: Flow through a wind tunnel, wind development of boundary layer, and pressure gradient along the length of the test section. Figure borrowed from Leishman (2024c)

This can be seen in Figure 5.7, and reduces the effective flow area. This can also be counteracted by a gradual increase in cross-section. This is done in the NTNU wind tunnel, as seen in Figure 5.9.

5.5 Other Aerodynamic Dissimilarities

Air density The local air density will matter as this is one of the inputs to, among others, the Reynolds number and drag coefficient. This was adjusted for by measuring the air pressure on the day of testing and comparing it to the standard atmospheric conditions at cruise altitude. On the day of testing, the atmospheric pressure was measured to 733 mmHg (97.7 kPa), using an analog mercury barometer. Air density was calculated using equation 5.4, with the help of a calculator by Czernia and Szyk (2024). Recorded air pressure and temperatures were used. A value for relative humidity of 50% was used as this was not measured.

$$\rho = \left(\frac{p_d}{R_d \cdot T} \right) + \left(\frac{p_v}{R_v \cdot T} \right) \quad (5.4)$$

This gave an air density of 1.12 kg/m^3 . For comparison, at the intended cruise altitude of 1219 m, at 15°C , air density is expected to be 1.058 kg/m^3 . These values are used when comparing the Reynolds numbers.

Incompressible and compressible flow

Air is generally considered incompressible below a speed of Mach 0.32, as this is the threshold where compressibility exceeds 5%. This is about twice the cruise speed of the TAC1. However, the local flow may accelerate as it passes around the body and airfoil, causing the Mach number to be higher locally. As seen in figure 5.8, the relationship between compressibility and Mach number is not linear, and at speed above the TAC1 cruise speed, the effect increases quite significantly. The formula for calculating the compressibility of air can be seen in equation 5.5. (Leishman 2024c)

$$\frac{\rho}{\rho_0} = \left(1 + \frac{\gamma - 1}{2} \cdot M^2\right)^{\frac{-1}{\gamma-1}} \quad (5.5)$$

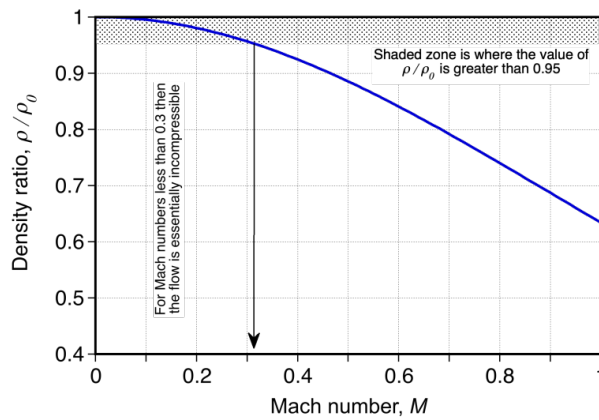


Figure 5.8: Compressibility ratio VS. Mach number. Figure borrowed from Leishman (2024c)

At a speed of 51m/s, like that of the full-scale TAC1 aircraft, compressibility is only 1.1%, and likely higher in certain regions. At the air speeds in the wind tunnel, the air will have a compressibility of less than 0.1%. This error was not accounted for as the change in density is highly localized and cannot be easily applied as a correction factor. It will be a source of error, although small.

5.5.1 Boundary Layer Tripping

As discussed in section 3.1.2, the transition point between laminar and turbulent flow will vary with the Reynolds number, and as the turbulent flow has higher drag than laminar and is more resistant to flow separation, the point of transition will affect the measured values. When testing in a wind tunnel at a lower Reynolds number than in real life, the transition will, therefore, occur at a different point. To account for this, we can add an irregularity in the flow path in order to force the air to become turbulent. This is called tripping the boundary layer. The height of the

trip strip should be high enough to ensure boundary layer tripping but not so high as to cause separation or significant pressure drag. Barlow, William and Pope (1966) suggests placing the trip strip where the diameter of the fuselage is half that of the maximum diameter. The paper also shows a method of choosing the trip height by gradually varying it and observing at what height the C_D stabilizes. This was not done as the absolute drag was not the primary number of interest, and a small increase in read drag was due to using a too-high trip strip being used.

Wind tunnel tests conducted at the NASA Langley Research Center by Ribere, Naeseth, Lowry, and Yates all used transition strips in order to force transition to turbulent flow at a specific point. A strip 12.7 mm wide, with 0.2 mm diameter particles was used to trip the boundary layer at the desired position (5% of the hull length from the bow) The wind tunnel tests were also corrected for blockage and buoyancy forces caused by the tunnel static pressure gradient. Angles of attack were corrected for bending in structural members. (Riebe and Naeseth 1947b) (Riebe and Lowry 1948) (Riebe and Yates 1947).

For this wind tunnel test, a 10 mm strip of No. 80 sandpaper was added at 85 mm from the front of the model. The particle size is equivalent to what was used by the wind tunnel tests mentioned, but the height of the paper was also included. This position is in the middle between the two sources stated above. It is also at the position where the windshield starts, a feature thought to trip the boundary layer at this position in the full-scale aircraft regardless. This trip strip can be seen if Figure 5.9

5.5.2 Summary Wind Tunnel Corrections

Summary of corrections applied and error not accounted for:

- Reynolds number = $1.43 \cdot 10^6$ (3.0% of full aircraft Re)
- Blockage factor = 0.81% corrected for
- Static buoyancy and boundary layer growth = accounted for by tunnel geometry
- Force measurement accuracy = 0.22% of force range expected by steps
- Air speed measurement accuracy = $\pm 0.073\%$ of FS
- Air density and temperature = measured and corrected for
- Compressibility = error in air density estimated to be about 1.1%
- Boundary layer tripping = Tripped with No. 80 paper at 85 mm from the bow

This error buildup reflects the assumptions and calculations made prior to the testing.

5.6 Integration Into Wind Tunnel

The model was originally designed to be mounted on its side in order to give better clearance to the wall and reduce wall interference, as the model is higher than its width, while the smaller wind tunnel was wider than tall. When moving to the larger wind tunnel, it was decided to keep this orientation due to the rotation floor, which would allow for accurate and fast changes in the angle of attacks. This comes with the trade-off that flow visualization will be harder, as one does not see the flow in a side-view against the high-contrast black wall.

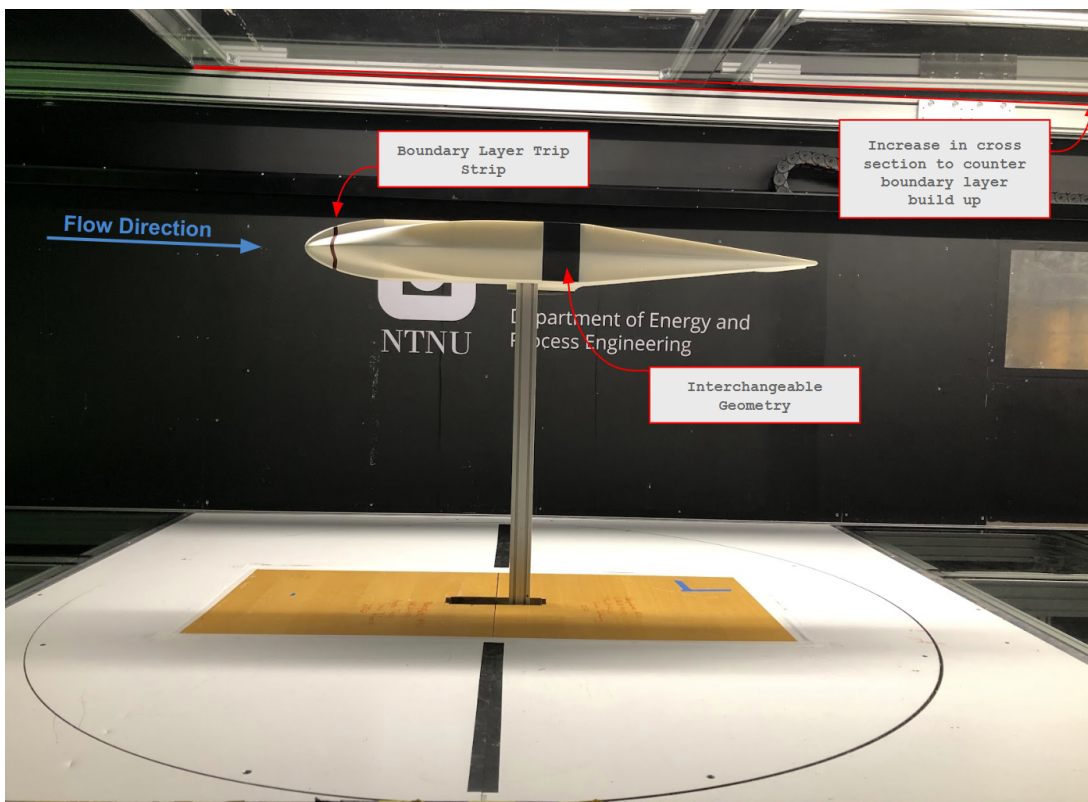


Figure 5.9: Scale model in the wind tunnel

The model was mounted using a 30mm x 60 mm aluminum flex beam. The model had a 30 x 60 mm hole in the side, and bolts were used to fasten the model from the top of the model into two threaded holes in the beam. The bolts were designed to be sunk into the model, and the holes were taped over to reduce interference.

5.7 Missing Data Points

The data series for the geometry with no fairing only had measurements for 2° , 4° , and 6° . This was due to this being the intended sweep. However, after testing this geometry, it was chosen to expand the sweep to 0° to 5° , at 1° intervals due to how fast-changing angles turned out to be.

Some data points were also discovered to be missing due to human error. These data points were:

- 1% depth of step, 10 x length of depth of step fairing, Angle of Incidence at 3°
- Fully faired, Angle of Incidence at 5°

5.8 Results

The results from the wind tunnel test were inconclusive. Most of the results were as expected, like in Figure 5.10a, where the longer the fairing, the lower the drag. But some results, notably from the tests with 1% depth of step, did not follow this trend. As seen in Figure 5.10b, the results are reversed from what one would expect. This holds true even if you apply all the corrections discussed earlier.

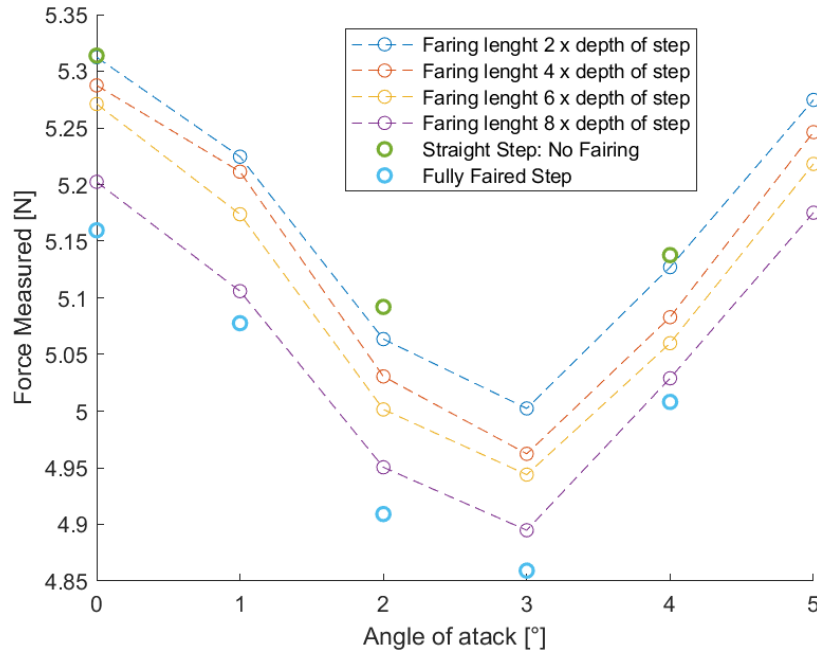
5.8.1 Flow Visualization

Flow visualization with a smoke wand was used to visualize the flow for two different geometries and can be seen in Figure 5.11. A clear difference between the faired and unfaired steps can be seen. The flow separation region is much larger with the unfaired step. The flow in the faired step also does not seem to re-attach until the angle flattens back after the fairing.

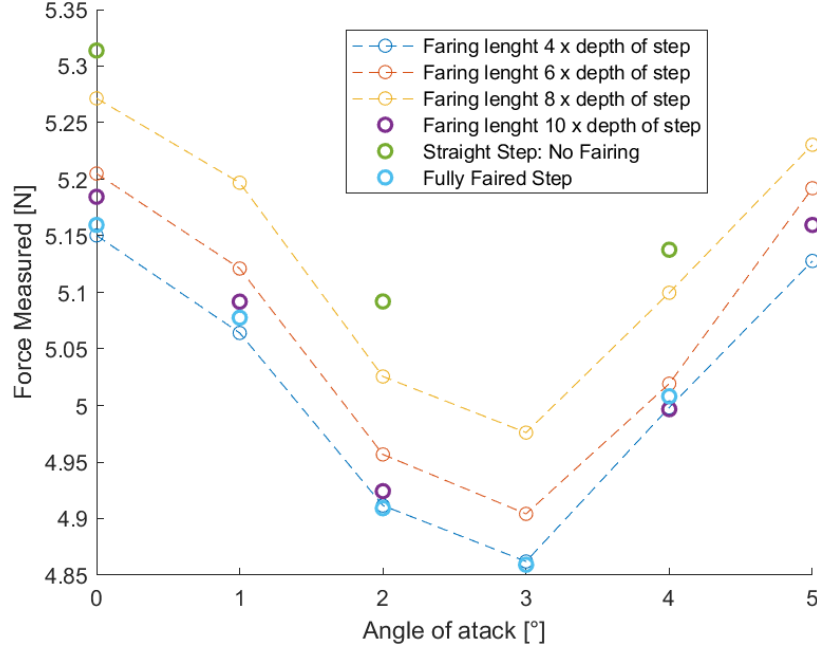
5.9 Post Test Error Analysis

Since only a few data points were off and most aligned with the expected theory, it would be tempting to disregard them and declare the results valid. However, if one assumes that the underlying results are still there but with a large amount of random noise on top, this is exactly what one would expect to get. Most results would be correct, but some, seemingly random, would not be.

The main theory for the inclusive results is the lack of fairing of the mounting strut. The original plan was to add a 3D printed fairing to the strut, but this was prioritized printed last and dropped when the tail angle geometry failed three times in the printer. The lack of fairing may have caused two problems in the readings. Figure 6.13 shows the flow around the strut, and how it creates separation. This simulation is a RANS simulation that would not capture vortexes.



(a) Force measured for the fairings with depth of step 0



(b) Force measured for the fairings with depth of step 1%

Firstly, a large amount of noise can be seen in the measured signal, as seen in Figure 5.12. The noise far exceeds the expected measured drag change due to the change in geometry. This could be an issue related to the flow or measuring, but it is thought to be more likely related to flow separation around the strut used to mount the model. Blunt objects can cause vortex shedding, as seen in Figure 5.13. It should be noted that vortex shedding is typically percent in Reynolds numbers from 1 to 10^3 , while the Reynolds number in the wind tunnel over the mounting strut is about $6 \cdot 10^4$. (Ansys 2020a)



(a) No fairing on the step, step depth 5.8% of beam width



(b) Depth of step 1%. Length of fairing 6 times the depth of step.

Figure 5.11: Smoke visualization of flow separation. Wind speed: 5m/s

This error could have been avoided by checking the drag expected from the strut and comparing it to the The strut had a frontal area of about 67% of the fuselage, but as seen in Figure 3.5, the drag coefficient can vary by more than an order of magnitude depending on the shape. While a rectangular shape can have a drag coefficient based on frontal area around 2, fairing it could bring it down to less than a tenth of that. This would have made the drag from the strut about equal to the fuselage, not an order of magnitude larger.

Another thing that could have caught this error is doing a CFD run on the test set-up. This is a common thing to do for wind tunnel testing, as it allows, among other things, to check for interference between vortices and the walls. However, as the plan up until the day before the testing was to fair the strut, the CFD would probably have been run with a fairing, not catching the error.

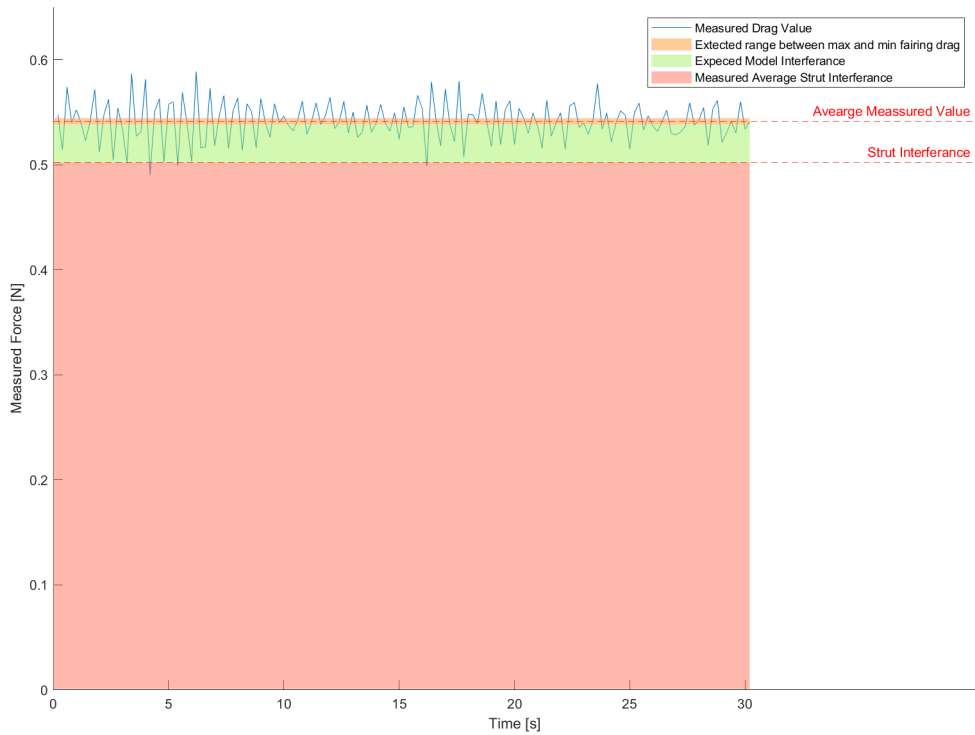


Figure 5.12: Measurement made in the wind tunnel showing the size of fluctuations over a 30-second period.



Figure 5.13: Vortex shedding of a cube. Image borrowed from: Stern and yang (2012)

The second error was not recording the air speeds measured during the runs. The air speeds were measured as a pressure differential and converted to speeds with a MATLAB script created by the NTNU lab. These were observed to be $16 \pm 0.05 m/s$ for all the runs, and this was thought to be accurate enough that it would not need to be adjusted for. If converting to expected force variation, this would only mean a variation of $\pm 0.6\%$ of the force on the model. The error made was to not account for the fact that this error would also affect the strut, and as the strut had a drag about ten times that of the model, the variation in drag force measured due to a change in airspeed by only $\pm 0.05 m/s$ would actually cause an error up to $\pm 6\%$, not $\pm 0.6\%$. Errors related to the reading of airspeed, discussed in Chapter 5.2.1, would add to this error, also with a multiplier factor of 10.

The error estimation was also somewhat made complicated by not having access to the data

sheets for the equipment in the wind tunnel. A secondary source, a master thesis from 2021 utilizing the same tunnel, was used for the source of information on the wind tunnel accuracy. Due to this, an error buildup analysis of the wind speed accuracy was not possible. A number on the accuracy of 0.073% of full scale reading was found, but not what the full scale reading of the equipment was.

The accuracy of the wind tunnel force balance was found in the thesis, but it was not clear if this was the absolute accuracy, repeatability, or the resolution. Due to the measurement being zeroed between each run, absolute accuracy and repeatability would in effect be the same for this setup.

6 CFD Study of Step Geometry

Due to the inconclusive wind tunnel results, it was decided to do a limited study in CFD to obtain the results not obtained in the wind tunnel. Although the wind tunnel test did not show the drag difference of step fairings as desired, it could still be used as a validation case to validate the CFD setup.

SimScale was used to run the CFD, using an academic thesis license provided by the SimScale team. SimScale provides an interface that integrates meshing, simulation set-up, and post-preprocessing in one platform. SimScale utilizes open-source solvers from Open-foam in the background. The service also comes with cloud computing, allowing the simulations to be set up and run without the need for expensive computing hardware.

CFD is a very complex topic that requires years to fully understand. In this thesis, the following factors were considered when setting up the mesh and simulation:

Factors considered and goals set

- $k - \omega$ SST chosen as RANS model
- Y^+ target of 1 with full resolving of the boundary layer, between 0.7 - 1.5 reached.
- Inflation layer growth rate of 1.47
- Mesh resolution study conducted
- Convergence of total force in X direction used as measure of convergence

For most other values, default or values recommended by SimScale (2024b) were used.

6.1 Choice of CFD Model

CFD (Computational Fluid Dynamics) is a method to estimate the airflow. The key word is estimate, and no CFD solver will be perfect. There are three main categories of CFD solvers, seen in Figure 6.1. DNS is the most computationally resource intensive, while RANS, is the least resource intensive. (LEAP 2018)

An example of a downside of using a RANS model is that if we wanted to check if the strut used in the wind tunnel modeling caused vibrations due to large eddies forming, the RANS would not capture this.

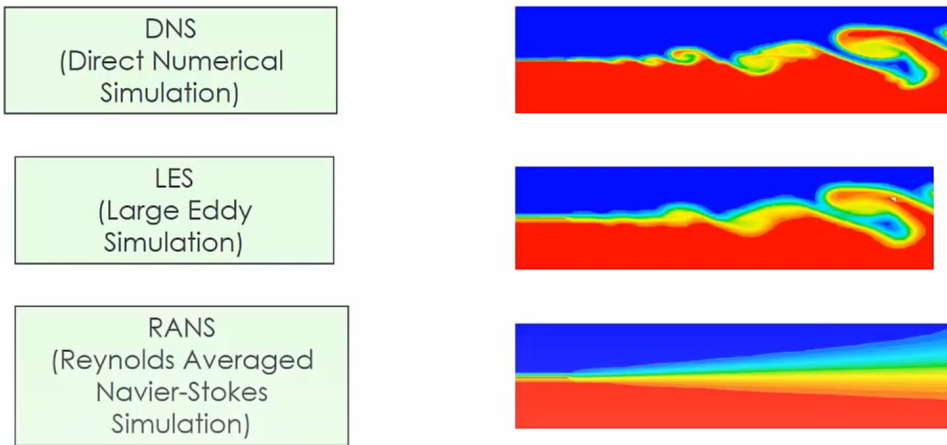


Figure 6.1: Difference between solvers methods. Image Borrowed from: LEAP (2018)

In this thesis, RANS will be used due to the computational power available and the accuracy required.

6.1.1 RANS turbulence model

Many RANS turbulence models exist, but the most popular are the following:

Spalart-Allmaras is a one equation model. Has some limitations in modeling separated flows.

k-epsilon is a popular two-equation turbulence model, with one equation for turbulent kinetic energy and $k - \epsilon$ one for turbulent energy dissipation. The model does not always solve boundary layer flow with adverse pressure gradients well.

k-omega is another two-equation turbulence model that is known to better model the boundary layer.

k-omega SST uses $k - \omega$ for near-wall boundary wall prediction and the $k - \epsilon$ in the free stream, combining the strengths of these two models. It is known to give a good prediction of flow separation.

6.1.2 Choosing a RANS Turbulence Model

Versteef and Malalasekera (2007) recommends the Spalart-Allmaras, $k-\omega$ or $k-\omega$ SST turbulence model for external aerodynamics. The $k - \omega$ is stated to perform best over a backwards-facing step.

Sazak (2017) did a CFD study comparing $k - \epsilon$, Spalart-Allmaras, and $k - \omega$ SST, specifically for seaplane floats, up against validation data from a NACA wind tunnel test. In this test, the

$k - \omega$ SST came out with the best results, with an error of about 10% of the wind tunnel test.

An example validation case run by SimScale for a body with a backwards-facing step also used the $k - \omega$ SST model. (SimScale 2024a)

Based on these considerations, it was chosen to use the $k - \omega$ SST turbulence model.

6.2 CAD Model Preparation and Import

A guideline from SimScale on how to import and set up the boundary conditions was used. (SimScale 2024b)

The simulation was run with a symmetry plane down the symmetric axes of the aircraft in order to reduce the computational cost. The remaining three walls were set up with slip condition, while the inlet was set as velocity inlet and the outlet as pressure outlet.

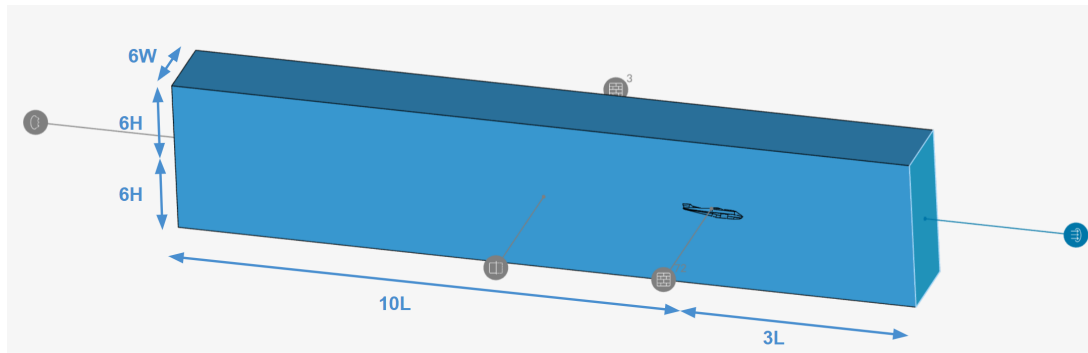


Figure 6.2: Flow volume set up as a function of the model size

6.3 Meshing

6.3.1 Inflation Layers

Modeling the flow behavior in the boundary layer, and especially the skin friction forces that come from it, is important to get accurate CFD results. There are two primary methods of achieving this, either through very thin inflation layers that contain the boundary layer or through not modeling the boundary layer but having the CFD solver use correction factors known as wall functions. (Ansys 2020b)

Figure 6.3 shows the breakdown of a boundary layer. We either want the first inflation height to be within the thinnest laminar sub-layer or cover the entire boundary layer with one cell. The reason for this can be seen in the right part of Figure 6.3. CFD solvers linearly interpolate

between nodes, and if there are mesh layers in the boundary layer, the linear interpolation will create an offset.

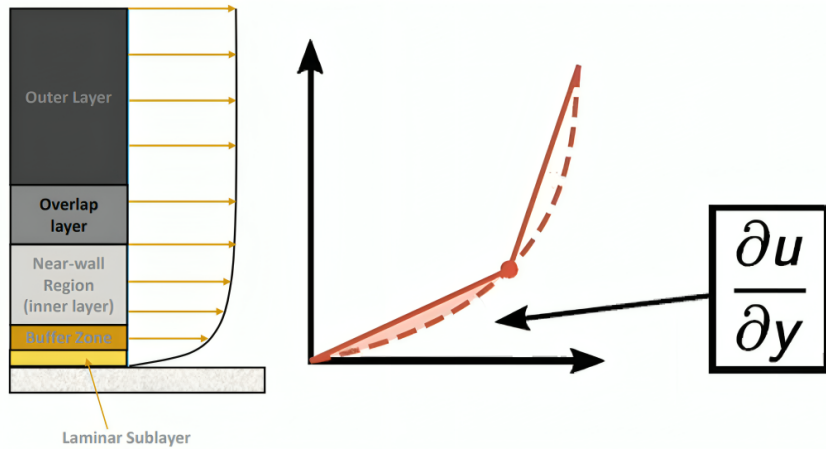


Figure 6.3: Example of buildup of a turbulent boundary layer, and linear interpolation error. Image edited based on original images from Ansys (2020b) and Wimshurst (2022)

A unitless value, known as Y^+ , is used in order to describe how far into the boundary layer the first cell height reaches.

If we are using wall functions, we generally want Y^+ to be larger than 350. If we are resolving the boundary layer, we want a Y^+ less than 5. A goal for Y^+ of 1 is commonly used. (Ansys 2020b)

As wall functions do not predict flow separation well, we will aim for a low Y^+ value in this study. (Wimshurst 2022)

We also want to make sure the boundary layer is contained within the inflation layers, as seen in Figure 6.4.



Figure 6.4: Inflation layers should be contained within the inflation layers, as seen in the right image, in order to resolve the boundary layer properly. Image borrowed from Wimshurst (2021a)

A third factor to keep in mind is the layer growth. The cell volume growth within the inflation layers should preferably not exceed 1.3. The difference in volume from one cell to another should not be too large. This is particularly important in the transition from the inflation layers to the

main mesh, as seen in Figure 6.5.

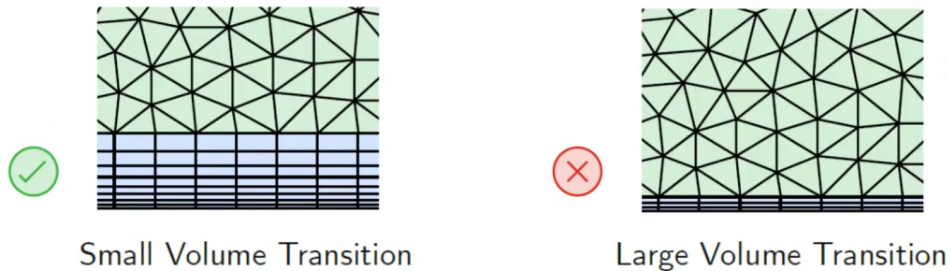


Figure 6.5: Example image of good and poor volume transition between inflation layer. Image borrowed from Wimshurst (2021a)

Based on these considerations, a tool by Wimshurst (2021b) was used to estimate inflation layers parameters. This tool inputs values for velocity, characteristic length, viscosity, density, targeted Y^+ , and a number of inflation layers. The output is first layer height, final layer height, boundary layer thickness, and growth ratio.

The values used in this study can be seen in Figure 6.6.

The growth rate had to be higher than the recommended 1.3 as this would have required 28 layers, and the SimScale solver only permits 20 layers.

This only gives a first estimate to choose inflation layer parameters. The actual Y^+ will be calculated by the CFD solver when it runs, and one might have to iteratively change the inflation layer parameters to get the desired Y^+ value.

Velocity (m/s)	Length Scale (m)
51	7.2
Viscosity (Pa s)	Density (kg/m ³)
0.00001876	1.057
Target y^+ (-)	Layers (-)
1	20
Calculate	
First Layer (m)	Final Layer (m)
2.04e-5	3.00e-2
δ_{99} (m)	Max. Growth Ratio (-)
9.42e-2	1.47

Figure 6.6: Input and output values used for determining the inflation layer in the mesh

6.3.2 Mesh Resolution

Mesh resolution is another important factor in CFD accuracy. It is good practice to do a mesh independence study, where one gradually varies the mesh resolution and observes the changes in output.

As a baseline for this study, we can look at two mesh independence studies done by SimScale (2024a) and Sazak (2017), both for similar shapes and with wind tunnel data for comparison. Both studies used $k - \omega$ SST.

The mesh study done by Sazak (ibid.) decreased the deviation to the wind tunnel data from 18% to 9% by increasing the mesh from 2.74 million to 10.44 million. In the end, the C_D had more or less stabilized. This was for a seaplane float.

The mesh study done by SimScale (2024a) decreased the deviation to the wind tunnel data from 17% to 6% by increasing the mesh from 3.8 million to 23.8 million. Here, the mesh had not stabilized at 10 million cells but stabilized when it increased to 23.8 million. This shape was a blunt body with a sharp break at the rear to cause flow separation.

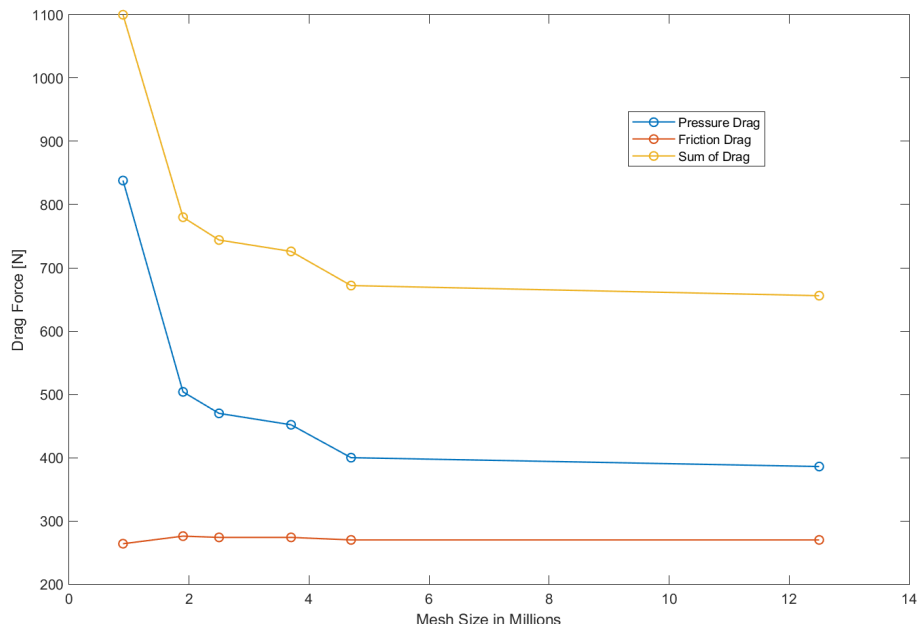


Figure 6.7: Mesh independence study performed on the TAC1 hull

Figure 6.7 shows the mesh independence study performed. The results stabilized after 4.7 million cells. Although the 12M cell mesh might give more accurate results, the difference Vs the extra required computational power, was not considered a good trade-off.

The rest of the study was therefore conducted with the 4.7 million cell count mesh. No mesh

qualities were changed between runs from this point.

6.3.3 Refinement Regions

In order to get the most out of the mesh cell count, refinement regions are used to increase the mesh count where it is needed the most. Three volumetric regions, two containing the entire aircraft and one around the step region, were used, as seen in Figure 6.8.

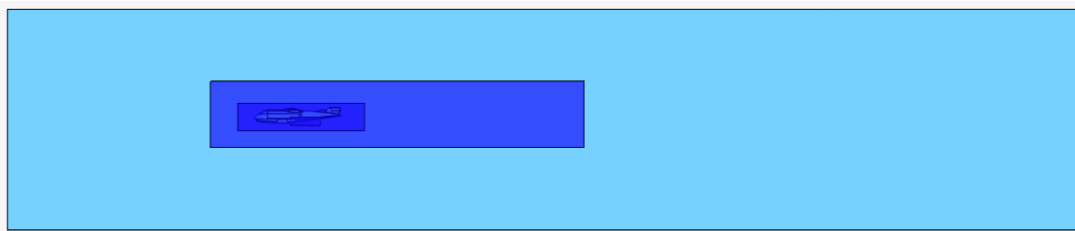


Figure 6.8: Refinement regions used for this CFD study. A third volume was used around the step region but is not that visible in the image.

In addition, a surface refinement was used in order to increase the mesh's detail around the curves on the model.

Figure 6.9 and C.1 shows the final mesh with 4.7 million cell count. Figure C.3 shows the Y^+ for the run without step fairing.

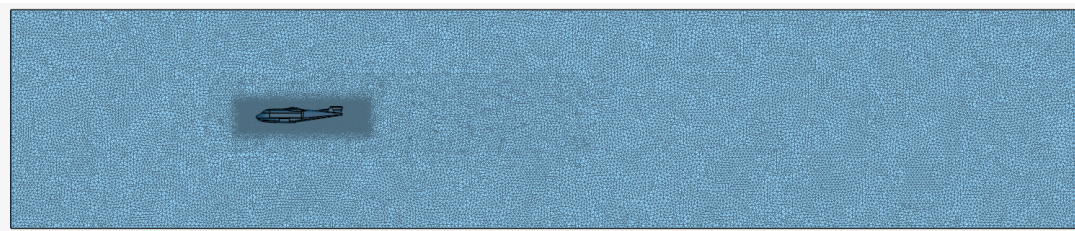


Figure 6.9: Mesh used in the CFD study comparing steps

6.4 Runs

The following geometries were run in the CFD study:

- 0% depth of step, with straight fairings lengths from 2 to 8 x the depth of step
- 1% depth of step, with straight fairings lengths from 4 to 10 x the depth of step
- 2% and 3% depth of step, with straight fairings lengths of 6 x the depth of step
- Geometry with no fairing
- Geometry with baseline concave fairing

No angle of attack sweeps were conducted.

The second concave fairing and the fully faired fairing were omitted due to time constraints.

6.5 Results

The results from the CFD study can be seen in Figure 6.10. The results are expressed as the drag force reduction, with the non-faired 5.8% depth of step as a baseline.

Two series, one for the 1% depth of step and the other for 2% depth of step, is plotted. The rest of the results are plotted as single data points. The concave fairing did not fit onto the x-axis and is instead plotted as a dashed horizontal line.

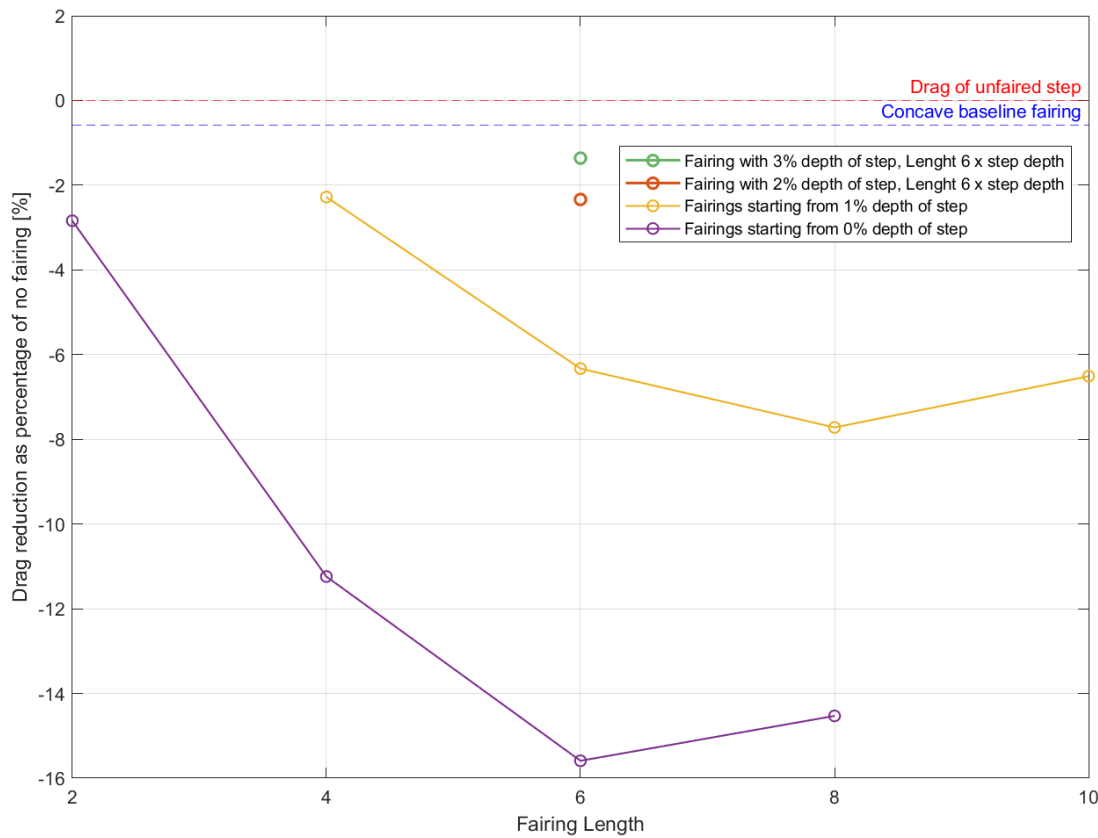


Figure 6.10: Results from CFD step study. The drag of the fairings is given as a percentage decrease compared to the non-faired step with a depth of 5.8%. The x-axis is the length of the fairing for that run

For all the data points, the skin friction was more or less constant, around 270 to 273 Newton.

The main source of difference was the pressure drag.

6.6 Discussion on the Accuracy and Confidence in the Results

Two data points do not follow the trend of what was expected, as do the last two points of the two series. For these points, the drag increases with longer fairing.

For the data point on the 0% depth of step series, this might be due to errors with the previous

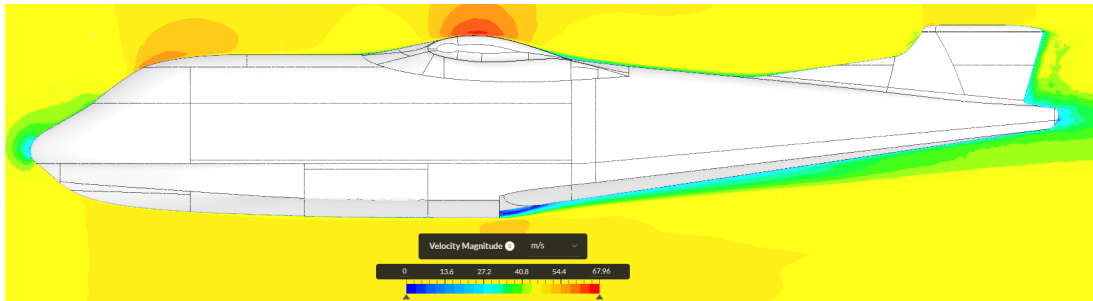


Figure 6.11: Flow field around aircraft showing flow separation behind the step without fairing

data point (0% depth of step, length of fairing 6). This run failed to converge twice, and the mesh was, therefore, slightly tweaked. For the last data point on the 1% depth of step, no good explanation was found for why the drag increased.

This unexplained increased increase decreases the confidence in the data, as there might be an error in the simulation set-up.

6.6.1 Flow Separation Comparison

The flow separation behind the un-faired step, seen in Figure 6.11, was very similar to the flow separation seen in the wind tunnel, seen in Figure 5.11a, both in length and height. This is a good sign that the simulation might treat the separation correct. It should be noted that the flow visualization in the wind tunnel was done at only 5 m/s while this CFD run is at 51 m/s, so not too much emphasis should be put on this.

6.6.2 Convergence

Looking at the convergence of the force data, it was clear that the simulations were not fully converging in the 1000 iterations it were running. One simulation run was set to 3000 iterations to see how far from convergence the runs were.

As seen in Figure 6.12, the results did not converge until after about 3000 iterations. Running all the runs at this length would have tripled the run time and computational power required, and would not have been feasible with the core hours allocated, without reducing mesh size.

Instead, it was checked that each run got to about the same gradient of convergence. It was then thought that the remaining convergence would affect all runs similarly, and that the results as a percentage of each other would be similar. This was checked for one fairing, the 1% depth of step, 6 times the length fairing, running both that fairing and the non faired step to 3000

iterations. The difference in percentage at 1000 iterations was 6.3% and after 3000 attentions, 7.1%. This should therefore not significantly change the comparative results.

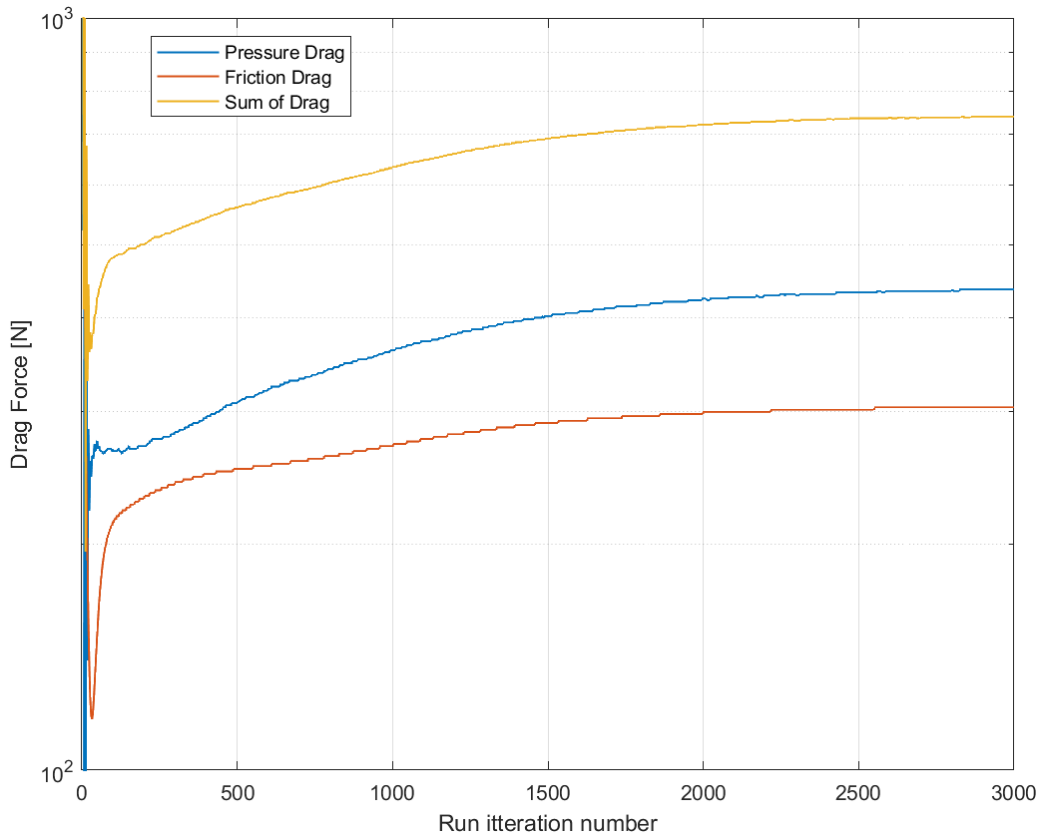


Figure 6.12: Convergence of a CFD run, over 3000 iterations

If the absolute number on the drag is to be used, a correction factor should be applied to the CFD results. The converged results after 3000 iterations were 17.1% higher than the results after 1000 iterations.

6.6.3 Validation Case: Compare to Wind Tunnel Data

The same test set-up, as in the wind tunnel, was also run in the CFD. The CFD estimated 5.2N for the mounting strut and 1.2N for the model under the same conditions as in the wind tunnel. This is 19% higher than what was measured in the wind tunnel.

The mesh was not very refined, and the mounting strut had some differences, like missing fillets on the corner in the CFD. With this in mind, 19% accuracy is within what could be expected. As seen earlier in this chapter, errors in other wind tunnel testings were in the range of 17% to 7%, compared to wind tunnel data.

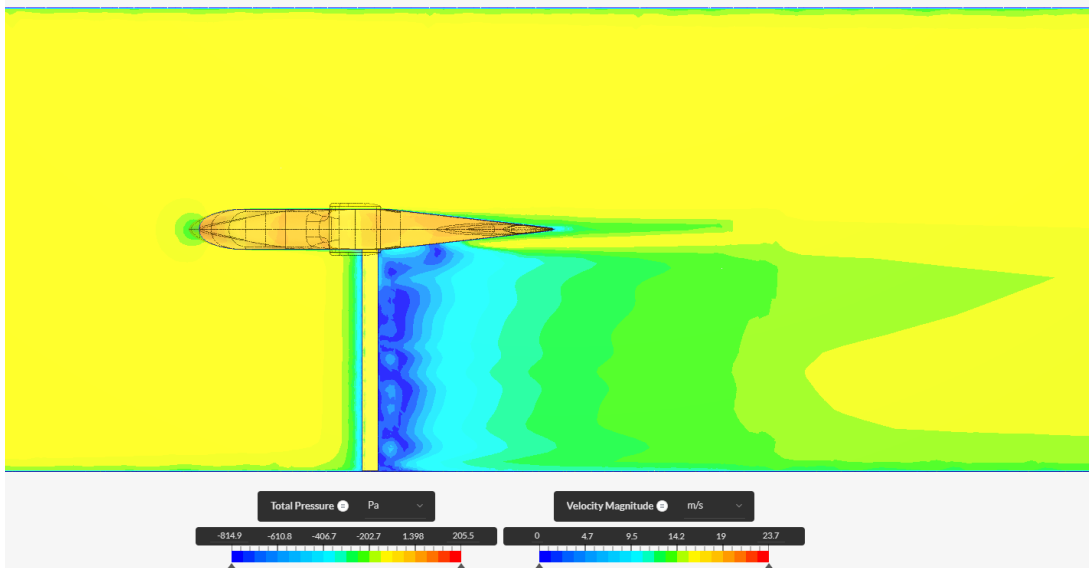


Figure 6.13: Flow field of flow in the wind tunnel, simulated by CFD. The interference from the mounting strut can be clearly seen. The surface of the model is plotted with a pressure field in [Pa], while the surrounding field is plotted with velocity [m/S]. Model seen from top view

6.6.4 Comparing Results to Expected Values Based on Theory

The overall test aligned well with what was expected from the theory. The same non-linear trend shown by Coombes and Clark (1937) is seen. The fairings not starting from 0% depth of step are also seen to be a lot less effective, similar to what was shown by Coombes and Clark (*ibid.*).

The effect of fairing the step at 2% and 3% starting depth was smaller than what was expected.

7 Conclusion

The objective of the thesis was to investigate the potential for reducing the aerodynamic drag of a flying boat hull. From the literature study and tests done, the following conclusions can be drawn:

Summary of conclusions

- The minimum drag of a flying boat can be expected at a positive angle of incidence
- Step fairings can be effective in reducing the drag by up to 15% of hull drag
- Step with a start depth of step can only be expected to provide a maximum of half the drag reduction achievable with a fairing starting at 0% depth of the step
- Features like afterbody angle, deadrise warp, step ventilation, and auxiliary steps can be a way to reduce the required step or allow for more aggressive fairing

In addition, the thesis work has gathered and sorted an extensive database of more than 50 sources on flying boat hull design that can be used for further development.

The method for testing many step fairings in a short period, by making a small part of the model interchangeable, also proved to be effective and could be implemented also for hydrodynamic testing.

8 Future Work

Due to time constraints, the number of CFD runs was limited. More CFD runs, particularly the angle of incidence and the remaining geometries from the wind tunnel, should be run.

After that, the next step in the development would be to use the results from this thesis in a trade-off against results from hydrodynamic testing.

The steps with a starting depth of step did not significantly reduce drag, and these are thought to be the ones with the most promising hydrodynamic performance. If the hydrodynamic testing proves that these are the only feasible step fairings, a movable step could be considered.

The first step in that development is to determine the criticality of landing with the extended fairing and the loads/suction that acts on the fairing.

References

- Airshaper (2020). "Scale model wind tunnel testing explained". In.
- Ansys (2020a). *Drag Forces in External Flows - Real External Flows – Lesson 2*. <https://innovationspace.ansys.com/courses/wp-content/uploads/sites/5/2020/09/Drag-Force-in-External-Flows-Lesson-2-Handout.pdf>. Accessed: 21.10.2024.
- (2020b). "Turbulent Boundary Layers". In: *Ansys.com*.
- Barlow, William and Pope (1966). *Low speed wind tunnel testing*. John Wiley and Sons Inc.
- Benson and Freihofner (1944). "Landing Characteristics of a model of a flying boat with the depth of step reduced to zero by the means of a retractable flap". In: *NACA, Langley Memorial Aeronautical Laboratory Langley Field, Va.*
- Benson and Havens (1945). "Tank tests of flying boat model equipped with several types of fairings designed to reduce the air drag of the main step". In: *Langley Memorial Aeronautical Laboratory Langley Field, Va.*
- Benson and Lindsay (1943). "The use of retractable planing flap instead of a fixed step on a seaplane". In: *Langley Memorial Aeronautical Laboratory Langley Field, Va.*
- C3S (2024). *Copernicus: 2024 virtually certain to be the warmest year and first year above 1.5°C*.
- Chicken (1999). "Conceptual design methodologies for waterborne and amphibious aircraft". PhD thesis. Cranfield University.
- Conway and Maynard (1943). "Wind-tunnel tests of four full-scale seaplane floats". In: *NACA, Langley Memorial Aeronautical Laboratory Langley Field, Va.*
- Coombes and Clark (1937). "The Air Drag of Hulls: The Effect of Alterations in the Main Dimensions and Various Detail Features". In: *Aircraft Engineering and Aerospace Technology, Vol. 9, Iss 12 pp. 315-328*.
- Czernia and Szyk (2024). *Air Density Calculator*.
- Dawson, Walter and Hay (1946). "Tank Tests to Determine the Effect of Varying Design Parameters of Planning-Tail Hulls". In: *National Advisory Committee for Aeronautics*.
- deCallies (1967). "Hydrodynamics manual". In: *Naval Air Test Center, Patuxent River, Maryland*.
- EASA (2015). *CS23 - Certification Specifications and Acceptable Means of Compliance for Normal, Utility, Aerobatic, and Commuter Category Aeroplanes*.
- FFA (2014). *Seaplane, skiplane, and float/ski equipped helicopter operations handbook*.

- Hamilton (1947). "An investigation into the effect of forced and natural afterbody ventilation on the hydrodynamic characteristics of a small flying boat (Saro 37) with a 1:20 fairing over the main step". In: *Pricipal Director of Research*.
- (1956). "A Full-scale Investigation into the Hydrodynamic Behaviour of a Highly Faired Flying-boat Hull". In: *Aeronautical Research Council Reports and Memoranda*.
- Hartman (1935). "The aerodynamic drag of flying boat models as measured in the N.A.C.A 20-foot wind tunnel". In: *Langley Memorial Aeronautical Laboratory Langley Field, Va.*
- Hoerner (1965). *Fluid-Dynamic Drag*. Published by the Author.
- Hugli and Axt (1951). "Hydrodynamical investigation of a series of hull models suitable for small flying boats and amphibians". In: *Stevens Institute of Technology*.
- Katz (1995). *Race Car Aerodynamics*. Bentley Publishers.
- Klöwer (2021). "Quantifying aviation's contribution to global warming". In: *Environ. Res. Lett.* 16.
- Larsen (2021). "Aerodynamic validation of a Formula Student race car". MA thesis. NTNU.
- LEAP, Australia (2018). "Turbulence Modelling using ANSYS Fluent- Presentation and Demo - ANSYS CFD for FSAE teams - 1/10". In: *youtube.com*.
- Leishman (2024a). "Aerodynamics of Airfoil Sections". In: *Embry-Riddle Aeronautical University*.
- (2024b). *Airplane Equations of Motion*. Accessed: 13.10.2024.
- (2024c). *Introduction to Aerospace Flight Vehicles*. Embry-Riddle Auronotical Univeristy.
- Locke (1946). "An analysis of the skipping characteristics of some full-size flying boats". In: *NACA*.
- Mistral (2024). "Airborne Electronics – Airworthiness Regulations and Safety Requirements". In: <https://www.mistralsolutions.com>.
- NASA (2022a). *Aircraft Rotations*. <https://www1.grc.nasa.gov/beginners-guide-to-aeronautics/aircraft-rotations/>. Accessed: 13.10.2024.
- (2022b). *What is Drag?* <https://www1.grc.nasa.gov/beginners-guide-to-aeronautics/what-is-drag/>. Accessed: 13.10.2024.
- Olson and Land (1942). "The Longitudinal Stability of Flying Boats as Determined by Tests of Models in the NACA Tank I : Methods Used for the Investigation of Longitudinal Stability Characteristics". In: *NACA, Langley Memorial Aeronautical Laboratory Langley Field, Va.*

- Parkinson and Land (1944). "The landing stability of a powered dynamic model of a flying boat with a 30 degree V-Step and with two depths of transverse step". In: *Langley Memorial Aeronautical Laboratory Langley Field, Va.*
- Parkinson, Roland and House (1939). "Hydrodynamic and aerodynamic tests of a family of models of seaplane floats with varying angles of dead rise". In: *National Advisory Committee for Aeronautics.*
- Riebe and Lowry (1948). "Effect of length-beam ratio on aerodynamic characteristics of flying-boat hulls without wing interference". In: *Langley Memorial Aeronautical Laboratory Langley Field, Va.*
- Riebe and Naeseth (1947a). "Aerodynamic Characteristics of three deep stepped planing tail flying boat hulls". In: *NACA, Langley Memorial Aeronautical Laboratory Langley Field, Va.*
- (1947b). "Effect of Aerodynamic Refinement on the Aerodynamic Characteristics of a Flying-boat Hull". In: *Langley Memorial Aeronautical Laboratory Langley Field, Va.*
- Riebe and Yates (1947). "Aerodynamic characteristics of three planing-tail flying-boat hulls." In: *Langley Memorial Aeronautical Laboratory Langley Field, Va.*
- Sazak (2017). "Parametric investigation of hull shaped fuselage for amphibious uav". MA thesis. Middle East Technical University.
- SimScale (2024a). "Aerodynamics: Flow around the Ahmed Body". In: *Simscale.com*.
- (2024b). "Tutorial: Incompressible Flow around a Formula Student Car". In: *SimScale.com*.
- Smith (1957). "Wind-tunnel tests on seaplane hulls in the R.A.E 5-ft Diameter Open Jet Tunnel and the N.P.L Compressed Air Tunnel". In: *Aeronautical Research Council Reports and Memoranda*.
- (1959). "The Full-scale drag of some Flying Boat Seaplanes". In: *Aeronautical Research Council Reports and Memoranda*.
- (2022). *Climbing and Gliding Caveat*. <https://aircraftflightmechanics.com/AircraftPerformance/GlidingFlight.html>. Accessed: 13.10.2024.
- Smith and White (1954). "A Review of Porpoising Instability of Seaplanes". In: *Aeronautical Research Council Reports and Memoranda*.
- Sottorf (1937). "The Design of Floats". In: *Technical Memorandums National Advisory Committee of Aeronautics*.
- (1942). "Systematic model researches on the stability limits of the dvl series of float designs". In: *Deutschen Luftfahrtforschung*.

- Stauffer and Takahashi (2023). “A History and Commentary on Thrust/Drag Bookkeeping”. In: *Arizona State University, Tempe.*
- Stern and yang (2012). “A simple and efficient direct forcing immersed boundary framework for fluid–structure interactions”. In: *Journal of Computational Physics*.
- Talay (1975). *Introduction to the Aerodynamics of Flight*. Nasa.
- Thurston (1978). *Design for Flying*. McGraw-Hill.
- Tomaszewski, Smith and Chalmers (1946). “A Preliminary Examination of Hull Afterbody Ventilation”. In: *Royal Aircraft Establishment*.
- Torenbeek (1982). *Synthesis of Subsonic Airplane Design*. Springer-Science+Business Media, B.V.
- Versteef and Malalasekera (2007). *An Introduction to Computational Fluid Dynamics*. Pearson.
- Wilczek (2021). *Seaplane Design - A Forgotten Art*. Hamburg Aerospace Lecture Series.
- Wimshurst (2021a). “[CFD] Inflation Layers / Prism Layers in CFD”. In: *youtube.com*.
- (2021b). “Inflation Layer Calculator”. In: *fluidmechanics101.com*.
- (2022). “Understanding $y+$ in CFD Part 1/2”. In: *youtube.com*.
- Wolf (2004). “Minimizing the Cooling System Drag for the New Porche 911 Carrera”. In: *Porche AG*.
- Yates and Riebe (1947). “Effect of Length-beam ratio on the aerodynamic characteristics of Flying Boat Hulls”. In: *NACA, Langley Memorial Aeronautical Laboratory Langley Field, Va.*

A Step Geometries for Wind Tunnel Testing

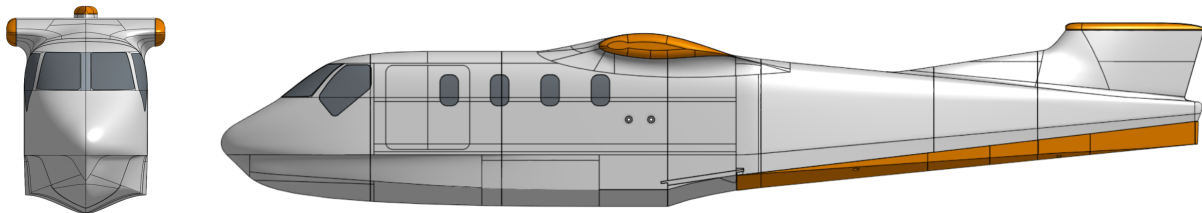
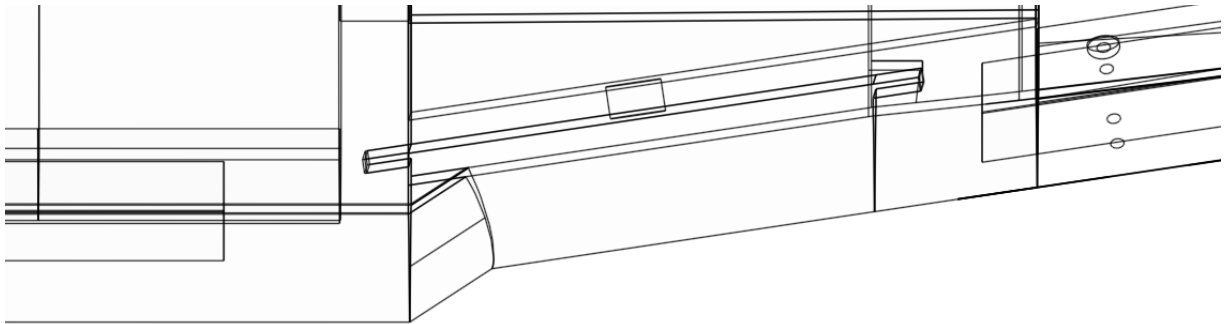
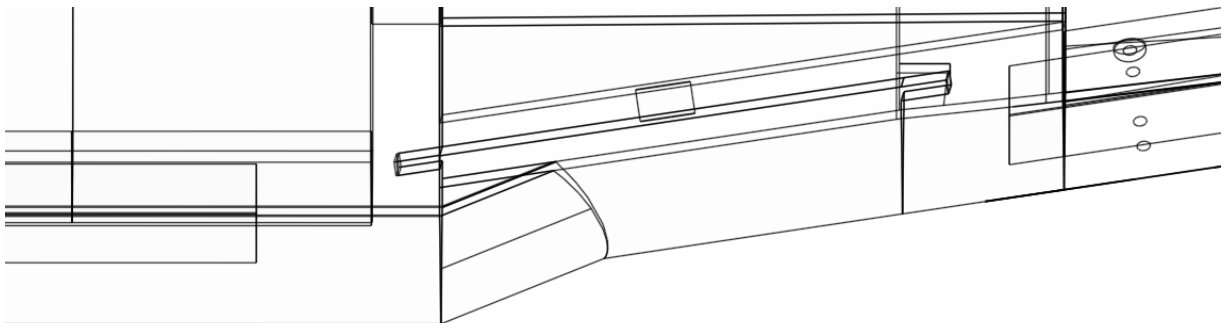


Figure A.1: Frontal and side view of model used in the wind tunnel testing, including wing and tail fairings, and tail attachment to change afterbody angle

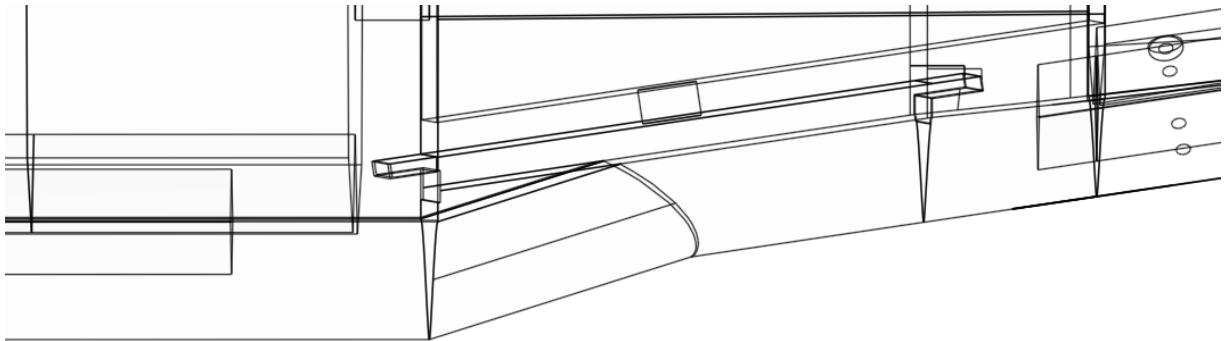
Depth of step 0%, Length of fairing 2 x depth of step:



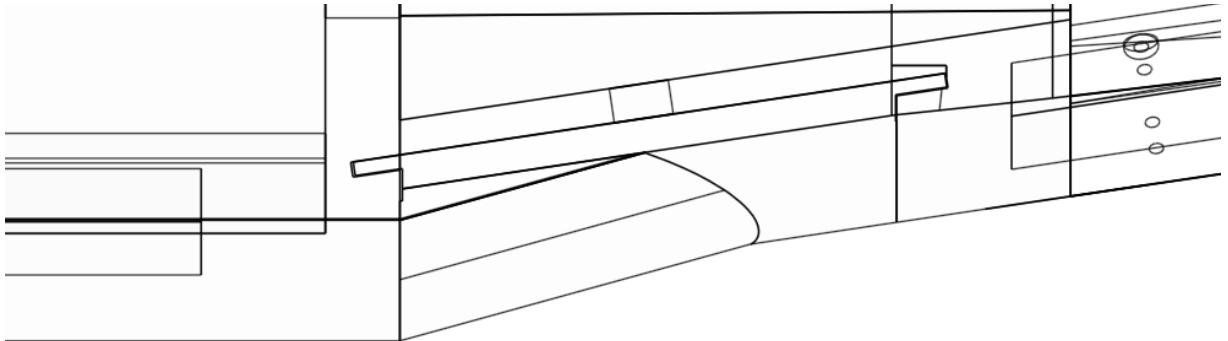
Depth of step 0%, Length of fairing 4 x depth of step:



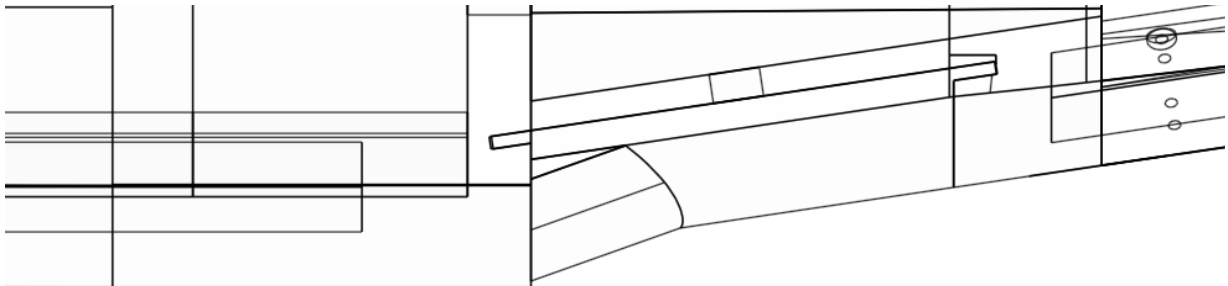
Depth of step 0%, Length of fairing 6 x depth of step:



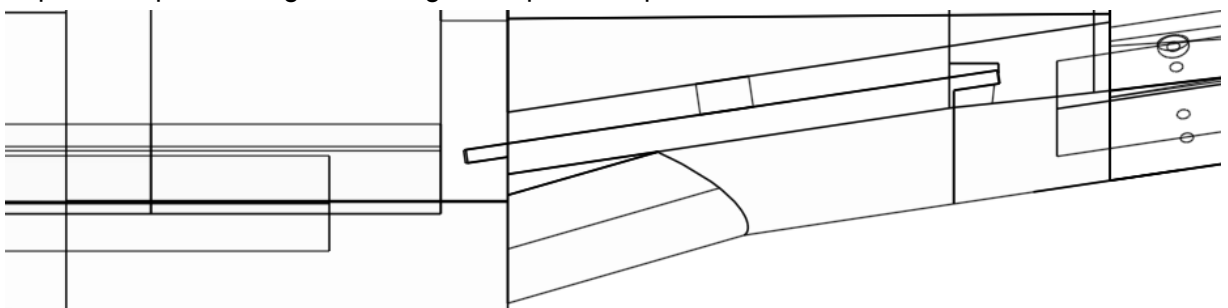
Depth of step 0%, Length of fairing 6 x depth of step:



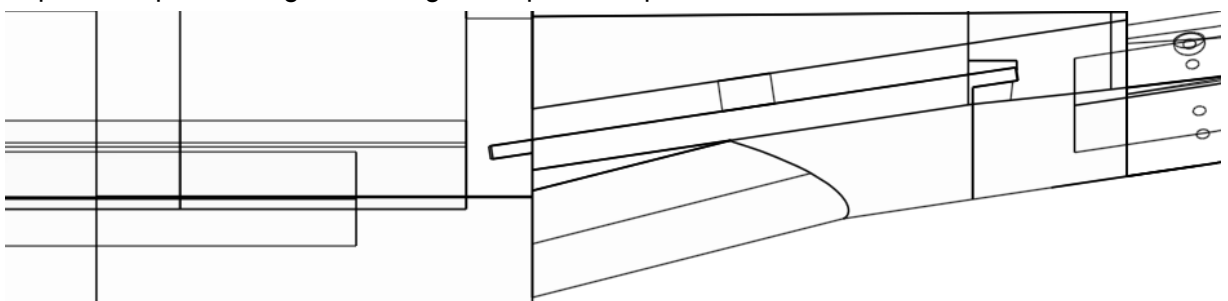
Depth of step 1%, Length of fairing 4 x depth of step:



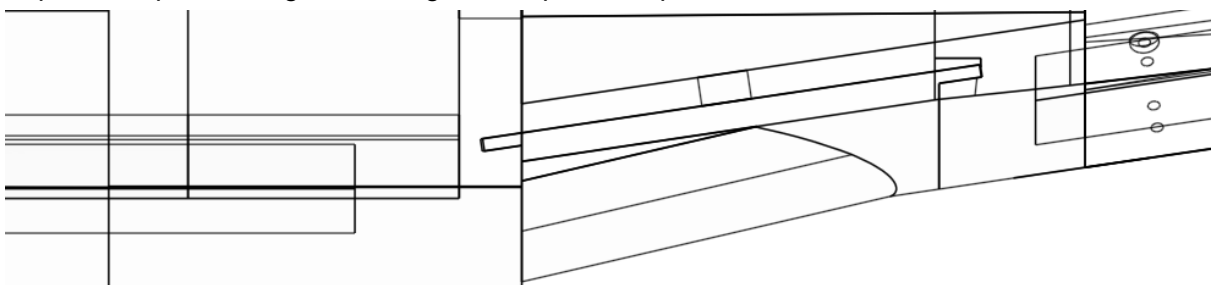
Depth of step 1%, Length of fairing 6 x depth of step:



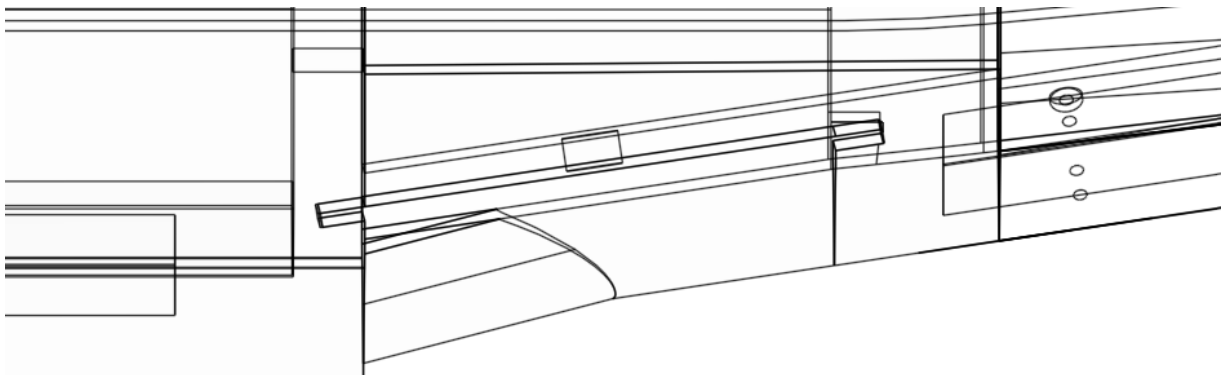
Depth of step 1%, Length of fairing 8 x depth of step:



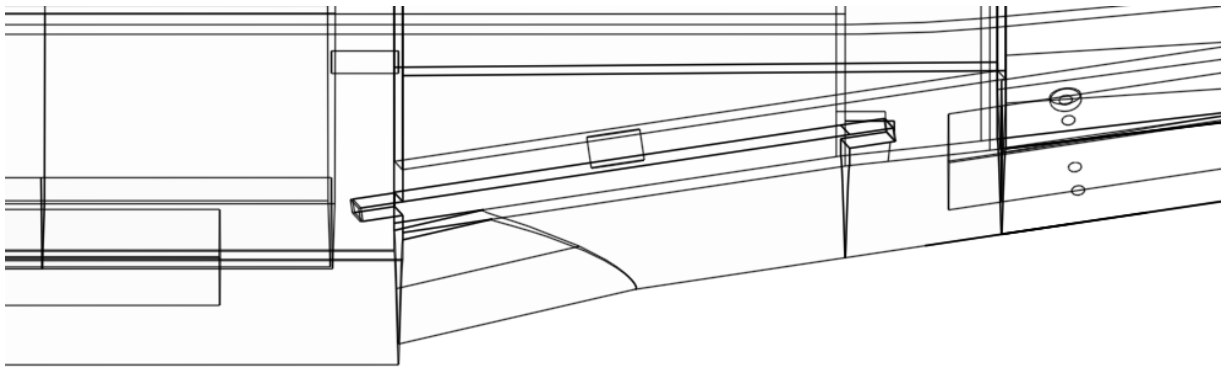
Depth of step 1%, Length of fairing 10 x depth of step:



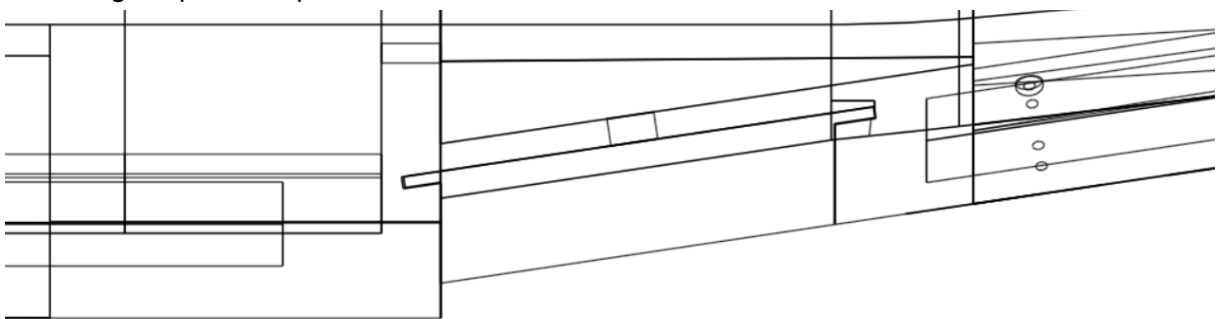
Depth of step 2%, Length of fairing 6 x depth of step:



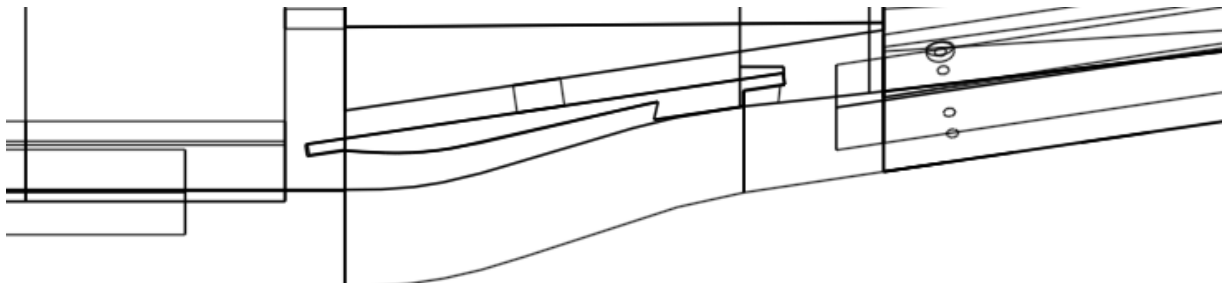
Depth of step 3%, Length of fairing 6 x depth of step:



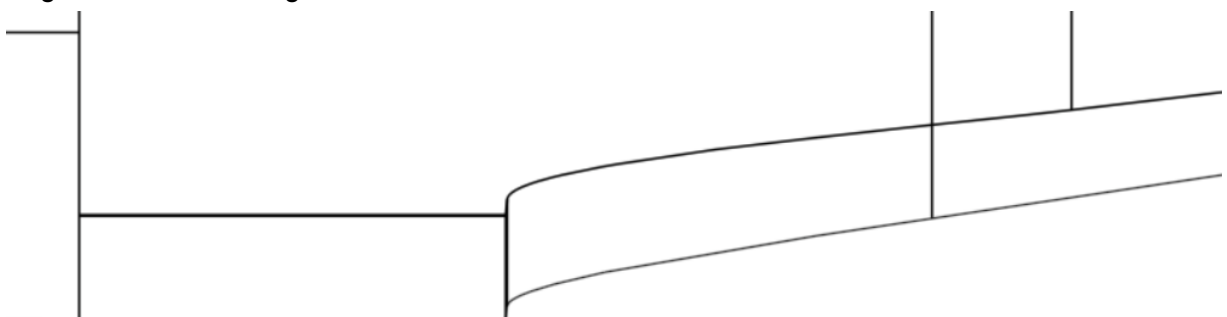
No Faring, Depth of step 5.8%



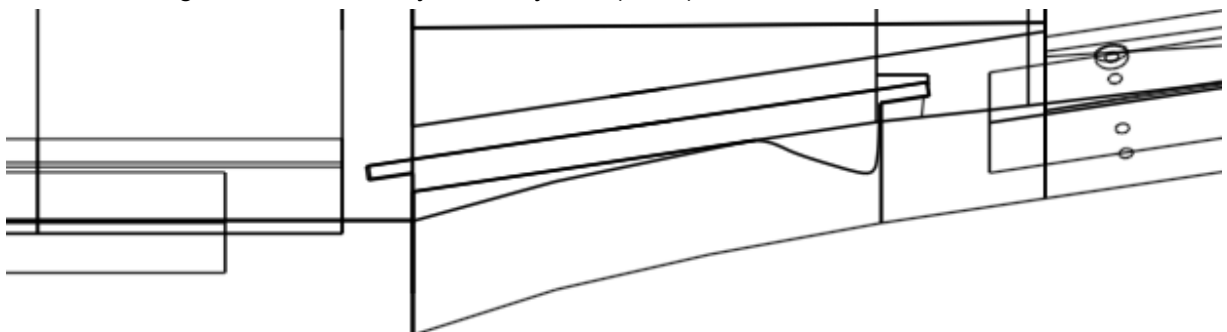
Fully faired:



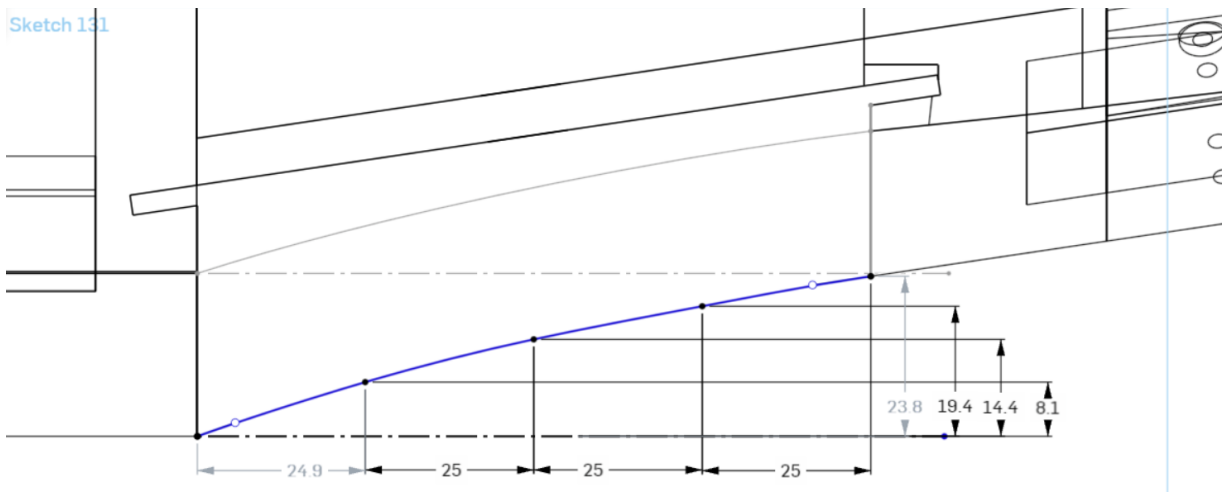
Original concave fairing as baseline:



Concave fairing based on Conway and Maynard (1943)



Measurements [mm] used to define the concave fairing based on Conway and Maynard (1943)



B Deceleration of AI aids and tools

Have any AI-based aids or tools been used in the creation of this report?

No

Yes

If yes: please specify the aid/tool and area of use below.

Listed below in respective sections

Text

Spell checking. Are parts of the text checked by:

Grammarly, Ginger, Grammarbot, LanguageTool, ProWritingAid, Sapling, Trinka.ai, or similar tools?

Text generation. Are parts of the text generated by:

ChatGPT, GrammarlyGO, CopyAI, WordAi, WriteSonic, Jasper, Simplified, Rytr, or similar tools?

Writing assistance. Are one or more of the report ideas or approaches suggested by:

ChatGPT, Google Bard, Bing chat, YouChat, or similar tools?

If yes, use of text aids/tools apply to this report - please specify usage here:

Grammarly was used for spell checking.

Codes and algorithms

Programming assistance. Are parts of the codes/algorithms that i) appear directly in the report or ii) have been used to produce results such as figures, tables, or numerical values generated by: *Github, Copilot, CodeGPT, Google Codey/Studio Bot, Replit Ghostwriter, Amazon CodeWhisperer, GPT Engineer, ChatGPT, Google Bard* or similar tools?

If yes, use of programming assistance aid/tools apply to this report - please specify usage here:

GPT 4o was used for assisting in writing certain parts of the Matlab Scripts used for the procecing and plotting of wind tunnel data, as well as with certain code for latex formating.

Images and figures

N

Image generation. Are one or more of the reports images/figures generated by:
Midjourney, Jasper, WriteSonic, Stability AI, Dall-E, or similar tools?

If yes, use of image generator aids/tools apply to this report – please specify usage here:

Y

Other AI aids or tools. Have you used other types of AI aids or -tools in the creation of this report?
If yes, please specify usage here:

Notebooklm from google was used in the research phase as an advanced Ctrl + F search function to search for information in PDF's. The generative text function was not used.

Y

I am familiar with NTNU's regulations: *Submitting a report generated with the assistance of AI tools and claiming the work to be partially or fully my own, is not permitted. I therefore declare that any use of AI aids or tools is explicitly stated i) directly in the report or ii) in this declaration form.*

Joakim Sægen / 16.12.24 / Torp
Signature / Date / Place

C CFD Appendix

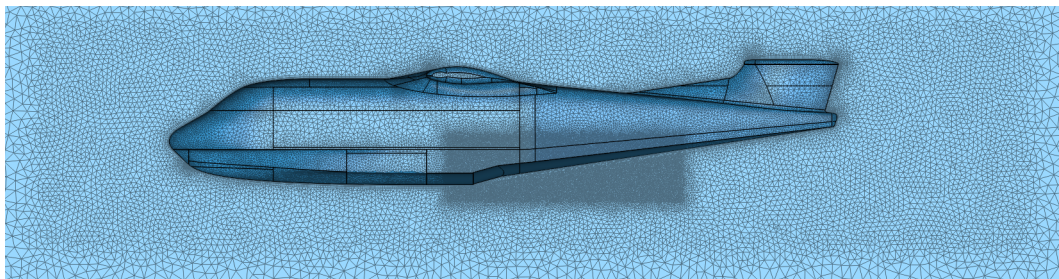


Figure C.1: Zoomed in of mesh used in the CFD study comparing steps

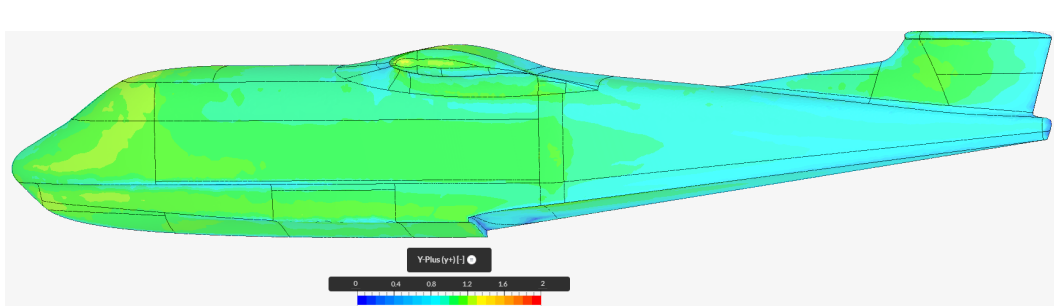
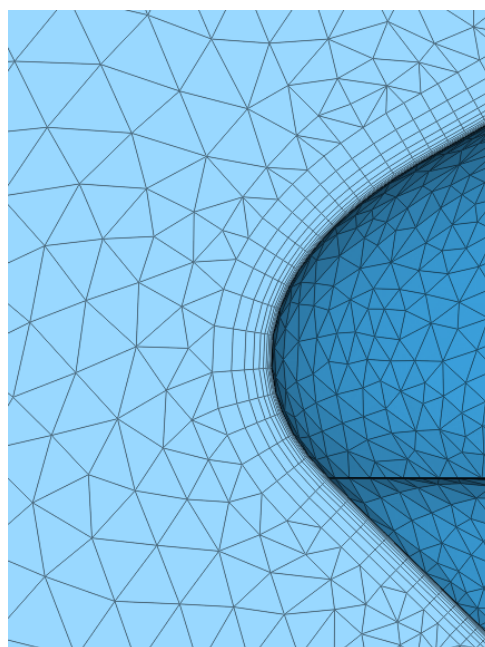
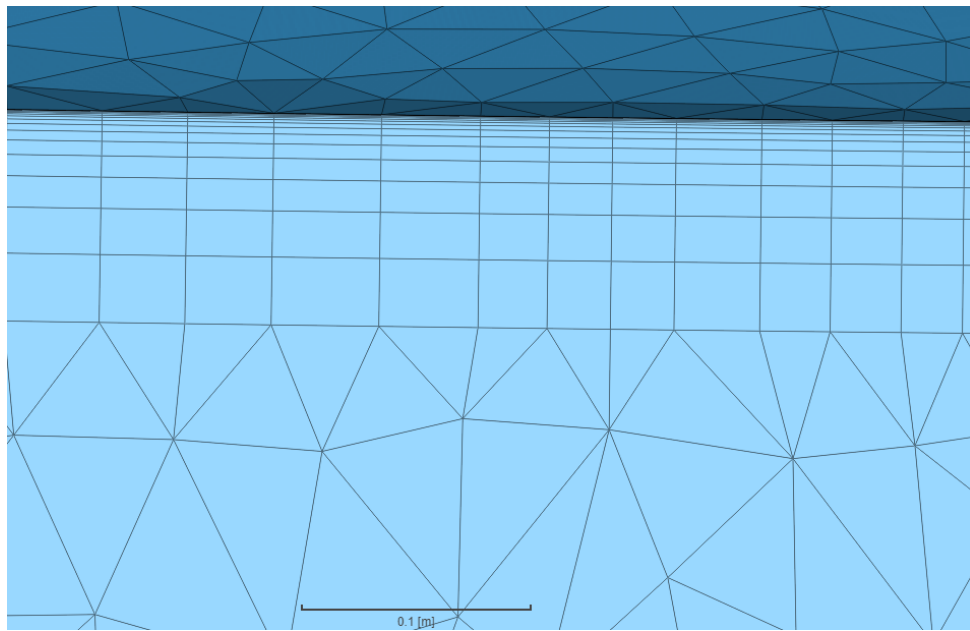
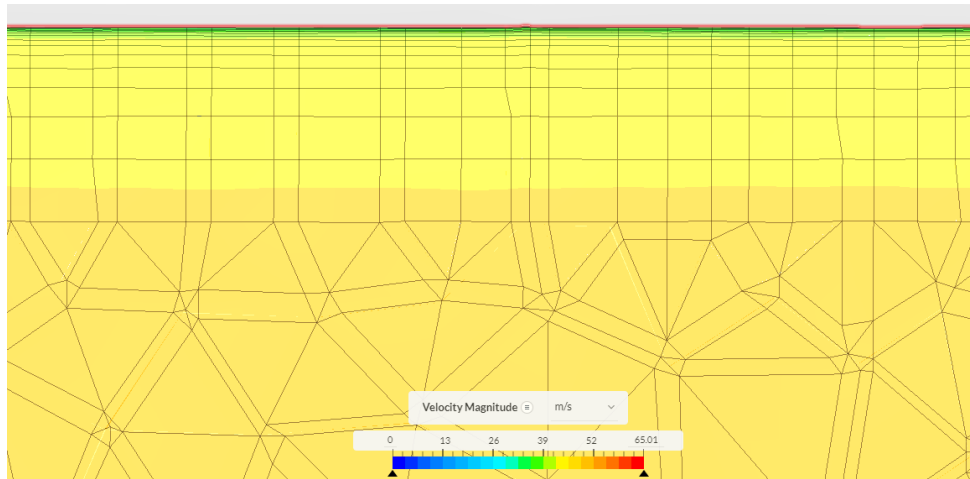


Figure C.3: Y^+ plotted on the surface of the model, in the range of 0 to 2



(a) Close up view of inflation layer mesh, on the keel, right before the step



(b) Same section as Figure C.4a, showing the flow field. The Boundary layer can see to be contained in the inflation layers

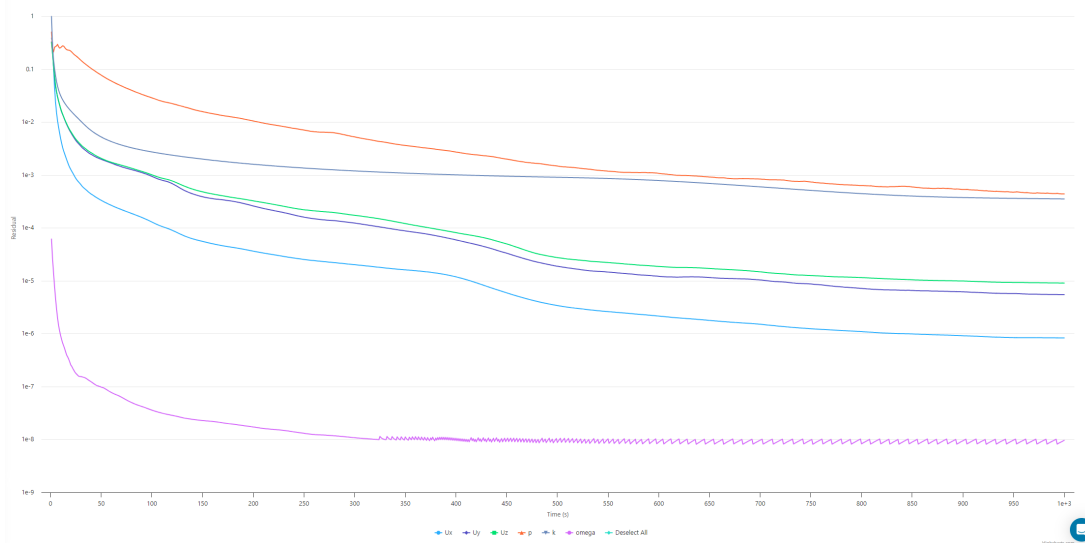
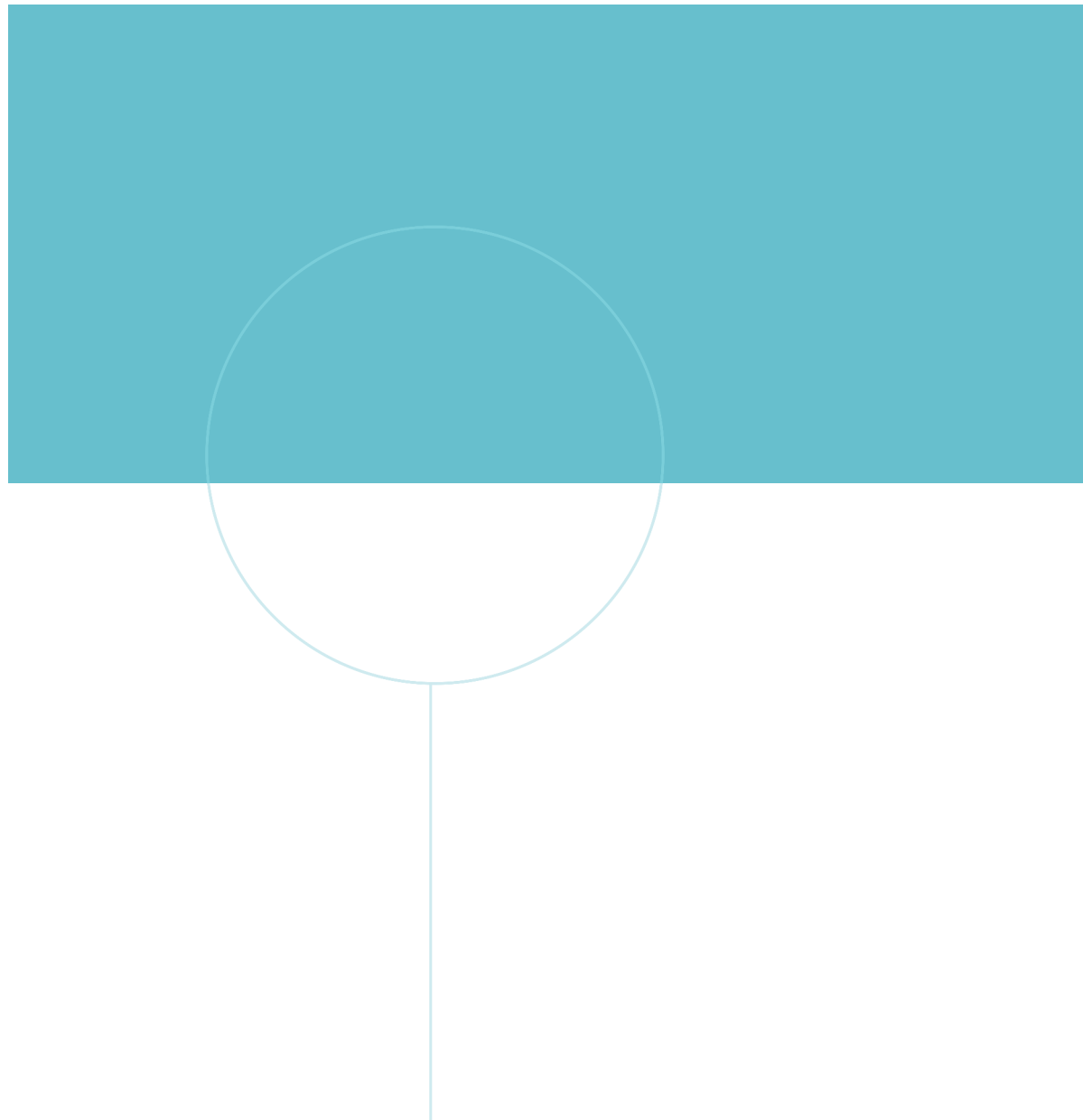


Figure C.5: Residuals plotted for the run with no fairings



NTNU

Norwegian University of
Science and Technology